JOURNAL OF MATERIALS SCIENCE **29** (1994) 3857–3896

Review

The physics and mechanics of fibre-reinforced brittle matrix composites

A. G. EVANS, F. W. ZOK
Materials Department, College of Engineering, University of California, Santa Barbara, CA 9310-5050, USA

This review compiles knowledge about the mechanical and structural performance of brittle matrix composites. The overall philosophy recognizes the need for models that allow efficient interpolation between experimental results, as the constituents and the fibre architecture are varied. This approach is necessary because empirical methods are prohibitively expensive. Moreover, the field is not yet mature, though evolving rapidly. Consequently, an attempt is made to provide a framework into which models could be inserted, and then validated by means of an efficient experimental matrix. The most comprehensive available models and the status of experimental assessments are reviewed. The phenomena given emphasis include: the stress/strain behaviour in tension and shear, the ultimate tensile strength and notch sensitivity, fatigue, stress corrosion and creep.

Nomenclature

a_i	Parameters found in the paper by Hutchinson and Jensen [33], Table IV
a_0	Length of unbridged matrix crack
a_m	Fracture mirror radius
a_N	Notch size
a_t	Transition flaw size
b	Plate dimension
b_i	Parameters found in the paper by Hutchinson and Jensen [33], Table IV
c_i	Parameters found in the paper by Hutchinson and Jensen [33], Table IV
d	Matrix crack spacing
d_s	Saturation crack spacing
f	Fibre volume fraction
f_ℓ	Fibre volume fraction in the loading direction
g	Function related to cracking of 90° plies
h	Fibre pull-out length
ℓ	Sliding length
ℓ_i	Debond length
ℓ_s	Shear band length
m	Shape parameter for fibre strength distribution
m_m	Shape parameter for matrix flaw-size distribution
n	Creep exponent
n_m	Creep exponent for matrix
n_f	Creep exponent for fibre
q	Residual stress in matrix in axial orientation
s_{ij}	Deviatoric stress
t	Time
t_p	Ply thickness
t_b	Beam thickness
u	Crack opening displacement (COD)
u_a	COD due to applied stress
u_b	COD due to bridging
v	Sliding displacement
w	Beam width
B	Creep rheology parameter $\dot{\varepsilon}_0/\sigma_0^n$
C_V	Specific heat at constant strain
E	Young's modulus for composite
E_0	Plane strain Young's modulus for composites
$\bar{E}$	Unloading modulus
E_*	Young's modulus of material with matrix cracks
E_f	Young's modulus of fibre
E_m	Young's modulus of matrix
E_L	Ply modulus in longitudinal orientation
E_T	Ply modulus in transverse orientation
E_t	Tangent modulus
E_s	Secant modulus
G	Shear modulus
$\mathcal{G}$	Energy release rate (ERR)
$\mathcal{G}_\mathrm{tip}$	Tip ERR
$\mathcal{G}^0_\mathrm{tip}$	Tip ERR at lower bound
K	Stress intensity factor (SIF)
K_b	SIF caused by bridging
K_m	Critical SIF for matrix
K_R	Crack growth resistance
K_tip	SIF at crack tip
I_0	Moment of inertia
L	Crack spacing in 90° plies
L_f	Fragment length
L_g	Gauge length
L_0	Reference length for fibres
N	Number of fatigue cycles
N_s	Number of cycles at which sliding stress reaches steady-state

R	Fibre radius
$\mathcal{R}$	R-ratio for fatigue ($\sigma_{max}/\sigma_{min}$)
$\mathcal{R}_c$	Radius of curvature
S	Tensile strength of fibre
S_b	Dry bundle strength of fibres
S_c	Characteristic fibre strength
S_g	UTS subject to global load sharing
S_0	Scale factor for fibre strength
S_p	Pull-out strength
S_{th}	Threshold stress for fatigue
S_u	Ultimate tensile strength (UTS)
S_*	UTS in the presence of a flaw
T	Temperature
ΔT	Change in temperature
Δt	Traction function for thermomechanical fatigue (TMF)
Δt_b	Bridging function for TMF
α	Linear thermal coefficient of expansion (TCE)
α_f	TCE of fibre
α_m	TCE of matrix
γ	Shear strain
γ_c	Shear ductility
δ_c	Characteristic length
$\delta\varepsilon$	Hysteresis loop width
ε	Strain
ε_*	Strain caused by relief of residual stress upon matrix cracking
ε_e	Elastic strain
ε_0	Permanent strain
$\dot{\varepsilon}_0$	Reference strain rate for creep
ε_τ	Transient creep strain
ε_s	Sliding strain
λ	Pull-out parameter
μ	Friction coefficient
ξ	Fatigue exponent (of order 0.1)
κ	Beam curvature
ν	Poisson's ratio
ϕ	Orientation of interlaminar cracks
ϱ	Density
σ	Stress
σ_b	Bridging stress
$\bar{\sigma}_b$	Peak, reference stress
σ_e	Effective stress = $[(3/2)s_{ij}s_{ij}]^{1/2}$
σ_f	Stress in fibre
σ_i	Debond stress
σ_m	Stress in matrix
σ_{mc}	Matrix cracking stress
σ^0	Stress on 0° plies
σ_0	Creep reference stress
σ_{rr}	Radial stress
σ^R	Residual stress
σ_s	Saturation stress
σ_s^*	Peak stress for traction law
σ_τ	Lower bound stress for tunnel cracking
σ^T	Misfit stress
τ	Interface sliding stress
τ_f	Value of sliding stress after fatigue
τ_0	Constant component of interface sliding stress
τ_s	In-plane shear strength
$\bar{\tau}_c$	Critical stress for interlaminar crack growth
τ_{ss}	Steady-state value of τ after fatigue
Δ^R	Displacement caused by matrix removal
$\Delta\varepsilon_p$	Unloading strain differential
$\Delta\varepsilon_0$	Reloading strain differential
Γ	Fracture energy
Γ_i	Interface debond energy
Γ_f	Fibre fracture energy
Γ_m	Matrix fracture energy
Γ_R	Fracture resistance
Γ_S	Steady-state fracture resistance
Γ_T	Transverse fracture energy
Ω	Misfit strain
Ω_0	Misfit strain at ambient temperature

1. Introduction

1.1. Rationale

Various types of brittle matrix composite exist, based on ceramics, glasses, polymers and intermetallics. The respective designations are CMCs, GMCs, PMCs and IMCs. The fibres are used to impart sound structural characteristics, particularly to resist the propagation of cracks when either steady or cyclic loads are imposed. However, all of the thermomechanical properties are affected by the fibres, sometimes profoundly. As a result, the approaches needed for design and assuring reliability are completely different from those used for monolithic metals, ceramics and polymers. The underlying principles are explored in this review. Many of the basic ideas originated with the development of PMCs. In these materials, the matrix has relatively low modulus and strength, but moderate ductility. The fibres enhance the modulus and strength but reduce the ductility. The mechanisms that dictate the structural performance of PMCs reflect these factors. In CMCs and GMCs, as well as many IMCs, the elastic properties of the fibres and matrix are similar and the matrix has low ductility. Consequently, the mechanisms that operate in response to thermomechanical loads are often quite different from those found in PMCs. The emphasis of this article is on composites exemplified by CMCs, GMCs and IMCs. The materials referenced in the following text are specified in Table I.

Continuous fibre-reinforced brittle-matrix composites have a major advantage compared with the monolithic matrix. They exhibit an ability to retain good tensile strength in the presence of holes and notches [1–3]. This characteristic is important because composite components generally need to be attached to other components, usually metals. At

TABLE I CMC material systems

SiC/CAS	Calcium alumino silicate glass ceramic with Nicalon fibres
SiC/SiC$_{CVI}$	Silicon carbide produced by chemical vapor infiltration (CVI) with Nicalon fibres
SiC/SiC$_{PP}$	Silicon carbide matrix produced by a polymer precursor method with Nicalon fibres
SiC/C	Carbon matrix produced by a combination of pyrolysis and CVI with Nicalon fibres The subscripts B and C refer to two different particulate phases in the matrix
C/C	Carbon fibre reinforced carbon matrices

these attachments (whether mechanical or bonded), stress concentrations arise, which dominate the design and reliability. Inelastic deformation at these sites is crucial. It alleviates the elastic stress concentration by locally redistributing stress [4]. Such inelasticity is present in brittle matrix composites [5–8]. In association with the inelastic deformation, various degradation processes occur which affect the useful life of the material. Several fatigue effects are involved [9, 10], cyclic, static and thermal. The most severe degradation appears to occur subject to out-of-phase thermomechanical fatigue (TMF). In addition, creep and creep rupture occur at high temperatures [11].

All of the mechanical characteristics that govern structural utility and life depend upon the constituent properties (fibres, matrix, interfaces), as well as the fibre architecture. Because the constituents are variables, optimization of the property profiles needed for design and lifing become prohibitively expensive if traditional empirical procedures are used. The philosophy of this article is based on the recognition that mechanism-based models are needed, which allow efficient interpolation between a well-conceived experimental matrix. The emphasis is on the creation of a framework which allows models to be inserted, as they are developed, which can also be validated by carefully chosen experiments.

1.2. Objectives

The initial intent of this review is to address the mechanisms of stress redistribution upon monotonic and cyclic loading, as well as the mechanics needed to characterize the notch sensitivity [4, 12]. This assessment is conducted primarily for composites with two-dimensional reinforcements. The basic phenomena that give rise to inelastic strains are matrix cracks and fibre failures subject to interfaces that debond and slide (Fig. 1) [13–15]. These phenomena identify the essential constituent properties, which have the typical values indicated on Table II.

Three underlying mechanisms are responsible for the non-linearity [16, 17]: (i) Frictional dissipation occurs at the fibre/matrix interfaces, whereupon the sliding resistance of debonded interfaces, τ, becomes a key parameter. Control of τ is critical. This behaviour is dominated by the fibre coating, as well as the fibre morphology [18, 19]. By varying τ, the prevalent damage mechanism and the resultant non-linearity can be dramatically modified; (ii) the matrix cracks increase the elastic compliance [20]; (iii) the matrix cracks also cause changes in the residual stress distribution, resulting in a permanent strain [20].

The relative ability of these mechanisms to operate depends on the loading, as well as the fibre orientation. It is necessary to address and understand the mechanisms that operate for loadings which vary from tension along one fibre direction to shear at various orientations. For tensile loading, several damage mechanisms have been found, involving matrix cracks combined with sliding interfaces (Fig. 2). These can be visualized by mechanism maps [21], which then become an integral part of the testing and design activity. One damage mechanism involves mode I cracks with simultaneous fibre failure, referred to as class I behaviour (Fig. 2). Stress redistribution is provided by the tractions exerted on the crack by the failed fibres, as they pull out [12, 22–24]. A second damage mechanism involves multiple matrix cracks, with minimal fibre failure referred to as class II behaviour (Fig. 2). In this case, the plastic deformation caused by matrix cracks allows stress redistribution [3, 4]. A schematic drawing of a mechanism map based on these two damage mechanisms (Fig. 3) illustrates another important issue: the use of non-dimensional parameters to interpolate over a range of constituent

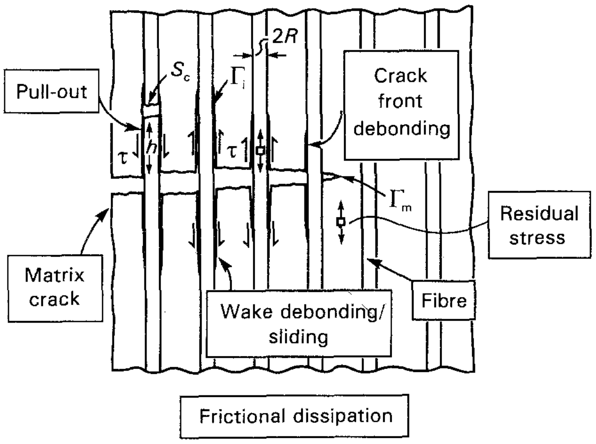

Figure 1 The fundamental mechanisms that operate in CMCs as a crack extends through the matrix.

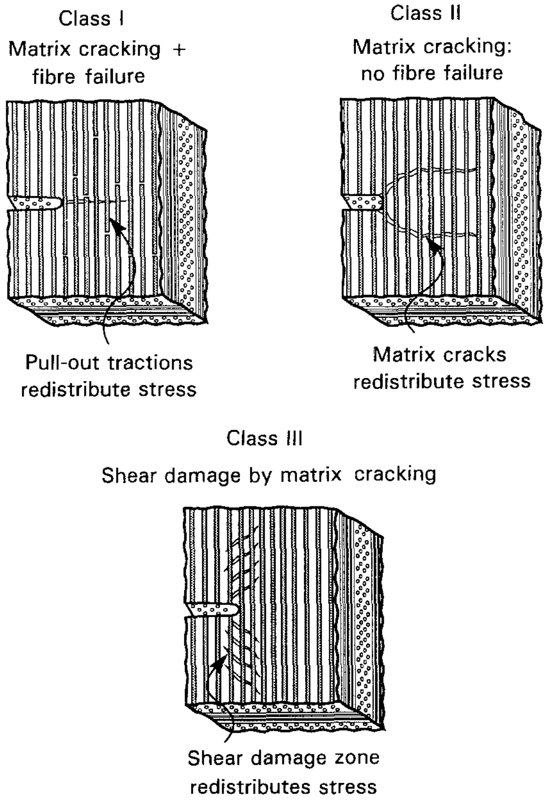

Figure 2 Three prevalent damage mechanisms occurring around notches in CMCs. Each mechanism allows stress redistribution by a combination of matrix cracking and fibre pull-out.

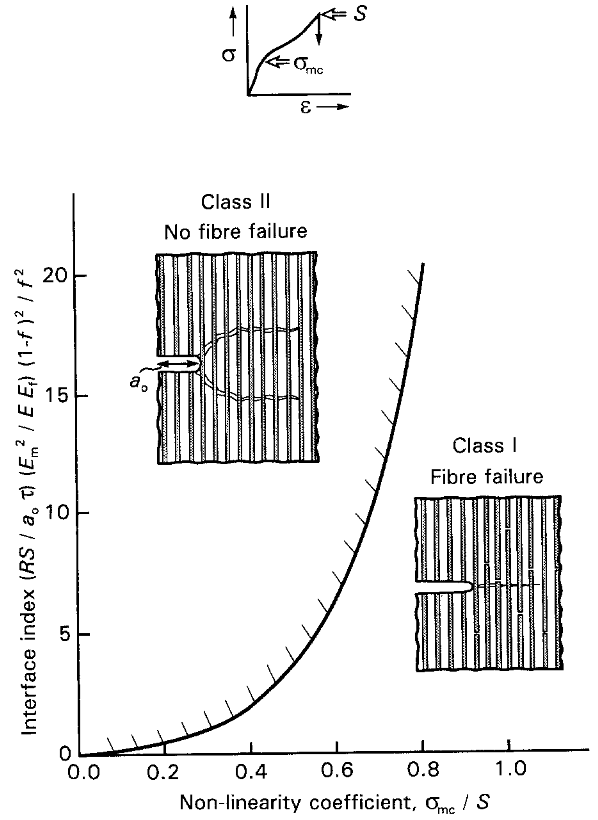

Figure 3 A proposed mechanism map that distinguishes class I and class II tensile behaviour.

TABLE II Constituent properties of CMCs and methods of measurement

Constituent property	Measurement methods	Typical range
Sliding stress, τ (MPa)	Push-out force Pull-out length, $\bar{h}$ Saturation crack spacing, $\bar{l}_s$ Hysteresis loop, $\delta\varepsilon$ Unloading modulus, $\bar{E}_L$	1–200
Characteristic strength, S_c (GPa)	Fracture mirrors Pull-out length, $\bar{h}$	1.2–3.0
Misfit strain, Ω	Bilayer distortion Permanent strain, ε_0 Residual crack opening	$0\text{–}2 \times 10^{-3}$
Matrix fracture energy, Γ_m (J m^{-2})	Monolithic material Saturation crack spacing, $\bar{l}_s$ Matrix cracking stress, $\bar{\sigma}_{mc}$	5–50
Debond energy, Γ_i (J m^{-2})	Permanent strain, ε_0 Residual crack opening, u_p	0–5

properties. (For ease of reference, all of the most important non-dimensional parameters are listed in Table III). On the mechanism map, the ordinate is a non-dimensional measure of sliding stress and the abscissa is a non-dimensional *in situ* fibre strength. A third damage mechanism also exists (Fig. 2), referred to as class III. It involves matrix shear damage prior to composite failure as a means for redistributing stress. A proposed mechanism map is presented in Fig. 4 [25].

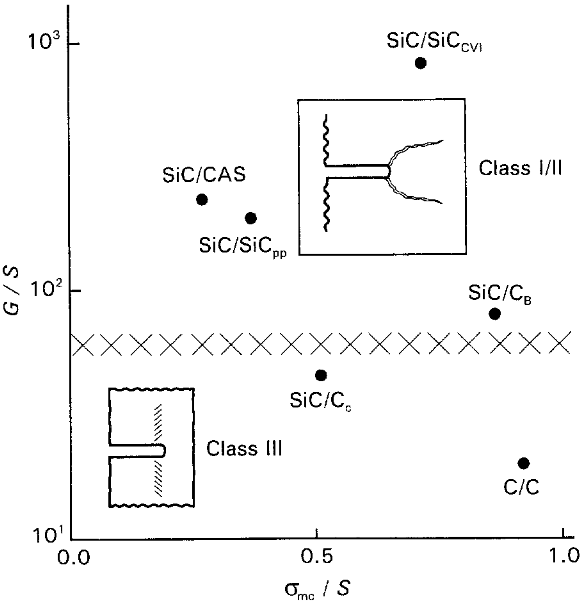

Figure 4 A proposed mechanism map that distinguishes class III behaviour. The CMCs used for this figure are summarized in Table I.

A summary of tensile stress–strain curves obtained for a variety of two-dimensional composites (Fig. 5) highlights the most fundamental characteristic relevant to the application of CMCs. Among these four materials (Table I), the SiC/CAS system is found to be notch insensitive in tension [3], even for quite large notches (~ 5 mm long). The other three materials exhibit varying degrees of notch sensitivity [26, 27]. Moreover, the notch insensitivity in SiC/CAS arises despite relatively small plastic strains. These results delineate two issues that need resolution. (i) How much plastic strain is needed to impart notch insensitivity? (ii) Is the ratio of the "yield" strength to ultimate tensile strength (UTS) an important factor in notch sensitivity? This review will address both questions.

The shear behaviour also involves matrix cracking and fibre failure [25]. However, the ranking of the shear stress–strain curves between materials (Fig. 6) differs appreciably from that found for tension (Fig. 5). Preliminary efforts at understanding this difference and for providing a methodology to interpolate between shear and tension will be described.

Analyses of damage and failure have established that certain constituent properties are basic to composite performance (Table II). These need to be measured, independently, and then used as characterizing parameters, analogous to the yield strength and fracture toughness in monolithic materials. The six major independent parameters are the interfacial sliding stress, τ, and debond energy, Γ_i, the *in situ* fibre properties, S_c and m, the fibre/matrix misfit strain, Ω, and the matrix fracture energy Γ_m, as well as the elastic properties, E, ν [4]. Dependent parameters that can often be used to infer the constituent properties include: the fibre pull-out length [7, 14, 28], the fracture mirror radius of the fibres [29] and the saturation crack spacing in the matrix [30]. Approaches for measuring the constituent properties in a consistent,

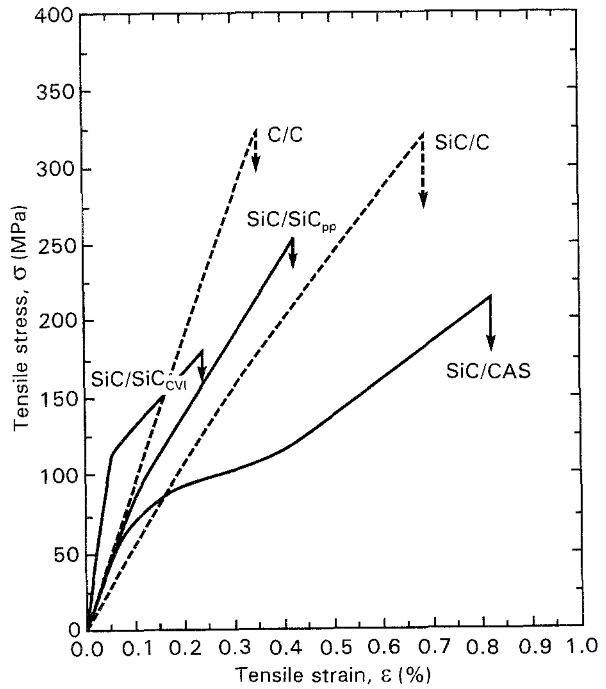

Figure 5 Tensile stress–strain curves measured for a variety of two-dimensional CMCs.

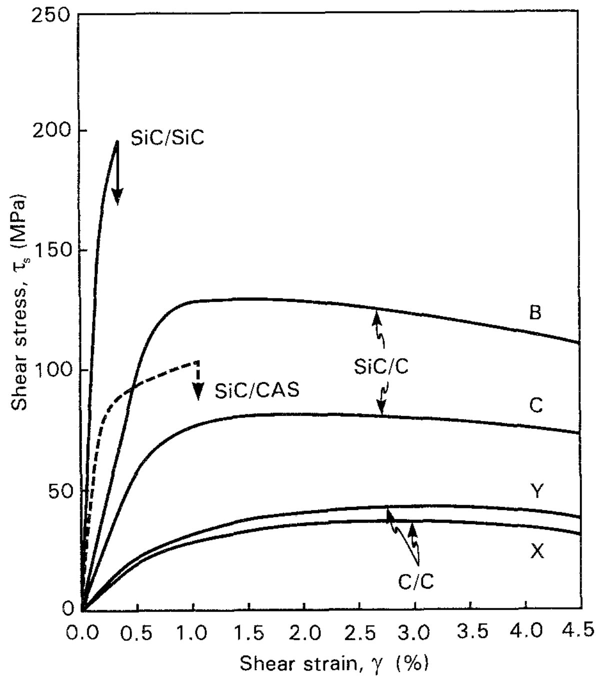

Figure 6 Shear stress–strain curves measured for two-dimensional CMCs.

straightforward manner will be emphasized and their relevance to composite behaviour explored through models of damage and failure. Moreover, the expressions that relate composite behaviour to constituent properties are often unwieldy, because a large number of parameters are involved. Consequently, throughout this article, the formulae used to represent CMC behaviour are the simplest capable of describing the major phenomena. (The behaviour represented by these formulae is often applicable only to composites: the equivalent phenomenon being absent in monolithic ceramics. Consequently, the expressions should be restricted to composites with fibre volume fractions in the range of practical interest (f between 0.3 and 0.5). Extrapolation to small f would lead to erroneous interpretations, because mechanism changes usually occur.)

In most composites with desirable tensile properties, linear elastic fracture mechanics (LEFM) criteria are violated [31, 32]. Instead, various large-scale non-linearities arise, associated with matrix damage and fibre pull-out. In consequence, an alternative mechanics is needed to specify the relevant material and loading parameters and to establish design rules. Some progress toward this objective will be described and related to test data. This has been achieved using large-scale bridging mechanics (LSBM), combined with continuum damage mechanics (CDM) [12, 22–24].

The preceding considerations dictate the ability of the material to survive thermal and mechanical loads imposed for short durations. In many cases, long-term survivability at elevated temperatures dictates the applicability of the material. Life models based on degradation mechanisms are needed to address this issue. For this purpose, generalized fatigue and creep models are required, especially in regions that contain matrix cracks. It is inevitable that such cracks exist in regions subject to strain concentrations and, indeed, are required to redistribute stress. In this situation, degradation of the interface and the fibres may occur as the matrix cracks open and close upon thermomechanical cycling, with access of the atmosphere being possible, through the matrix cracks. The rate of such degradation dictates the useful life.

1.3. Approach

To address the preceding issues, this article is organized in the following manner. Some of the basic thermomechanical characteristics of composites are first established, with emphasis on interfaces and interface properties, as well as residual stresses. Then, the fundamental response of unidirectional (one-dimensional) materials, subject to tensile loading, is addressed, in accordance with several sub-topics: (i) mechanisms of non-linear deformation and failure, (ii) constitutive laws that relate macroscopic performance to constituent properties; (iii) the use of stress–strain measurements to determine constituent properties in a consistent, straightforward manner; (iv) the simulation of stress–strain curves. The discussion of one-dimensional materials is followed by the application of the same concepts to two-dimensional materials, subject to combinations of tensile and shear loading. At this stage, it is possible to address the mechanisms of stress redistribution around flaws, holes, attachments and notches. In turn, these mechanisms suggest a mechanics methodology for relating strength to the size and shape of the flaws, attachment loading, etc.

Data regarding the effects of cyclic loading and creep on the life of brittle matrix composites are limited. The concepts to be developed thus draw upon knowledge and experience gained with other composite systems,

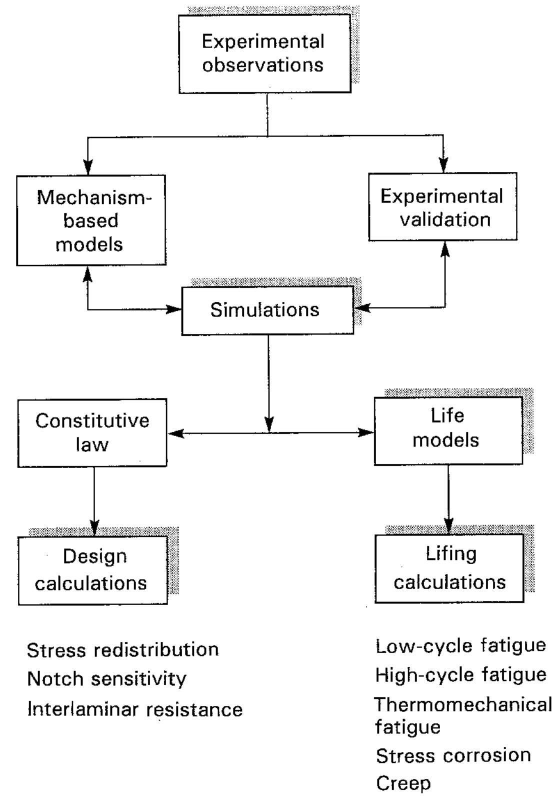

Figure 7 The philosophy adopted for using models in the design and application of CMCs.

such as metal matrix (MMCs) and polymer matrix (PMCs) materials. The overall philosophy is depicted in Fig. 7.

2. Interfaces

2.1. Thermomechanical representation

The thermomechanical properties of coatings at fibre/matrix interfaces are critically important. A consistent characterization approach is necessary. The most commonly adopted hypothesis is that there are two parameters (Fig. 8). One is associated with fracture and the other with slip [33–36]. Fracture, or debonding, is considered to involve a debond energy, Γ_i [21, 37]. Slip is expected to occur with a shear resistance, τ. A schematic representation (Fig. 9) illustrates the issues. Debonding must be a mode II (shear) fracture phenomenon. In brittle systems, mode II fracture typically occurs by the coalescence of microcracks within a material layer [38, 39]. In some cases, this layer coincides with the coating itself, such that debonding involves a diffuse zone of microcrack damage (Fig. 9). In other cases, the layer is very thin and the debond has the appearance of a single crack. For both situations, it is believed that debond propagation can be represented by a debond energy, Γ_i, with an associated stress jump above and below the debond front [33]. Albeit that, in several instances, Γ_i is essentially zero [40]. When a discrete debond crack exists, frictional sliding of the crack faces provides the shear resistance. Such sliding occurs in accordance with a friction law [33–36, 40]

$$\tau = \tau_0 - \mu\sigma_{rr} \qquad (1)$$

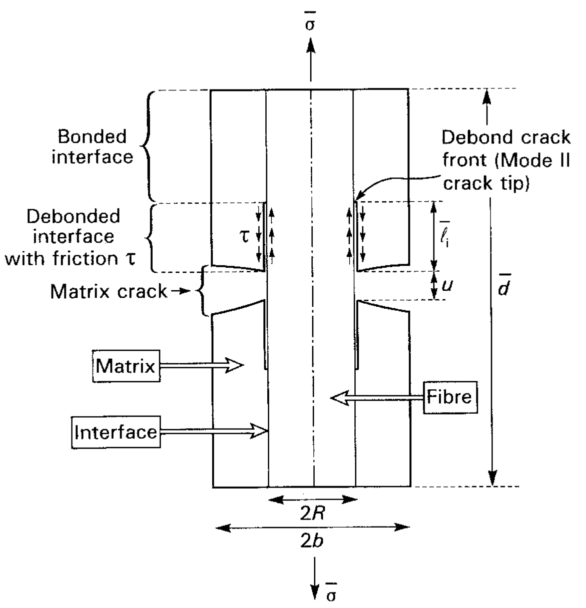

Figure 8 A basic cell model used for CMCs indicating the sliding and debonding behaviour.

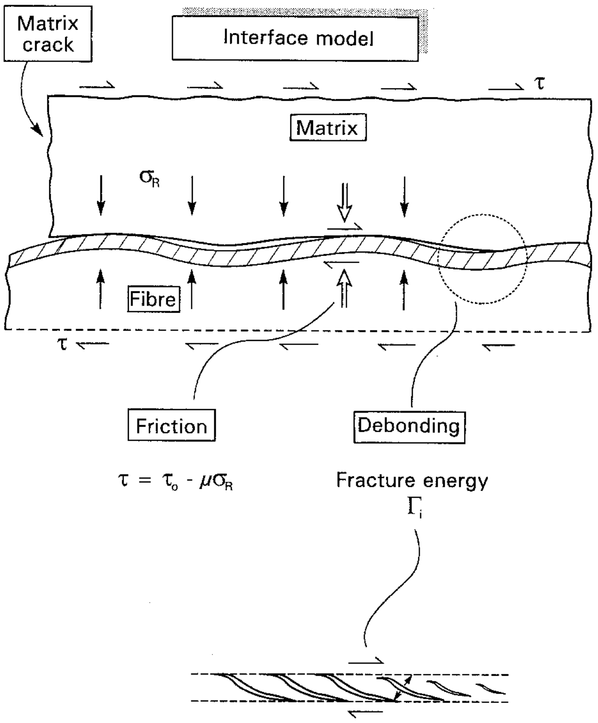

Figure 9 The fibre sliding model indicating the location of debonding and frictional sliding. The cross-hatched region is a thin fibre coating.

where μ is the Coulomb friction coefficient, σ_{rr} is the compression normal to the interface and τ_0 is a term associated with fibre roughness. When the debond process occurs by diffuse microcracking in the coating, it is again assumed (without justification) that the interface has a constant shear resistance, τ_0.

For debonding and sliding to occur, rather than brittle cracking through the fibre, the debond energy, Γ_i, must not exceed an upper bound, relative to the fibre fracture energy, Γ_f [37]. Calculations have suggested that the following inequality must be satisfied

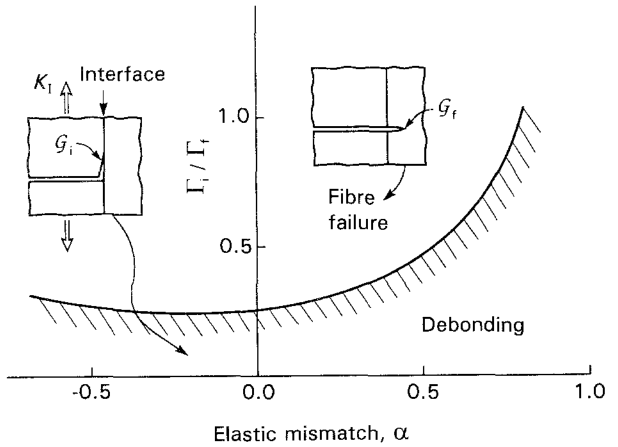

Figure 10 A debond diagram for CMCs. The debond region is below the cross-hatched curve.

(Fig. 10)

$$\Gamma_i \lesssim (\tfrac{1}{4})\Gamma_f \quad (2)$$

Noting that most ceramic fibres have a fracture energy, $\Gamma_f \approx 20\ \mathrm{J\,m^{-2}}$, Equation 2 indicates that the upper bound on the debond energy, $\Gamma_i \approx 5\ \mathrm{J\,m^{-2}}$. This magnitude is broadly consistent with experience obtained on fibre coatings that impart requisite properties [18, 41–44].

2.2. Measurement methods

Measurements of the sliding stress, τ, and the debond energy, Γ_i, have been obtained by a variety of approaches (Table II). The most direct involve displacement measurements. These are conducted in two ways: (i) fibre push-through/push-in, by using a small-diameter indentor [40]; (ii) tensile loading in the presence of matrix cracks [4, 45]. Indirect methods for obtaining τ also exist. These include measurement of the saturation matrix crack spacing [30] and the fibre pull-out length [14]. The direct measurement methods require accurate determination of displacements, coupled with an analysis that allows rigorous deconvolution of load–displacement curves. The basic analyses used for this purpose are contained in papers by Hutchinson and Jensen [33], Liang and Hutchinson [46], and Jero *et al.* [35]. The fundamental features are illustrated by the behaviour found upon tensile loading, subsequent to matrix cracking (Fig. 11). The hysteresis that occurs during an unload/reload cycle relates to the sliding stress, τ. Accurate values for τ can be obtained from hysteresis measurements [4, 17, 47]. Furthermore, these results are relevant to the small sliding displacements that occur during matrix crack evolution in actual composites. (Information about τ at larger sliding displacements is usually obtained from fibre push-through measurements.) The plastic strains contain combined information about τ, Ω and Γ_i. Consequently, if τ is already known, Γ_i can be evaluated from the plastic strains measured as a function of load, especially if Ω has been obtained from independent determinations [4]. The basic formulae that connect τ, Γ_i and Ω to the stress–strain behaviour are presented in a subsequent section.

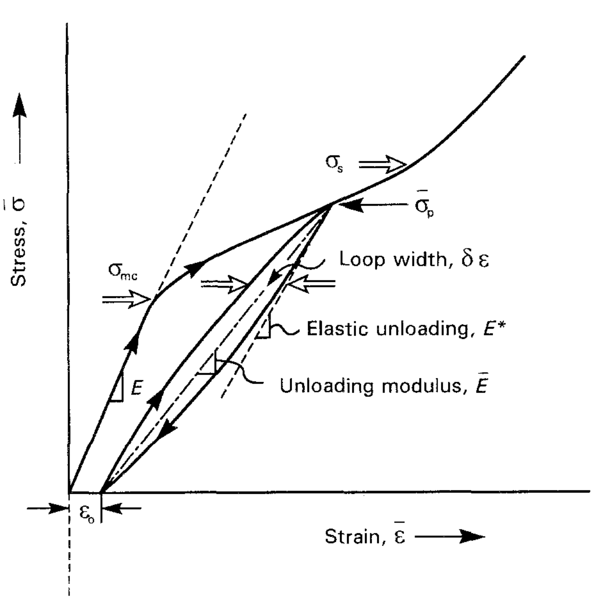

Figure 11 A typical load–unload cycle showing the parameters that can be measured which relate to the interface properties.

2.3. Sliding models

The manipulations of interfaces needed to control τ can be appreciated by using a model to simulate the sliding behaviour. A simplified sliding model has been developed (Fig. 19) which embodies the role of the pressure at contact points, due to the combined effects of a mismatch strain and roughness [35, 36]. Coulomb friction is regarded as the fundamental friction law operating at contacts. Otherwise, the system is considered to be elastic. The variables in the analysis are (i) the amplitude and wavelength of the roughness; (ii) the mismatch strain, Ω; (iii) the Coulomb friction coefficient, μ; and (iv) the elastic properties of the constituents. With these parameters as input, the sliding can be simulated for various loading situations. One set of simulations conducted for comparison with fibre push-out tests (Fig. 12) illustrates the relative importance of each of the variables. For this set, the fibre roughness was characterized using a fractal method. The roughness within the section was selected at random, from the measured amplitude distribution, causing some differences in the push-out spectrum for each simulation. By using this simulation, substantial systematic changes in the sliding resistance have been predicted when the friction coefficient, the mismatch strain and the roughness amplitude are changed. (There are only minor effects of Poisson's ratio). Generally, the mismatch strain and the roughness can be measured independently [36]. Consequently, the comparison between simulation and experiment actually provides an estimate of the friction coefficient, μ. If this is found to be within an acceptable range, the inferred μ is, thereafter, used to predict how τ can be expected to vary as either the misfit or the roughnesses are changed, if μ is fixed. This approach indicates that $\mu \approx 0.1$ for either carbon or BN coatings [48],

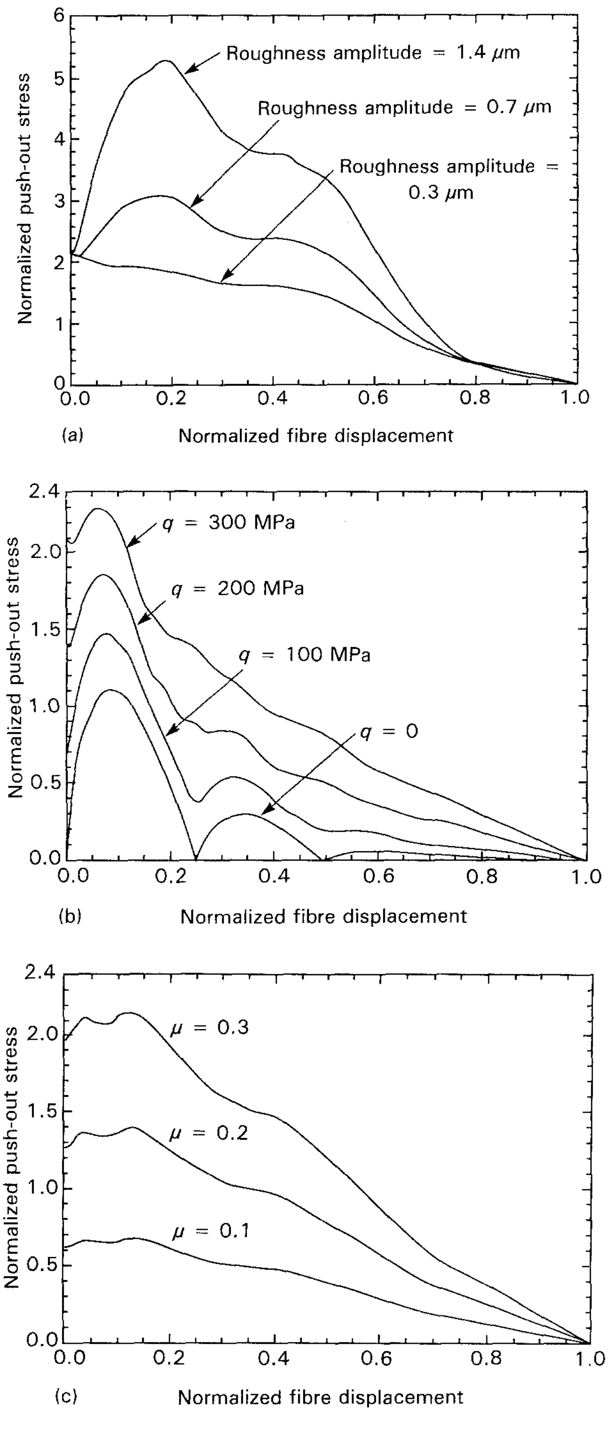

Figure 12 Simulation of the effects of the key variables on the push-out behaviour: (a) roughness, (b) residual stress, (c) friction coefficient.

whereas $\mu \approx 0.5$ for oxide coatings [49]. Such values are compatible with macroscopic friction measurements made on bulk materials and thus appear to be reasonable. However, much additional testing is needed to validate the sliding model.

2.4. Experimental results

Most of the experience with brittle matrix composites is on carbon, BN, or molybdenum fibre coatings [18, 19, 41–44, 50]. Such coatings usually have a relatively low debond energy, Γ_i, and can provide a range of sliding stresses, τ (Table II), as illustrated by comparison of three different carbon coatings on sapphire fibres in TiAl (Fig. 13a). A considerable range in τ has even been achieved with carbon coatings. Values between 2 and 200 MPa have been found. Furthermore, this range obtains even at comparable values of the misfit strain. The different values may relate to fibre roughness. Roughness effects are best illustrated by the sliding behaviour of sapphire fibres in a glass matrix. During fibre manufacture, sinusoidal asperities are grown on to the surface of the sapphire fibres. The sinusoidal fibre surface roughness is manifest as a wavelength modulation in the sliding stress during push-out (Fig. 13b) [36]. However, there must also be influences of the coating thickness and microstructure. A model that includes an explicit influence of the coating has yet to be developed.

In many brittle matrix composites, the debond energy, Γ_i, has been found to be negligibly small ($\Gamma_i < 0.1$ J m^{-2}). Such systems include all of the glass ceramic matrix systems reinforced with Nicalon fibres, which have a carbon interphase formed by reaction during composite processing. Low values also seem to obtain for SiC matrix composites with BN fibre coatings. The clear exception is SiC/SiC composites made by chemical vapour infiltration (CVI), which use a carbon interphase, introduced by chemical vapour deposition [51]. For such composites, the non-linear behaviour indicates a debond energy, $\Gamma_i \approx 1$–5 J m^{-2} (Table II). The interphase in this case debonds by a diffuse damage mechanism [52]. Moreover, it has been found that the coating behaviour can be changed into one with $\Gamma_i \approx 0$, either by heat treatment of the composite (after CVI) or by chemical treatment of the fibre [51]. A basic understanding of these changes in Γ_i does not exist.

2.5. Environmental influences

There are temperature and environmental effects on τ and Γ_i. There are also effects on τ of fibre displacement and cyclic sliding (Fig. 13c). These effects can critically influence composite performance. The basic effect of temperature on τ [53] concerns changes in the misfit strain and friction coefficient, evident from the simulations shown in Fig. 12. Environmental influences can be pronounced, especially in oxidizing atmospheres. The major effects arise either at high temperatures, or during fatigue (a consequence of internal heating associated with cyclic frictional sliding at the interfaces). When either carbon or molybdenum coatings are used, τ initially decreases upon either exposure or fatigue (Fig. 13d), because a gap is created between the fibre and matrix, caused by elimination of the coating, through volatile oxide formation [7, 18, 53–55]. This process occurs when the local temperature reaches ~ 800 °C. The subsequent behaviour depends on the fibres. When SiC fibres are used, further exposure causes SiO_2 formation [56]. This layer gradually fills the gap, leading to large values of τ. Eventually, a "strong" interface bond forms (with large Γ_i) that produces brittle behaviour, without fibre pull-out. Conversely, oxide fibres in oxide matrices are inherently resistant to this embrittlement

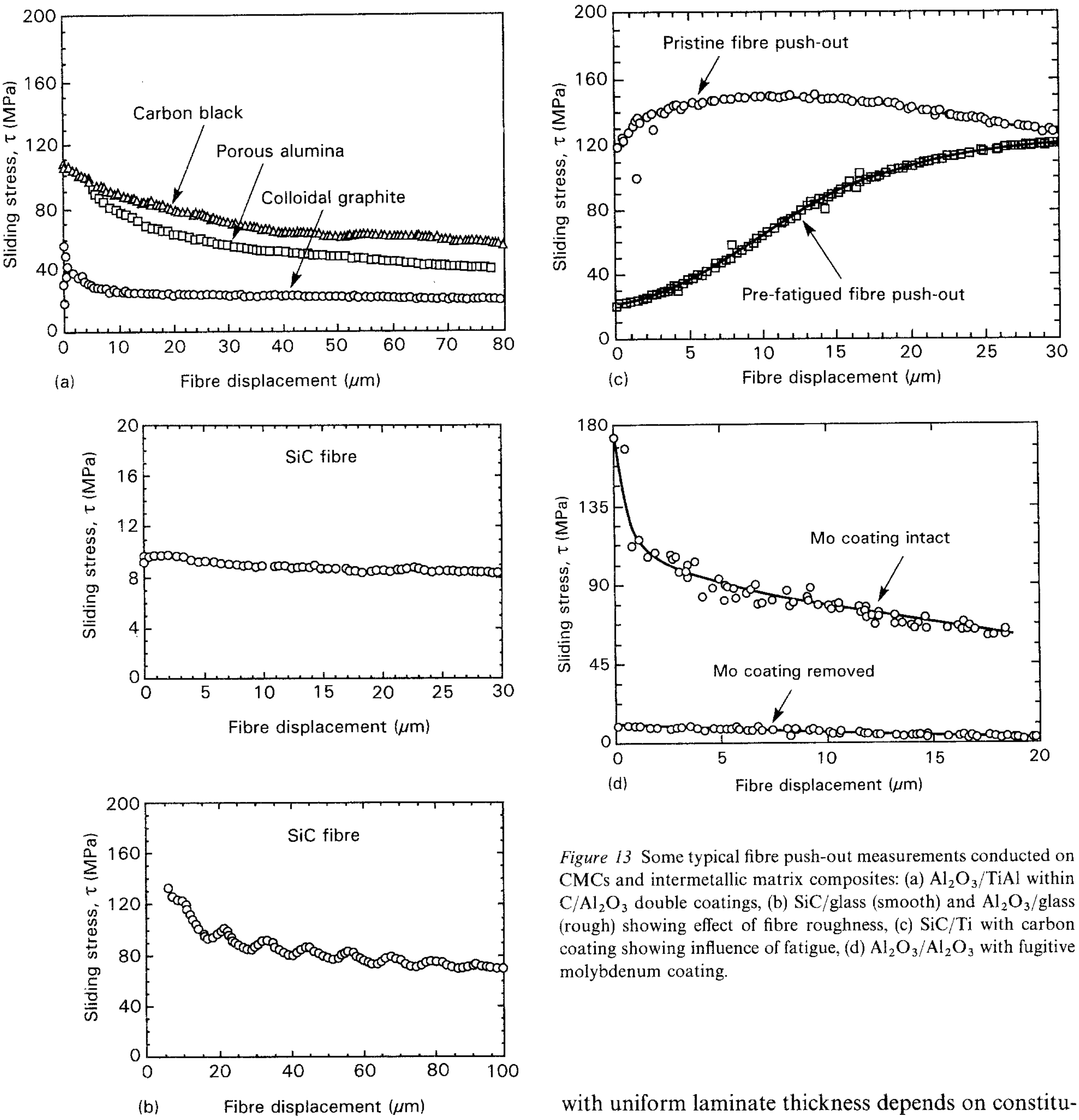

Figure 13 Some typical fibre push-out measurements conducted on CMCs and intermetallic matrix composites: (a) Al_2O_3/TiAl within C/Al_2O_3 double coatings, (b) SiC/glass (smooth) and Al_2O_3/glass (rough) showing effect of fibre roughness, (c) SiC/Ti with carbon coating showing influence of fatigue, (d) Al_2O_3/Al_2O_3 with fugitive molybdenum coating.

phenomenon [18, 49] and are environmentally desirable, provided that the matrix does not sinter to the fibres.

3. Residual stresses

3.1. Origin

Many composite properties are sensitive to the residual stress caused by the misfit strain, Ω, between fibre and matrix. Measurement of these stresses thus becomes an important aspect of the analysis and prediction of properties. These stresses arise at inter- and intra-laminate levels. Within a laminate, the axial stress in the matrix is [57]

$$q = (E_m/E_L)\sigma^T \tag{3}$$

where σ^T is the misfit stress, which is related to the misfit strain by (Tables III and IV) [17, 33]

$$\sigma^T = (c_2/c_1)E_m\Omega \tag{4}$$

The average residual stress, σ^R, in a 0/90 laminate, with uniform laminate thickness depends on constituent properties in approximate accordance with [58, 59]

$$\sigma^R \approx \frac{\Omega(1-f)E_L(1-E_m/E_L)}{(1+\nu_{LT})(1+E_L/E_T)} \tag{5}$$

Note that the residual stress $\sigma^R \rightarrow 0$ as the elastic properties become homogeneous ($E_f = E_m = E_L$). While connections between the residual stresses and constituent properties are rigorous, experimental determination is still necessary, because Ω is not readily predictable. In general, Ω includes terms associated with the thermal expansion difference, $\alpha_f - \alpha_m$, as well as volume changes that occur either upon crystallization or during phase transformations. For CVI systems, "intrinsic" stresses may also be present.

The temperature dependence can be assessed from the thermal expansion mismatch, by using

$$\Omega = \Omega_0 - (\alpha_m - \alpha_f)\Delta T_R \tag{6}$$

where ΔT_R is the temperature change from ambient and Ω_0 is the ambient misfit strain, measured using the procedures outlined below.

TABLE III Inventory of non-dimensional functions

Relative stiffness	$\xi \rightarrow fE_f/(1-f)E_m$
Sliding index	$\mathscr{T} \rightarrow \xi[\tau_0 E/\sigma E_f]^{1/2}$
Cyclic sliding index	$\Delta\mathscr{T} \rightarrow \xi[\tau_0 E/\Delta\sigma E_f]^{1/2}$
Loading index	$\mathscr{E} \rightarrow [2R\sigma/f\xi^2 a\tau_0]$
Cyclic loading indices	$\Delta\mathscr{E} \rightarrow [2R(\Delta\sigma)/f\xi^2 a\tau_0]$
	$\Delta\mathscr{E}_0 \rightarrow [2R(\Delta\sigma)/f\xi^2 a_0\tau_0]$
Bridging index	$\mathscr{E}_b \rightarrow [2R\sigma_b/f\xi^2 a\tau_0]$
Cyclic bridging indices	$\Delta\mathscr{E}_b \rightarrow [2R(\Delta\sigma_b)/f\xi^2 a\tau_0]$
	$\Delta\mathscr{E}_T \rightarrow [2RE_f(\alpha_f-\alpha_m)\Delta T/\xi^2 f\tau_0 a]$
Misfit index	$\Sigma_T \rightarrow \frac{\bar{\sigma}_T}{\bar{\sigma}_p} = (c_2/c_1)E_m\Omega/\bar{\sigma}_p$
Debond index	$\Sigma_i \rightarrow \frac{\bar{\sigma}_i}{\bar{\sigma}_p} = (1/c_1)(E_m\Gamma_i/R\bar{\sigma}_p^2)^{1/2} - \Sigma_T$
Hysteresis index	$\mathscr{H} \rightarrow b_2(1-a_1 f)^2 R\bar{\sigma}_p^2/4\bar{\ell}\tau E_m f^2$
Crack spacing index	$\mathscr{L} \rightarrow \Gamma_m(1-f)^2 E_f E_m/f\tau^2 E_L R$
Matrix cracking index	$M \rightarrow 6\tau\Gamma_m f^2 E_f/(1-f)E_m^2 R E_L$
Residual stress index	$\mathscr{Q} \rightarrow E_f f\Omega/E_L(1-\nu)$
Flaw index	$\mathscr{A} \rightarrow a_0 S^2/E_L\Gamma$
Flaw index for bridging	$\mathscr{A}_b \rightarrow [f/(1-f)]^2(E_f E_L/E_m^2)(a_0\tau/RS_u)$
Flaw index for pull-out	$\mathscr{A}_p \rightarrow (a_0/\bar{h})(S_p/E_L)$

TABLE IV Summary of HJ [33] constants for type II boundary conditions

$$a_1 = E_f/E$$

$$a_2 = \frac{(1-f)E_f[1+E_f/E]}{[E_f+(1-2\nu)E]}$$

$$b_2 = \frac{(1+\nu)E_m\{2(1-\nu)^2E_f+(1-2\nu)[1-\nu+f(1+\nu)](E_m-E_f)\}}{(1-\nu)E_f[(1+\nu)E_0+(1-\nu)E_m]}$$

$$b_3 = \frac{f(1+\nu)\{(1-f)(1+\nu)(1-2\nu)(E_f-E_m)+2(1-\nu)^2E_m\}}{(1-\nu)(1-f)[(1+\nu)E_0+(1-\nu)E_m]}$$

$$c_1 = \frac{(1-fa_1)(b_2+b_3)^{1/2}}{2f}$$

$$c_2 = \frac{a_2(b_2+b_3)^{1/2}}{2}$$

$$c_1/c_2 = \frac{1-a_1 f}{a_2 f}$$

with

$$E = fE_f + (1-f)E_m$$

$$E_0 = (1-f)E_f + fE_m$$

3.2. Measurement methods

Several experimental procedures can be used to measure the residual stresses. The four preferred methods involve (a) diffraction (X-ray or neutron), (b) beam deflection, (c) Raman microscopy and (d) permanent strain measurements. X-ray diffraction measurements give lattice strains. They have the limitation that the penetration depth is small, such that only near-surface information is obtained. Moreover, in composites, residual stresses are redistributed near surfaces [46]. Consequently, a full stress analysis is needed to relate the measured strains to either q or σ^R and the method has not been widely used.

Beam deflection and permanent strain measurements have the advantage that they provide information averaged over the composite. The results thus relate directly to the misfit strain, Ω. An experimental approach having high reliability involves curvature measurements on beams made from 0/90 composites [60]. For such material, polishing to produce one 0° layer and one 90° layer results in elastic bending (Fig. 14) (unless the material has a plain weave). The curvature, κ, is related to the residual stress by [60] (note there is a typographical error in Beyerle *et al.* [10]: the width w was omitted in their equation)

$$\sigma^R = E_L I_0 \kappa/t_b^2 w \qquad (7)$$

where I_0 is the second moment of inertia, t_b is the beam thickness and w the beam width.

When only one-dimensional material is available, the preferred approach is to measure the displacement, Δ^R, that occurs when a section of matrix, length L_d, is removed by dissolution (when possible). The residual stress in the matrix is then [61]

$$q = E_f f \Delta^R/(1-f)L_d \qquad (8)$$

Typical results are plotted on Fig. 15.

The Raman microscope can be used in two different modes to measure the residual stress. Both methods rely of shifts in Raman peaks induced by strain. A fluorescence spectroscopy method [62, 63] uses the fluorescence peak created by impurities and dopants (such as chromium) in oxide fibres, particularly Al_2O_3. The capability of the method has been

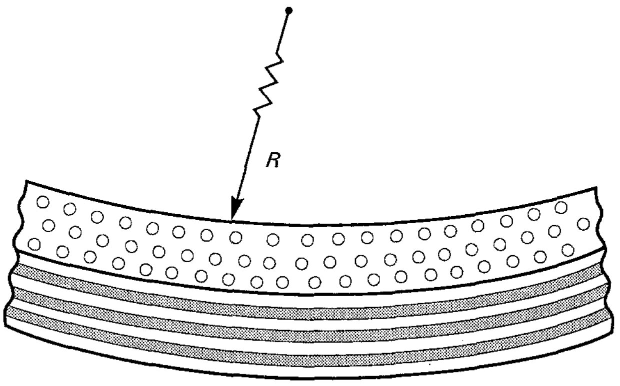

Figure 14 A schematic illustration of the beam bending effect used to evaluate the residual stress.

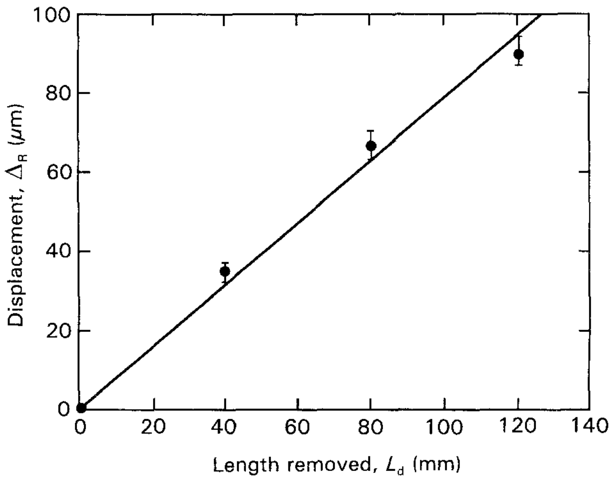

Figure 15 Displacements caused by matrix dissolution as a function of length removed.

TABLE V Important constituent properties for two typical CMCs: comparison between SiC/SiC and SiC/CAS [4]

Property	Material	
	SiC/CAS	SiC/SiC
Matrix modulus, E_m (GPa)	100	400
Fibre modulus, E_f (GPa)	200	200
Sliding stress, τ (MPa)	15–20	50–150
Debond energy, Γ_i ($\mathrm{J\,m^{-2}}$)	~ 0.1	~ 4
Residual stress, q (MPa)	80–100	50–100
Fibre strength, S_c (GPa)	2.0–2.2	1.3–1.6
Shape parameter, m	3.3–3.8	4.2–4.7
Matrix fracture energy, Γ_m ($\mathrm{J\,m^{-2}}$)	20–25	5–10

demonstrated for Al_2O_3 fibre-reinforced materials. The second method applies to ceramic fibres that contain carbon (such as Nicalon and carbon itself). It relies on the shifts in the peaks of the Raman spectrum for carbon [64]. The method has been applied to Nicalon fibre-reinforced CMCs.

The permanent strains that arise following tensile plastic deformation also relate to Ω. Measurement of these strains allows Ω to be assessed [17]. The relevant formulae are presented later in Section 5.4.

3.3. Experimental results

Experimental results are mostly consistent with a misfit strain that derives from the thermal expansion difference, $\alpha_m - \alpha_f$, and the cooling range from the processing temperature. Examples for SiC/CAS and $\mathrm{SiC/SiC_{CVI}}$ are given in Table V. However, volumetric changes that occur in the matrix contribute to Ω_0 when relatively low-temperature processing steps are used. For example, matrix crystallization of glass ceramics can induce substantial misfit [64].

4. Fibre properties

4.1. Load sharing

The strength properties of fibres are statistical in nature. Consequently, it is necessary to apply principles of weakest link statistics, which define the properties of fibres within a composite. The initial decision to be made concerns the potential for interactions between failed fibres and matrix cracks. It has generally been assumed that matrix cracks and fibre failure are non-interacting and that global load sharing (GLS) conditions obtain (however, a criterion for GLS breakdown has yet to be devised) [14, 18, 65, 66]. In this case, the stress along a material plane that intersects a failed fibre is equally distributed among all of the intact fibres. Experience has indicated that these assumptions are essentially valid for a variety of CMCs.

Subject to the validity of GLS, several key results have been derived. Two characterizing parameters emerge [67]: a characteristic length

$$\delta_c^{m+1} = L_0 (S_0 R/\tau)^m \qquad (9)$$

and a characteristic strength

$$S_c^{m+1} = S_0^m [L_0 \tau / R] \qquad (10)$$

where m is the shape parameter that characterizes the fibre strength distribution, S_0 the scale parameter, L_0 the reference length, and R the fibre radius. Various GLS results based on these parameters are described below.

When fibres do not interact, analysis begins by considering a fibre of length $2L$ divided into $2N$ elements, each of length δz. The probability that a fibre element will fail, when the stress is less than σ, is the area under the probability density curve [68, 69]

$$\delta\phi(\sigma) = \frac{\delta z}{L_0} \int_0^{\sigma} g(S)\,\mathrm{d}S \qquad (11)$$

where $g(S)\,\mathrm{d}S/L_0$ represents the number of flaws per unit length of fibre having a "strength" between S and $S + \mathrm{d}S$. The local stress, σ, is a function of both the distance along the fibre, z, and the reference stress, $\bar{\sigma}_b$. The survival probability, P_s, for all elements in the fibre of length $2L$ is the product of the survival probabilities of each element [70]

$$P_s(\bar{\sigma}_b, L) = \prod_{n=-N}^{N} [1 - \delta\phi(\bar{\sigma}_b, z)] \qquad (12)$$

where $z = n\delta z$ and $L = N\delta z$. Furthermore, the probability, Φ_s, that the element at z will fail when the peak, reference stress is between $\bar{\sigma}_b$ and $\bar{\sigma}_b + \delta\bar{\sigma}_b$, but not when the stress is less than $\bar{\sigma}_b$, is the change in $\delta\phi$ when the stress increased by $\delta\bar{\sigma}_b$ divided by the survival probability up to σ_b, given by [68, 69, 71]

$$\Phi_s(\bar{\sigma}_b, z) = [1 - \delta\phi(\bar{\sigma}_b, z)]^{-1} \left[\frac{\partial\phi(\bar{\sigma}_b, z)}{\partial\bar{\sigma}_b}\right] \mathrm{d}\bar{\sigma}_b \qquad (13)$$

Denoting the probability density function for fibre failure by $\Phi(\bar{\sigma}_b, z)$, the probability that fracture occurs at a location z, when the peak stress is $\bar{\sigma}_b$, is governed by the probability that all elements survive up to a peak stress $\bar{\sigma}_b$, but that failure occurs, at z, when the stress reaches $\bar{\sigma}_b$ [71–73]. It is given by the product of Equation 12 with Equation 13

$$\Phi_s(\bar{\sigma}_b, z)\delta\bar{\sigma}_b\delta z = \frac{\prod_{-N}^{N} [1 - \delta\phi(\bar{\sigma}_b, z)]}{[1 - \delta\phi(\bar{\sigma}_b, z)]} \times \left[\frac{\partial\delta\phi(\bar{\sigma}_b, z)}{\partial\bar{\sigma}_b}\right] \mathrm{d}\bar{\sigma}_b \qquad (14)$$

While the above results are quite general, it is convenient to use a power law to represent $g(S)$

$$\int_0^{\sigma} g(S)\mathrm{d}S = (\sigma/S_0)^m \qquad (15)$$

Alternative representations of $g(S)$ are not warranted at the present level of development. Using this assumption, Equation 14 becomes [72]

$$\Phi(\bar{\sigma}_b, z) = \exp\left\{-2\int_0^L \left[\frac{\sigma(\bar{\sigma}_b, z)}{S_0}\right]^m \frac{\mathrm{d}z}{L_0}\right\} \times \left(\frac{2}{L_0}\right) \frac{\partial}{\partial\bar{\sigma}_b} \left[\frac{\sigma(\bar{\sigma}_b, z)}{S_0}\right]^m \qquad (16)$$

This basic result has been used to obtain solutions for several problems [14, 72, 74] described below.

4.2. The ultimate tensile strength

When multiple matrix cracking precedes failure of the fibres in the 0° bundles, the load along each matrix crack plane is borne entirely by the fibres. Nevertheless, the matrix has a crucial role, because stress transfer between the fibres and the matrix still occurs through the sliding resistance, τ. Consequently, some stress can be sustained by the failed fibres. This stress transfer process occurs over a distance related to the characteristic length, δ_c. As a result, the stresses on the intact fibres along any plane through the material are less than those experienced within a "dry" fibre bundle (in the absence of matrix). The transfer process also allows the stress in a failed fibre to be unaffected at distance $\gtrsim \delta_c$ from the fibre fracture site (Fig. 16). Consequently, composite failure requires that fibre bundle failure occurs within δ_c [14]. This phenomenon leads to an ultimate tensile strength (UTS) independent of gauge length, L_g, provided that $L_g > \delta_c$. (At small gauge lengths ($L_g < \delta_c$), the UTS becomes gauge length dependent and exceeds S_u [66].) The magnitude of the UTS can be computed by first evaluating the average stress on all fibres, failed plus intact, along an arbitrary plane through the material. Then, by differentiating with respect to the stress on the intact fibres, in order to obtain the maximum, the UTS becomes

$$S_g = f_f S_c F(m) \tag{17a}$$

with

$$F(m) = [2/(m+1)]^{1/(m+1)}[(m+1)/(m+2)] \tag{17b}$$

It is of interest to compare this result to that found for a "dry" bundle. Then, the "fibre bundle" strength, S_b, depends on the gauge length in accordance with [75]

$$S_b = f S_0 (L_0/L_g)^{1/m} e^{-1/m} \tag{17c}$$

In all cases, $S_g > S_b$.

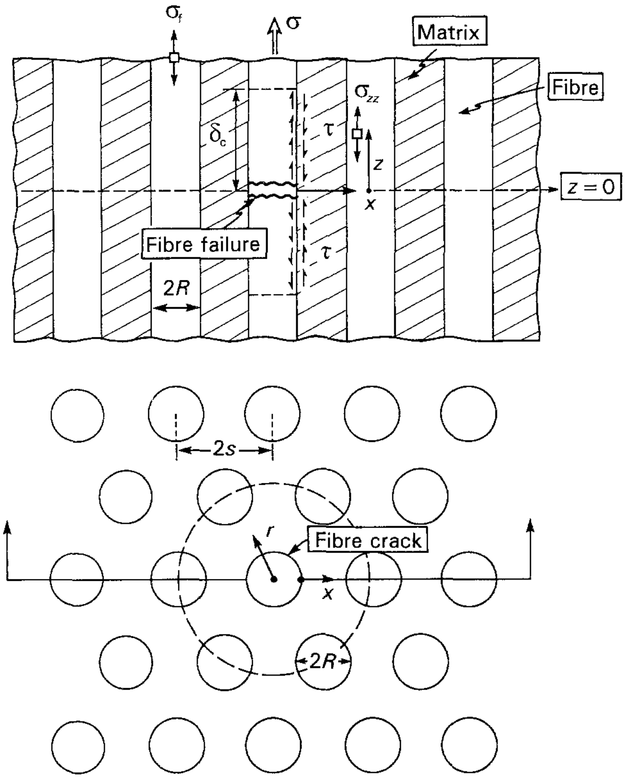

Figure 16 A schematic illustration of the load transfer process from failed fibres.

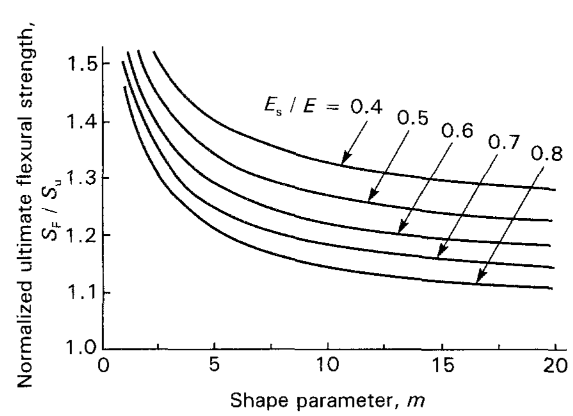

Figure 17 Relationship between ultimate strengths measured in flexure and tension.

As the load increases, the fibres fail systematically, resulting in a characteristic fibre fragment length. At composite failure, there can be multiple cracks within some fibres. The existence of many fibre fragments is still compatible with a high ultimate tensile strength (a good analogy being the strength of a wire rope). However, a diminished creep strength may ensue, as elaborated below (Section 9).

The above results are applicable to tensile loading. When a bending moment is applied, the behaviour is modified. In this case, the stress is redistributed by both matrix cracking and fibre failure. Predictions of the UTS in pure flexure (Fig. 17) indicate the salient phenomena [66].

4.3. Fibre pull-out

In CMCs with good composite properties, fibre pull-out is evident on the tensile fracture surfaces [73]. Various measurements conducted on these surfaces provide valuable information. Regions with highly correlated fibre failures, with minimal pull-out, are indicative of manufacturing flaws. Such flaws often occur in regions where fibre coating problems existed. In zones where fibre failures are uncorrelated, the distribution of fibre pull-out lengths provides essential information. The pull-out lengths are related explicitly to the stochastics of fibre failure [14, 72]. The basic realization is that, on average, fibres do not fail on the plane of the matrix crack, even though the stress in the fibres has its maximum value at this site. This unusual phenomenon relies exclusively on statistics, wherein the locations of fibre failure may be identified as a distribution function that depends on the shape parameter, m. Furthermore, the mean pull-out length, $\bar{h}$, has a connection with the characteristic length, δ_c. Consequently, a functional dependence exists, dictated by the non-dimensional parameters, $\tau\bar{h}/RS_c$ and m. If it is assumed that sliding is controlled by a constant stress, τ, dictated by roughness and friction and that the shape parameter for the fibres is unaffected by the details of the friction, the pull-out length can be expressed as [14]

$$\bar{h}\tau/RS_c = \lambda(m) \qquad (18)$$

There are two bounding solutions for the function λ (Fig. 18). Composite failure subject to multiple matrix cracking gives the upper bound. Failure in the presence of a single crack gives the lower bound.

Because of pull-out, a frictional pull-out resistance exists, which allows the material to sustain load, beyond the UTS. The associated "pull-out" strength, S_p, is an important property of the composite (Fig. 19). The strength, S_p, is given by [76]

$$\begin{aligned} S_p &= 2\tau f\bar{h}/R \\ &\equiv 2fS_c\lambda(m) \qquad (19) \end{aligned}$$

4.4. Influence of flaws

The preceding results are applicable provided that there are no unbridged segments along the matrix crack. Unbridged regions concentrate the stress in the adjacent fibres and weaken the composite [12, 77, 78]. Simple linear scaling considerations indicate that the diminished UTS depends on a non-dimensional flaw index (Table III)

$$\mathscr{A} = a_0 S_g^2/E_L\Gamma \qquad (20)$$

where Γ is the "toughness", reflected in the area under the stress–displacement curve for the bridging fibres, E is Young's modulus and $2a_0$ is the length of the unbridged segment. The flaw index, $\mathscr{A}$, can be specified, based on Γ, using large-scale bridging mechanics (LSBM). The dependence of the UTS, designated S^*, on the flaw index $\mathscr{A}$ can be determined from LSBM by numerical analysis [78] (Fig. 19). The results reveal that the ratio S_p/S_g, is an important factor. Notably, relatively large values of the "pull-out" strength alleviate the strength degradation caused by unbridged cracks.

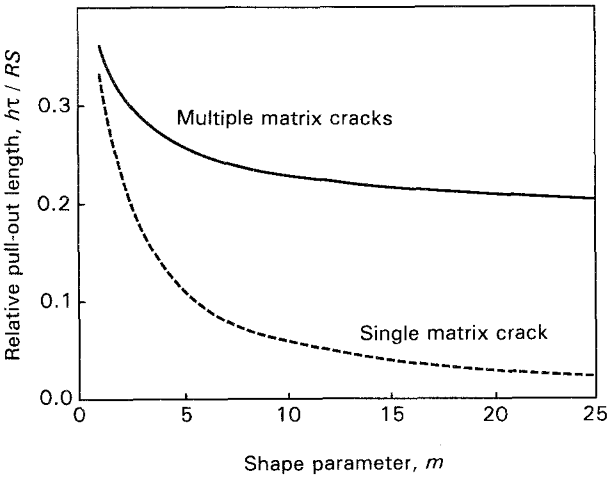

Figure 18 Bounds on the relationship between the non-dimensional fibre pull-out length and the Weibull modulus.

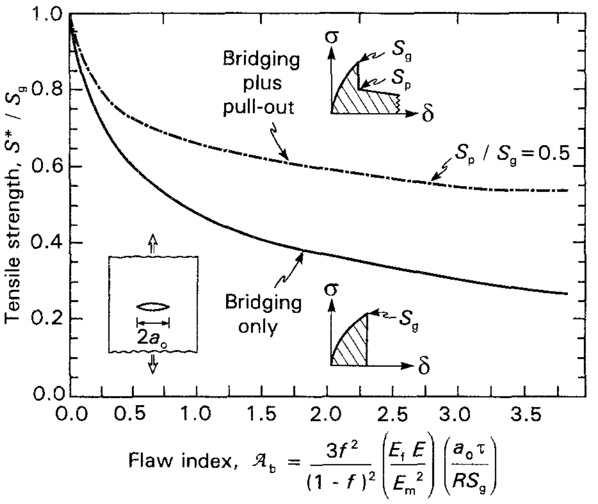

Figure 19 The effect of unbridged regions, length $2a_0$, on the ultimate tensile strength.

4.5. *In situ* strength measurements

In general, composite consolidation degrades fibre properties and it becomes necessary to devise procedures that allow determination of S_c and m to be evaluated relevant to the fibres within the composite. This is a challenging problem. In some cases, it is possible to dissolve the matrix without further degrading the fibres and then measure the bundle strength [79]. This is not feasible with most CMCs of interest. The following two alternatives exist.

Some fibres exhibit fracture mirrors when they fail within a composite (e.g. Nicalon). A semi-empirical calibration has been developed that relates the mirror radius, a_m, to the *in situ* fibre tensile strength, S, given by (Fig. 20).

$$S = 3.5(E_f\Gamma_f/a_m)^{1/2} \qquad (21)$$

where Γ_f is the fracture energy of the fibre [7, 29, 80]. By measuring S on many fibres, and then plotting the

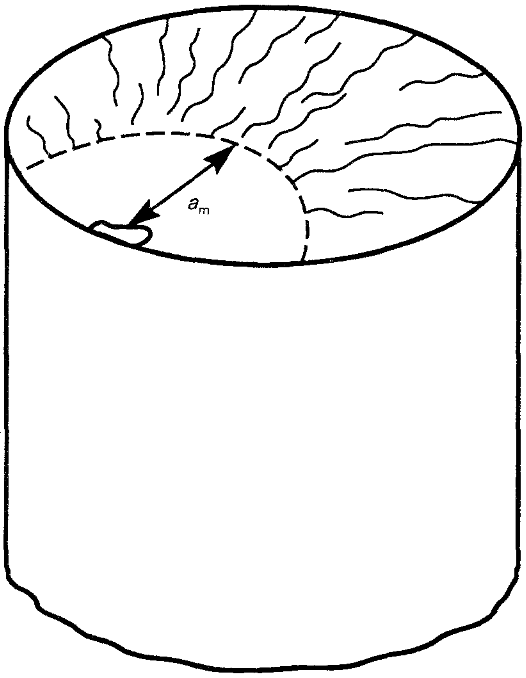

Figure 20 A schematic illustration of a fracture mirror and the dimension a_m used to predict the *in situ* strength.

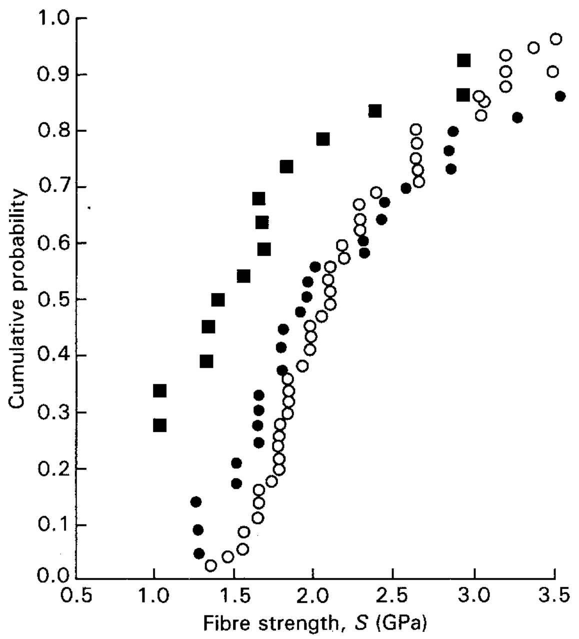

Figure 21 *In situ* strength distributions measured for Nicalon fibres in three CMCs, using the fracture mirror approach. (○) SiC/C, (●) SiC/CAS, (■) SiC/SiC_{CVI}.

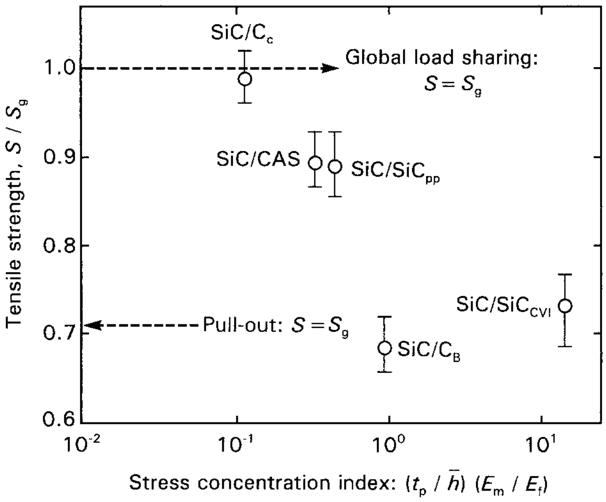

Figure 22 Comparison of the measured UTS with S_g predicted from GLS (Equation 17a) plotted against a stress concentration index. Note that h is inversely proportional to τ.

cumulative distribution, both the shape parameter, m, and the characteristic *in situ* fibre strength, S_c, can be ascertained. Results of this type have been obtained for Nicalon fibres in a variety of different matrices (Fig. 21). This compilation indicates the sensitivity of the *in situ* strength to the composite processing approach. This fibre strength variation is also reflected in the range in UTS found among CMCs reinforced with these fibres (Fig. 5).

A problem in implementing the fracture mirror approach arises when a significant fraction of the fibres does not exhibit well-defined mirrors. Those fibres that do not have mirrors usually have a smooth fracture surface. It has thus been assumed that these are the weakest fibres in the distribution [61, 80]. The order statistics used to determine $G(S)$ are adjusted accordingly. This assumption has not been validated.

The only alternative approaches for evaluating S_c, known to the authors, are based on pull-out and fragment length measurements [28]. Both quantities depend on S_c and m, as well as τ. Consequently, if τ is known, S_c can be determined. For example, m can be evaluated by fitting the distribution of fibre pull-out lengths to the calculated function. Then, S_c can be obtained for the mean value, $\bar{h}$, using Equation 12. This approach has not been extensively used and checked.

4.6. Experimental results

Several studies have compared the multiple matrix cracking GLS prediction, S_g (Equations 17a–c) with the UTS measured for either one- or two-dimensional CMCs. In most cases, the UTS is in the range (0.7–1) S_g, as indicated in Fig. 22. The two obvious discrepancies are the SiC/SiC_{CVI} material and one of the SiC/C materials. In these cases, the GLS predictions overestimate the measured values. Moreover, τ is relatively large for both materials, as reflected in the magnitude of the stress concentration index (Fig. 22). Two factors have to be considered as these results are interpreted. (i) In some materials, the fraction of fibres that exhibit mirrors is not large enough to provide confidence in the inferred values of S_c and m. This issue is a particular concern for the SiC/SiC_{CVI} material. (ii) In other materials, manufacturing flaws are present that provide unbridged crack segments, which cause the UTS to be smaller than S_g (Section 4.4).

With the above provisos, it is surprising that the UTS measured for several two-dimensional CMCs is close to the GLS prediction. In these materials, cracks exist in the 90° plies at low stresses and these cracks should concentrate the stress on the neighbouring fibres in the 0° plies. The UTS would thus be expected to follow the strength degradation diagram (Fig. 19). That this weakening does not occur remains to be explained. It probably reflects the influence on the strength degradation of elastic anisotropy, as well as pull-out (Fig. 19).

5. Matrix cracking in unidirectional materials

The development of damage in the form of matrix cracks within one-dimensional CMCs subject to tensile loading has been traced by direct optical observations on specimens with carefully polished surfaces and by acoustic emission detection [6, 8, 55, 61], as well as by ultrasonic velocity measurements [81]. Interrupted tests, in conjunction with sectioning and SEM observations, have also be used. Analyses of the matrix damage found in one-dimensional CMCs provides the basis upon which the behaviour of two- and three-dimensional CMCs may be addressed. The matrix cracks are found to interact with predominantly intact fibres, subject to interfaces that debond and slide. This process commences at a lower bound stress, $\bar{\sigma}_{mc}$. The crack density increases with increase in stress above $\bar{\sigma}_{mc}$ and may eventually attain a saturation spacing, $\bar{d}_s$, at stress $\bar{\sigma}_s$. The details of crack

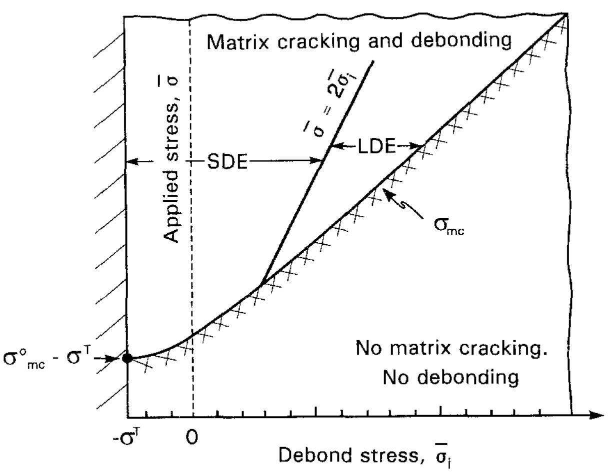

Figure 23 A mechanism map representing the various modes of interface response.

evolution are governed by the distribution of matrix flaws. The matrix cracks reduce the unloading elastic modulus, $\bar{E}$, and also induce a permanent strain, ε_0 (Fig. 9). Relationships between $\bar{E}$, ε_0 and constituent properties provide the key connections between processing and macroscopic performance, via the properties of the constituents.

The deformations caused by matrix cracking, in conjunction with interface debonding and sliding, exhibit three regimes that depend on the magnitude of the debond stress, $\bar{\sigma}_i$. In turn, $\bar{\sigma}_i$ depends on the debond energy through the relationship [33]

$$\begin{aligned} \bar{\sigma}_i &= (1/c_1)(E_m\Gamma_i/R)^{1/2} - \sigma^T \\ &\equiv \sigma_D - \sigma^T \qquad (22a) \end{aligned}$$

which has a useful non-dimensional form

$$\Sigma_i = \bar{\sigma}_i/\sigma \qquad (22b)$$

A mechanism map that identifies the three regimes is shown in Fig. 23 [17]. When $\Sigma_i > 1$, debonding does not occur, whereupon matrix crack growth is an entirely elastic phenomenon. When $\Sigma_i < \frac{1}{2}$, small debond energy (SDE) behaviour arises. The characteristic of SDE is that the reverse slip length at the interface, upon complete unloading, exceeds the debond length. For SDE, Γ_i is typically small and does not affect certain properties, such as the hysteresis loop width. The term SDE is thus used, loosely, to represent the behaviour expected when $\Gamma_i \approx 0$. An intermediate, large debond energy (LDE) regime also exists, when $\frac{1}{2} \leqslant \Sigma_i \leqslant 1$. In this situation, reverse slip is impeded by the debond.

5.1. Basic mechanics

The approach used to simulate mode I cracking under monotonic loading is to define tractions σ_b acting on the crack faces, induced by the fibres (Fig. 1) and to determine their effect on the crack tip by using the J integral [31, 57]

$$\mathcal{G}_{tip} = \mathcal{G} - \int_0^u \sigma_b \mathrm{d}u \qquad (23)$$

where $\mathcal{G}$ is the energy release rate and u is the crack opening displacement. Cracking is considered to proceed when $\mathcal{G}_{tip}$ attains the pertinent fracture energy. Because the fibres are not failing, the crack growth criterion involves matrix cracking only. A lower bound is given by [57, 82]

$$\mathcal{G}_{tip} = \Gamma_m(1-f) \qquad (24)$$

with Γ_m being the matrix toughness. Upon crack extension, $\mathcal{G}$ becomes the crack growth resistance, Γ_R, whereupon

$$\Gamma_R = \Gamma_m(1-f) + \int_0^u \sigma_b \mathrm{d}u \qquad (25)$$

A traction law, $\sigma_b(u)$, is now needed to predict Γ_R. A law based on frictional sliding along debonded interfaces has been used most extensively and appears to provide a resonable description of many of the observed mechanical responses (Equation 1). The traction law also includes effects of the interface debond energy, Γ_i [33]. For many CMCs, Γ_i is small, as reflected in the magnitude of the debond stress, Σ_i.

For a constant sliding stress, τ_0, the sliding distance, l, in the absence of fibre failure, is related to the crack surface tractions, σ_b, by [13, 31, 33]

$$\ell = [RE_m(1-f)/2\tau_0 E_f f](\sigma_b - \bar{\sigma}_i) \qquad (26)$$

The sliding length is, in turn, related to the crack opening displacement. The corresponding traction law is [17, 31, 57]

$$\sigma_b - \bar{\sigma}_i = (2\xi\tau_0 E_L f u/R)^{1/2} \qquad (27)$$

where ξ is defined in Table III.

The matrix fracture behaviour can also be described by using stress intensity factors, K. This approach is more convenient than the J integral in some cases: particularly for short cracks and for fatigue [31, 83]. To apply this approach, it is first necessary to specify the contribution to the crack opening induced by the applied stress, as well as that provided by the bridging fibres. For a plane strain crack of length $2a$ in an infinite plate, the contribution due to the applied stress is [84]

$$u_\infty = (4/E_L)\sigma(a^2 - x^2)^{1/2} \qquad (28a)$$

and that caused by bridging is

$$u_b = -(4/E_L)\int_0^a \sigma_b(\hat{x})H\,\mathrm{d}\hat{x} \qquad (28b)$$

with H being a weight function. The net crack opening displacement is

$$u = u_\infty + u_b \qquad (29)$$

The contribution to K from the bridging fibres is obtained using [84]

$$K_b = -2\left(\frac{2}{\pi}\right)^{1/2} \int_0^a \frac{\sigma_b(x)\mathrm{d}x}{(a^2 - x^2)^{1/2}} \qquad (30)$$

with σ_b given by Equation 27. The shielding associated with K_b leads to a tip stress intensity factor

$$K_{tip} = K + K_b \qquad (31)$$

where K depends on the loading and specimen geometry.

A criterion for matrix crack extension, based on K_{tip}, is needed. For this purpose, to be consistent with the energy criterion (Equation 24), the critical stress intensity factor is taken to be

$$K_{\mathrm{tip}} \;=\; [E\Gamma_{\mathrm{m}}(1-f)]^{1/2} \tag{32}$$

Then, the two approaches (K and $\mathscr{G}$) lead to the same steady-state matrix cracking stress.

5.2. The matrix cracking stress

The preceding basic results can be used to obtain solutions for matrix cracking [13, 45, 57, 82, 83]. Present understanding involves the following factors. Because the fibres are intact, a steady-state condition exists wherein the tractions on the fibres in the crack wake balance the applied stress. This special case may be addressed by integrating Equation 23 up to a limit $u = u_0$. This limit is obtained from Equation 27 by equating σ_{b} to σ. For SDE, this procedure gives [57]

$$\mathscr{G}^0_{\mathrm{tip}} \;=\; \frac{(\sigma+\sigma^{\mathrm{T}})^3 E_m^2(1-f)^2 R}{6\tau_0 f^2 E_{\mathrm{f}} E_{\mathrm{L}}^2} \tag{33}$$

A lower bound to the matrix cracking stress, σ_{mc}, is then obtained by invoking Equation 24 such that [57]

$$\begin{aligned}\bar{\sigma}_{\mathrm{mc}} \;&=\; E_{\mathrm{L}}\left[\frac{6\tau\Gamma_{\mathrm{m}} f^2 E_{\mathrm{f}}}{(1-f)E_{\mathrm{m}}^2 R E_{\mathrm{L}}}\right]^{1/3} - \sigma^{\mathrm{T}} \\ &\equiv\; \sigma^0_{\mathrm{mc}} - \sigma^{\mathrm{T}} \end{aligned}\tag{34}$$

In some cases, small matrix cracks can form at stresses below $\bar{\sigma}_{\mathrm{mc}}$ [6]. These occur either within matrix-rich regions or around processing flaws. The non-linear composite properties are usually dominated by fully developed matrix cracks that form at stresses above $\bar{\sigma}_{\mathrm{mc}}$. However, these small flaws may provide access of the atmosphere to the interfaces and cause degradation.

Analogous results can be obtained using stress intensity factors [31, 83]. For a small centre crack in a tensile specimen, ($K = \sigma/(\pi a)^{1/2}$). Equations 30 and 32 give a steady-state result, at large crack lengths [83]

$$K_{\mathrm{tip}} \;=\; \frac{\sigma R^{1/2}}{6^{1/2}\mathscr{T}} \tag{35}$$

where $\mathscr{T}$ is a sliding index defined in Table III. When combined with the fracture criterion (Equation 32), the matrix cracking stress, $\bar{\sigma}_{\mathrm{mc}}$ is predicted to be the same as that given by Equation 34.

The K approach may also be used to define a transition crack length, a_{t}, above which steady-state applies. This transition length is given by [31, 83]

$$a_{\mathrm{t}}/R \approx E_{\mathrm{m}}[\Gamma_{\mathrm{m}}(1+\xi)^2(1-f)^4/\tau_0^2 f^4 E_{\mathrm{f}}^2 R]^{1/3} \tag{36}$$

Namely, when the initial flaw size $a_{\mathrm{i}} > a_{\mathrm{t}}$, cracking occurs at $\sigma = \bar{\sigma}_{\mathrm{mc}}$. Conversely, when the initial flaws are small, $a_{\mathrm{i}} < a_{\mathrm{t}}$, it has been shown that [83]

$$K_{\mathrm{tip}} \approx K\left[1 - \frac{3.05}{\mathscr{E}}(\mathscr{E}+3.3)^{1/2} + \frac{5.5}{\mathscr{E}}\right] \tag{37}$$

where $\mathscr{E}$ is a loading index defined as (Table III)

$$\mathscr{E} = 2R(1-f)^2 E_{\mathrm{m}}^2\sigma/E_{\mathrm{f}} E\tau_0 a f^2(1-\nu^2) \tag{38}$$

This result for K_{tip}, when combined with Equation 32, gives a revised matrix cracking stress, which exceeds $\bar{\sigma}_{\mathrm{mc}}$.

Analogous results can be derived for the LDE regime. In this case, Equation 27 may be used with Equation 23 to derive an energy release rate, which can be combined with the fracture criterion (Equation 24) to predict σ_{mc}. The result is contained within the implicit formula

$$\begin{aligned}&[(\sigma_{\mathrm{mc}}+\sigma^{\mathrm{T}})/\sigma^0_{\mathrm{mc}}]^3 - 3[(\sigma_{\mathrm{mc}}+\sigma^{\mathrm{T}})/\sigma^0_{\mathrm{mc}}](\sigma_{\mathrm{D}}/\sigma^0_{\mathrm{mc}})^2 \\ &\qquad + 3(\sigma_{\mathrm{D}}/\sigma^0_{\mathrm{mc}})^3 = 1\end{aligned}\tag{39}$$

The trend in σ_{mc} with debond stress is plotted on Fig. 23.

5.3. Crack evolution

The evolution of additional cracks at stresses above $\bar{\sigma}_{\mathrm{mc}}$ is less well understood, because two factors are involved: screening and statistics [30, 85]. When the sliding zones between neighbouring cracks overlap, screening occurs and $\mathscr{G}_{\mathrm{tip}}$ differs from, $\mathscr{G}^0_{\mathrm{tip}}$. The relationship is dictated by the location of the neighbouring cracks. When a crack forms midway between two existing cracks with a separation $2d$, subject to SDE, $\mathscr{G}_{\mathrm{tip}}$ is related to $\mathscr{G}^0_{\mathrm{tip}}$ by [30]

$$\mathscr{G}_{\mathrm{tip}}/\mathscr{G}^0_{\mathrm{tip}} \;=\; 4(d/2\ell)^3 \qquad \text{for } 0 \leqslant d/\ell \leqslant 1 \tag{40}$$

and

$$\mathscr{G}_{\mathrm{tip}}/\mathscr{G}^0_{\mathrm{tip}} \;=\; 1 - 4(1-d/2\ell)^3 \qquad \text{for } 0 \leqslant d/l \leqslant 2 \tag{41}$$

When d is sufficiently small $\mathscr{G}_{\mathrm{tip}}$ is independent of the stress. Once this occurs, $\mathscr{G}_{\mathrm{tip}}$ cannot increase and is unable to again satisfy the matrix crack growth criterion (Equation 24). This occurs with spacing, $\bar{d}_{\mathrm{s}}$, at an associated stress $\bar{\sigma}_{\mathrm{s}}$ (Fig. 11). This saturation spacing is given for SDE materials by

$$\bar{d}_{\mathrm{s}}/R \;=\; \chi[\Gamma_{\mathrm{m}}(1-f)^2 E_{\mathrm{f}} E_{\mathrm{m}}/f\tau_0^2 E_{\mathrm{L}} R]^{1/3} \tag{42}$$

Note that this result is independent of the residual stress, because the terms containing $(\sigma_{\mathrm{b}}+\sigma^{\mathrm{T}})$ in Equations 26 and 33 cancel when inserted into Equation 40. The coefficient χ depends on the spatial aspects of crack evolution: periodic, random, etc. Simulations for spatial randomness indicate that $\chi = 1.6$ [30].

In addition to these screening effects, the actual evolution of matrix cracks at stresses above σ_{mc} is governed by statistics that relate to the size and spatial distribution of matrix flaws. If this distribution is known, the evolution can be predicted. Such statistical effects arise when the matrix flaws are smaller than the transition size, a_{t}, at which steady-state commences (Equation 36). In this case, a flaw size distribution must be combined with the short crack solution for

K_{tip} (Equation 37) in order to predict crack evolution. At the simplest level, this has been done by assuming an exponential distribution for the matrix flaw size [86]

$$\phi = \exp(L/L_*)(a_t/a)^{\omega} \quad (43)$$

where ϕ is the fraction of flaws in a composite, length L, having size larger than a, ω is a shape parameter related to the Weibull modulus for the matrix, ($\omega = m_m/2$) and L_* is a scale parameter

$$L_* = \lambda_s \ell_{\mathrm{mc}} \quad (44)$$

with ℓ_{mc} being the slip distance at $\sigma = \sigma_{\mathrm{mc}}$ and λ_s a flaw-size coefficient. The condition $\lambda_s \lesssim 1$ corresponds to a high density of matrix flaws already large enough to be at steady-state. Conversely, $\lambda_s > 1$ refers to a situation wherein most matrix flaws are smaller than the transition size, a_t.

Simulations can be performed in which the key variables are the shape parameter ω and the scale parameter λ_s. The simulated crack densities (Fig. 24a) indicate a sudden burst of cracking at $\sigma = \sigma_{\mathrm{mc}}$, when $\lambda_s < 1$, followed by a gradual increase with continued elevation of the stress. In contrast, when $\lambda_s \gg 1$, the cracks evolve more gradually with stress, reaching saturation at substantially higher levels of stress. (Nevertheless, the saturation spacing remains insensitive to λ_s [86].) These simulated behaviours are qualitatively similar to those measured by experiment (Fig. 24b). Moreover, the values found for ω are in a reasonable range ($m_m = 2\omega \approx 4$–8). However, because ω and λ_s are not known, a priori, in practice this approach becomes a fitting procedure rather than a predictive model. Despite this limitation, it has been found that a simple formula can be used to approximate crack evolution in most CMCs [4], given by (Fig. 24b)

$$\bar{d} \approx \bar{d}_s \frac{[\bar{\sigma}_s/\sigma_{\mathrm{mc}} - 1]}{[\bar{\sigma}/\sigma_{\mathrm{mc}} - 1]} \quad (45)$$

Analogous results can be derived for LDE, with the debond length given by Equation 28b and the reference energy release rate by Equation 39.

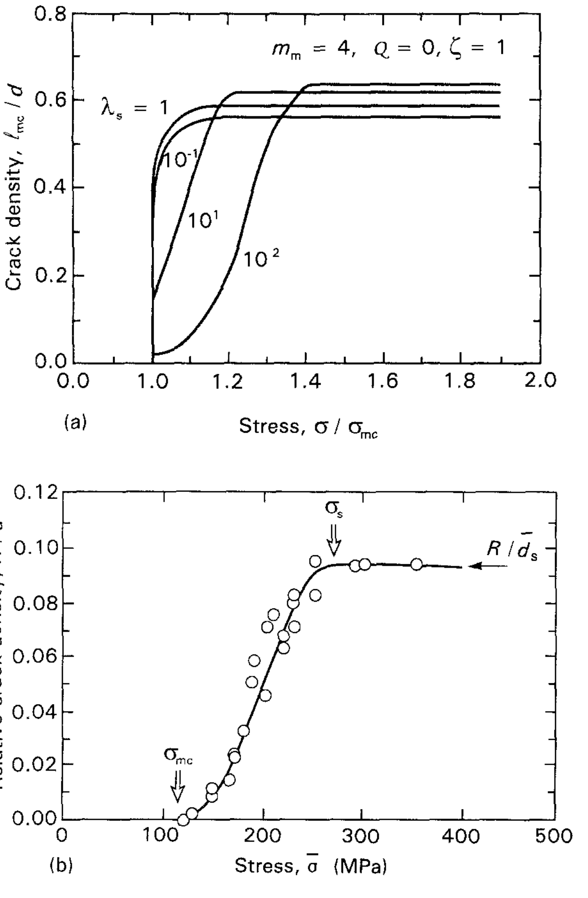

Figure 24 (a) Simulation of crack evolution for various matrix flaw distributions characterized by λ_S when the shape parameter $\omega = 2$. (b) Evolution of matrix crack density with stress for unidirectional SiC/CAS.

5.4. Constitutive law

Analyses of the plastic strains caused by matrix cracks, combined with calculations of the compliance change, provide a constitutive law for the material. The important parameters are the permanent strain, ε_0, and the unloading modulus, $\bar{E}$. These quantities, in turn, depend on several constituent properties; the sliding stress, τ, the debond energy, Γ_i, and the misfit strain, Ω. The most important results are summarized below.

Matrix cracks increase the elastic compliance. Numerical calculations indicate that the unloading elastic modulus, E^*, is given by [20]

$$E_L/E^* - 1 = (R/\bar{d})\mathscr{B}(f, E_f/E_m) \quad (46)$$

where $\mathscr{B}$ is the function plotted in Fig. 25. The matrix cracks also cause a permanent strain associated with relief of the residual stress. This strain, ε^*, related to the modulus and the misfit stress by (Fig. 26) [20]

$$\varepsilon^* \equiv \sigma^T(1/E^* - 1/E_L) \quad (47)$$

The preceding effects occur without interface sliding. The incidence of sliding leads to plastic strains that superpose on to ε^*. The magnitude of these strains depends on Σ_i (Fig. 23) and on the stress relative to the saturation stress, $\bar{\sigma}_s$. Because saturation arises when the slip zones from neighbouring cracks overlap, the

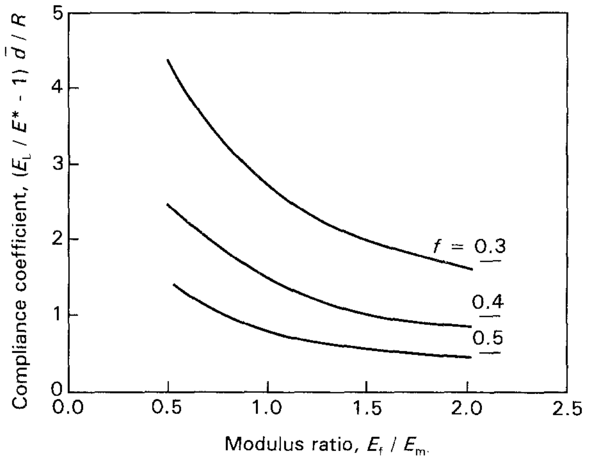

Figure 25 Effects of modulus mismatch and fibre volume fraction on the elastic compliance.

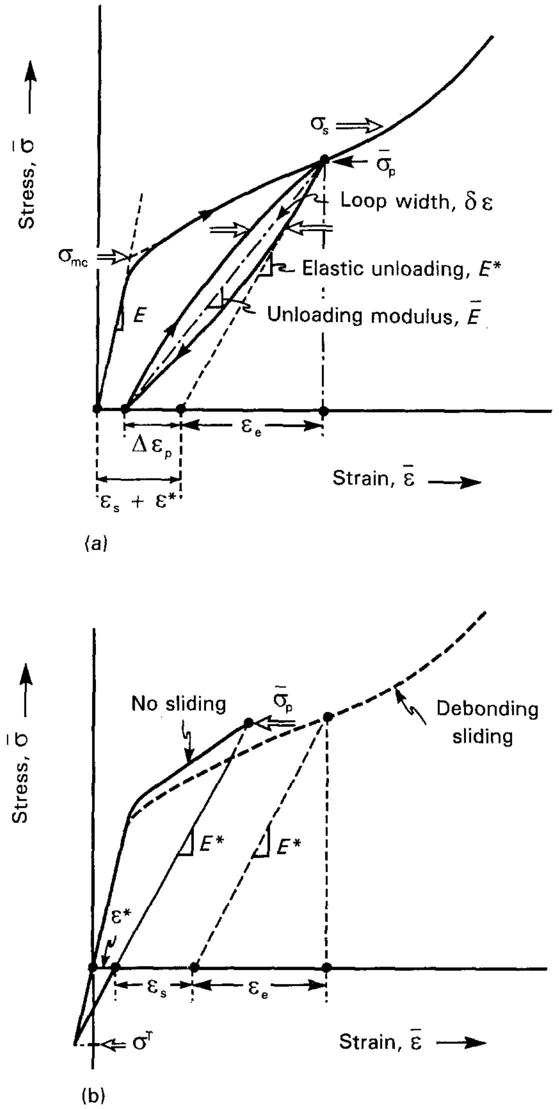

Figure 26 Basic parameters involved in the stress–strain behaviour of CMCs. (a) Interfaces that debond and slide subject to SDE, (b) Behaviour in the absence of debonding and sliding.

saturation stress may first be estimated from Equation 26 by equating ℓ and $\bar{d}_s$. This gives

$$\sigma_s - \bar{\sigma}_i \approx \frac{2\tau_0 \bar{d}_s E_f f}{R E_m (1 - f)} \qquad (48)$$

5.4.1. Stresses below saturation

5.4.1.1. Small debond energy. For SDE, when $\sigma < \bar{\sigma}_s$, the unloading modulus $\bar{E}$ depends on τ_0, but is independent of Γ_i and Ω. However, the permanent strain, ε_0, depends on Γ_i and Ω, as well as τ_0. These differing dependencies of $\bar{E}$ and ε_0 on constituent properties have the following two implications. (i) To simulate the stress–strain curve, both ε_0 and $\bar{E}$ are required. Consequently, τ_0, Γ_i and Ω must be known. (ii) The use of unloading and reloading to evaluate the constituent properties has the convenience that the hysteresis is dependent only on τ_0. Consequently, precise determination of τ_0 is possible. Moreover, with τ_0 known from the hysteresis, both Γ_i and Ω can be evaluated from the permanent strain. The principal SDE results are as follows.

The permanent strain is [4, 8, 17]

$$(\varepsilon_0 - \varepsilon^*)\mathscr{H}^{-1} = 4(1 - \Sigma_i)\Sigma_T + 1 - 2\Sigma_i^2 \qquad (49)$$

where $\mathscr{H}$ is a hysteresis index (Table III)

$$\mathscr{H} = b_2(1 - a_1 f)^2 R\bar{\sigma}^2 / 4\bar{d}\tau_0 E_m f^2 \qquad (50)$$

and

$$\Sigma_T = \sigma^T/\bar{\sigma} \qquad (51)$$

The hysteresis loop is parabolic and has a maximum width at half maximum, $\delta\varepsilon_{1/2}$ (Figs 9, 26) given by

$$\delta\varepsilon_{1/2} = \mathscr{H}/2 \qquad (52)$$

The unloading strain is (Fig. 26)

$$\Delta\varepsilon_p = \mathscr{H} \qquad (53)$$

and the unloading modulus is

$$(\bar{E})^{-1} = (E^*)^{-1} + \mathscr{H}/\bar{\sigma} \qquad (54)$$

5.4.1.2. Large debond energy. For LDE (Fig. 23), when $\sigma < \bar{\sigma}_s$, the unloading modulus depends on both τ_0 and Γ_i (Fig. 26). There are also linear segments to the unloading and reloading curves. These segments can be used to establish constructions that allow the constituent properties to be conveniently established. The principal results are as follows. The permanent strain is [17]

$$(\varepsilon_0 - \varepsilon^*)\mathscr{H}^{-1} = 2(1 - \Sigma_i)(1 - \Sigma_i + 2\Sigma_T) \qquad (55)$$

and the unloading modulus is

$$(\bar{E})^{-1} = (E^*)^{-1} + 4\Sigma_i(1 - \Sigma_i)\mathscr{H}/\bar{\sigma} \qquad (56)$$

In this case, the hysteresis loop has parabolic and linear segments. The loop width depends on the magnitude of Σ_i. For intermediate values, $\frac{1}{2} \leqslant \Sigma_i \leqslant \frac{3}{4}$

$$\delta\varepsilon_{1/2} = \mathscr{H}[\tfrac{1}{2} - (1 - 2\Sigma_i)^2] \qquad (57)$$

whereas for $\frac{3}{4} \leqslant \Sigma_i \leqslant 1$

$$\delta\varepsilon_{1/2} = 4\mathscr{H}[1 - \Sigma_i]^2 \qquad (58)$$

5.4.2. Stresses above saturation

At stress, $\sigma > \bar{\sigma}_s$, the crack density remains essentially constant and there is no additional stress transfer between the fibres and the matrix. In this case, the tangent modulus has been assumed to be given by [13]

$$\begin{aligned} E_t &\equiv \mathrm{d}\bar{\sigma}/\mathrm{d}\bar{\varepsilon} \\ &= f E_f \qquad (59) \end{aligned}$$

In practice, the tangent modulus is usually found to be smaller than predicted by Equation 59. Two factors are involved: changes in the sliding stress and fibre failure. At high fibre stresses, the Poisson contraction of the fibres reduces the radial stress, σ_{rr}. Consequently, whenever the sliding stress can be represented by Equation 1, τ decreases as the stress increases. The associated tangent modulus at fixed crack spacing is [33]

$$\mathrm{d}\bar{\sigma}/\mathrm{d}\bar{\varepsilon} = b_1 E_m \bar{d}/a_3 b_2 R[1 + \vartheta + \exp(-\vartheta)] \qquad (60)$$

where $\vartheta = 2\mu b_1 d/R$, with μ being the friction coefficient.

As the UTS is approached, significant fibre failures occur, which further reduce the tangent modulus. The basic stress–strain relationship is [66]

$$\bar{\sigma} = fE_f\bar{\varepsilon}\left\{1 + \sum_{n\geqslant 1}\frac{(-1)^n}{2n!}\left[\frac{2 + n(m+1)}{1 + n(m+1)}\right] \times (E_f\bar{\varepsilon}/S_c)^{n(m+1)}\right\} \quad (61)$$

The hysteresis behaviour also changes once saturation has been achieved, although initial unloading is still parabolic, but then becomes linear. The loop width eventually reaches

$$\delta\varepsilon_{1/2} = 2\tau_0\bar{d}_s/E_f R \quad (62)$$

5.5. Simulations

The preceding constitutive laws may be used to simulate stress–strain curves for comparison with experiments. In order to conduct the simulations, the constituent properties, τ, Γ_i and Ω are first assembled into the non-dimensional parameters $\mathscr{H}$, Σ_i, and Σ_T. For this purpose, it is necessary to have independent knowledge of $\bar{d}(\bar{\sigma})$. When this does not exist, an estimation procedure is needed, based on Equation 45, through evaluation of $\bar{d}_s$, $\bar{\sigma}_{mc}$ and $\bar{\sigma}_s$. The first step is to use Equation 42 to evaluate the saturation crack spacing $\bar{d}_s$ from the constituent properties. One limitation of this procedure concerns the accuracy with which χ and Γ_m are known. An alternative option exists when crack spacing data are available for another CMC with the same matrix. Then, Equation 42 can be used to scale $\bar{d}_s$ in accordance with

$$\bar{d}_s^3 \sim E_f R^2/\tau_0^2 E_L \quad (63)$$

It is also possible to estimate $\bar{\sigma}_{mc}$ from the constituent properties, by using Equation 39. Then Equation 48 is used to estimate $\bar{\sigma}_s$.

When $\bar{d}(\bar{\sigma})$ has been established in this manner, stress–strain curves can be simulated for one-dimensional materials. Internal consistency recognizes that both $\bar{d}_s$ and $\bar{\sigma}_{mc}$ depend on τ_0 and Γ_i. In addition, $\bar{\sigma}_{mc}$ depends on the misfit stress σ^T. However, $\bar{d}_s$ is σ^T independent. Based on this approach, simulations have been used to conduct sensitivity studies of the effects of constituent properties on the inelastic strain. Examples (Fig. 27) indicate the spectrum of possibilities for CMCs.

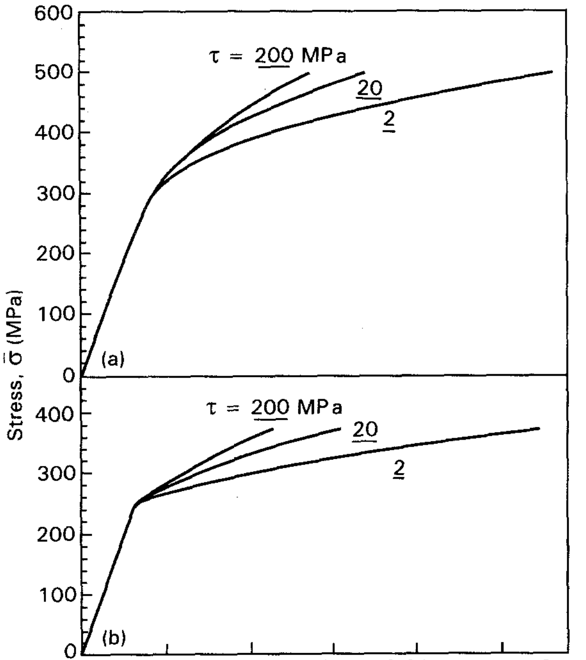

Figure 27 Simulated stress–strain curves for one-dimensional CMCs indicating the relative importance of constituent properties. (a) LDE, $\Gamma_i = 2\,\mathrm{J\,m^{-2}}$, $\sigma_s/\sigma_{mc} = 2$; (b) SDE, $\Gamma_i = 0$, $\sigma_s/\sigma_{mc} = 1.5$.

5.6. Experiments

Matrix cracking and inelastic strain measurements have been made on two unidirectional CMCs [4, 48]: SiC/CAS, as well as SiC/SiC (produced by CVI). The stress–strain curves for these two materials (Fig. 28) indicate a contrast in inelastic strain capability. Some typical hysteresis measurements for these materials (Fig. 28) reveal major differences which must reflect differences in constituent properties. There are also considerable differences in the evolution of matrix cracks. An analysis of the hysteresis loops (Fig. 29) and the permanent strain (Fig. 30), as well as other characteristics, indicate the substantial differences in interface properties summarized in Table V. These differences arise despite the fact that the fibres are the same and that the fibre coatings are carbon in both cases. (Analysis of the coating structure by TEM provides a rationale for specifying the differing interface responses in accordance with the basic model (Fig. 9).)

The constituent properties from Table V can, in turn, be used to simulate the stress–strain curves

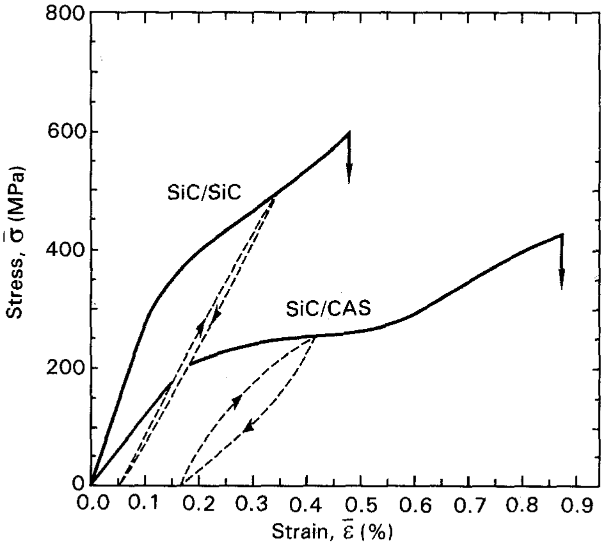

Figure 28 Stress–strain curves and typical hysteresis measurements obtained on SiC/CAS and SiC/SiC unidirectional composites.

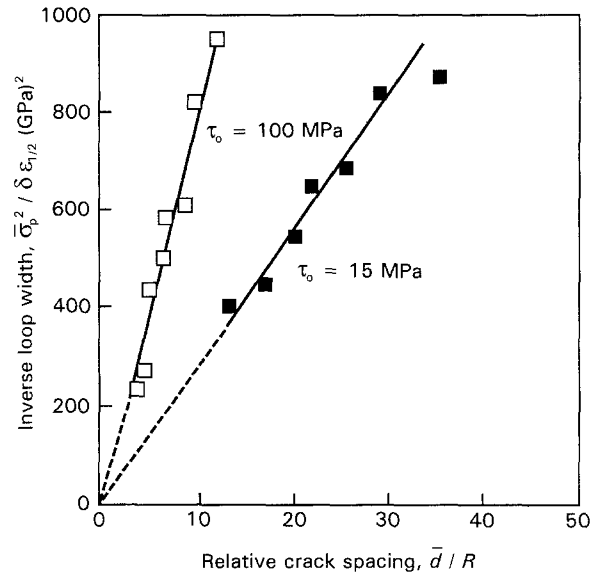

Figure 29 Analysis of hysteresis loop results for unidirectional (■) SiC/CAS and (□) SiC/SiC.

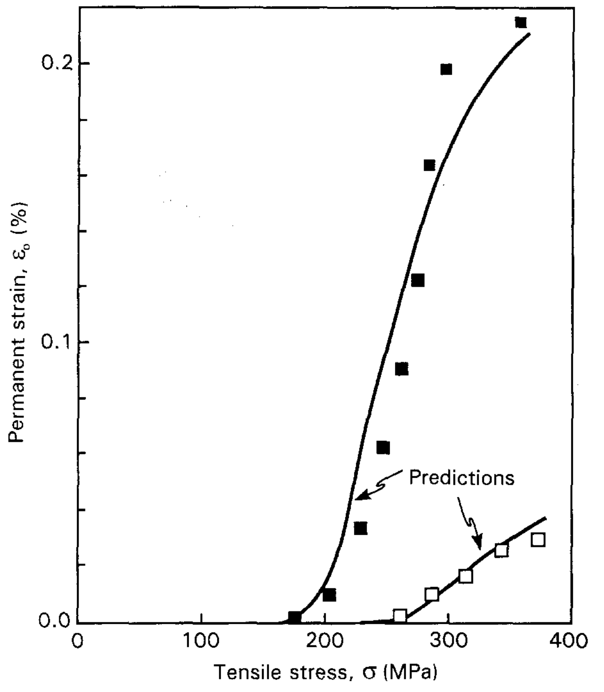

Figure 30 Analysis of permanent strains for unidirectional (■) SiC/CAS and (□) SiC/SiC.

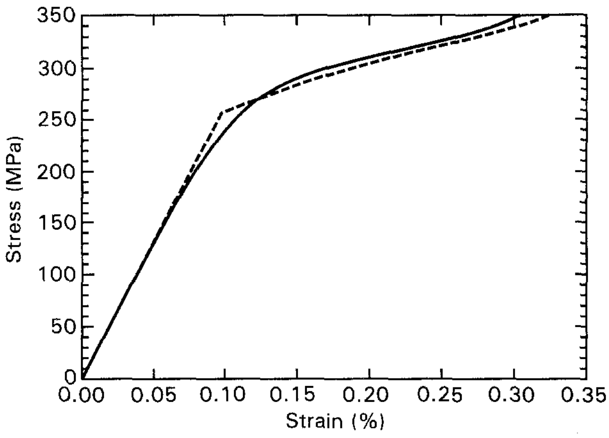

Figure 31 (---) Simulated stress–strain curve for unidirectional SiC/SiC and (——) comparison with experiment.

(Fig. 31). The agreement with measurements affirms the simulation capability, whenever the constituent properties have been obtained from completely independent tests (Table II). This has been done for the SiC/CAS material, but not yet for SiC/SiC. While the limited comparison between simulation and experiment is encouraging, an unresolved problem concerns the predictability of the saturation stress, $\bar{\sigma}_s$. A related issue concerns the necessity for matrix crack density information. Again, additional insight is needed to establish meaningful bounds. Meanwhile, experimental methods that provide crack density information in an efficient, straightforward manner require development. One possibility involves measurements of the acoustic velocity, v_a, which can be conducted continuously, during testing [81]. These measurement relate to changes in the elastic modulus E^* as matrix cracks develop ($E^* = \rho_0 v_a^2$). This modulus can be related to the crack spacing, through a model (Equation 46).

There has been debate about the matrix cracking stress, $\bar{\sigma}_{mc}$, and its interpretation upon comparison with experimental measurements. When adequate independent measurements of constituent properties have been measured (Fig. 32), it has been found [61] that the stress at which significant inelastic strain occurs always exceeds $\bar{\sigma}_{mc}$, given by Equation 39. This stress may thus be interpreted as the stress at which matrix cracking is sufficiently extensive to cause detectable inelastic strain. It thus has a similar interpretation to the yield strength (or proof stress) in metallic systems. It may be used as a basic strength parameter relevant to the simulation of stress–strain curves, as well as calculations of stress redistribution. However, small matrix cracks form at stresses below $\bar{\sigma}_{mc}$ [6]. These arise in heterogeneous regions of the composite, where interactions occur between small matrix flaws and the stress field. Such flaws are most

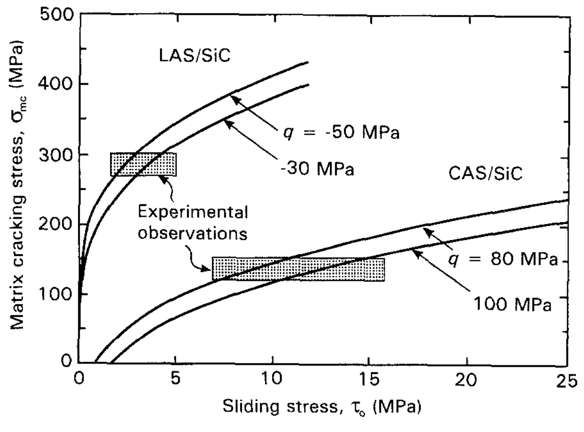

Figure 32 A comparison between measured and predicted values of the matrix cracking stress for two unidirectional CMCs.

important when atmospheric degradation of the fibres is possible, because they provide pathways for ingress of the degrading species. Again, analogies with yielding in metals may be useful. Notably, slip over small distances (within grains) occurs in metals at stresses appreciably below the macroscopic yield strength. Such slip is important in fatigue, etc., but is incidental to the plastic strain that causes stress redistribution.

6. Matrix cracking in two-dimensional materials

General loadings of two-dimensional CMCs involve mixtures of tension and shear. For design purposes, it is necessary to have models and experiments that combine these loadings. Matrix cracking and fibre failure are the basic phenomena that dictate all of the non-linearities. However, there are important differences between tension and shear. The behaviour subject to tensile loading has been widely investigated [45, 53, 87–92]. The behaviour in shear is only appreciated at an elementary level [25]. Furthermore, the intermediate behaviour has had even less study [88, 93]. Nevertheless, the basic concept is clear. It is required that matrix cracking, as well as fibre failure, phenomena be incorporated into the models in a consistent manner, such that interpolation approaches can be devised and implemented, which interrelate the tensile and shear properties.

6.1. Tensile properties

General comparison between the tensile stress–strain [$\sigma(\varepsilon)$], curves for one- two-dimensional materials (Fig. 33) provides important perspective. It is found that $\sigma(\varepsilon)$ for two-dimensional materials is quite closely matched by simply scaling down the one-dimensional curves by 1/2. The behaviour of two-dimensional materials must, therefore, be dominated by the 0° plies, because these plies provide a fibre volume fraction in the loading direction about half that present in one-dimensional material [4]. (Furthermore, because some of the two-dimensional materials are woven, the 1/2 scaling infers that the curvatures introduced by weaving have minimal effect on the stress–strain behaviour.)

The most significant two-dimensional effects occur at the initial deviation from linearity. At this stage, matrix cracks that form either in matrix-rich regions or in 90° plies evolve at lower stresses than cracks in one-dimensional materials. The associated non-linearities are usually slight and do not normally contribute substantially to the overall non-linear response of the material. However, these cracks have important implications for oxidation embrittlement and creep rupture and require analysis. Matrix cracking in the 90° plies often proceeds by a tunnelling mechanism (Fig. 34). Tunnel cracking occurs subject to a lower bound stress σ_τ [94, 95], given by

$$\sigma_\tau = \sigma_\tau^0 - \sigma^{\mathrm{R}}(E_{\mathrm{L}} + E_{\mathrm{T}})/2E_{\mathrm{T}} \tag{64}$$

with

$$\sigma_\tau^0 = (E\Gamma_{\mathrm{R}}/t_{\mathrm{P}})^{1/2} g(f, E_{\mathrm{f}}/E_{\mathrm{m}}) \tag{65}$$

where

$$E_0 = E_{\mathrm{L}}(1 + E_{\mathrm{L}}/E_{\mathrm{T}})/2[E_{\mathrm{L}}/E_{\mathrm{T}} - \nu_{\mathrm{L}}^2] \tag{66}$$

The function g depends quite strongly on whether the transverse fibres either remain in contact with matrix upon loading or separate, as plotted on Fig. 35. As loading continues up to stresses that exceed σ_τ, additional cracks form in the 90° plies (thickness, t_{p}). These cracks have a spacing $\bar{L}$ that decreases as the stress increases. The consequence is a reduction in the modulus from E_0 to $\bar{E}$. The relative unloading modulus, $\bar{E}/E$, depends primarily on the crack density,

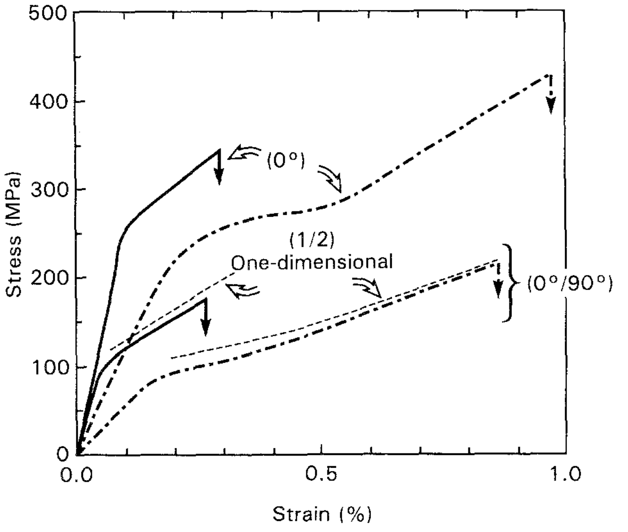

Figure 33 A comparison of stress–strain curves measured for one- and two-dimensional CMCs. The dotted lines labelled 1/2 (one-dimensional) represent the behaviour expected in two-dimensional materials when the 90° plies carry zero load. (– – –) SiC/CAS, (——) SiC/SiC (CVI).

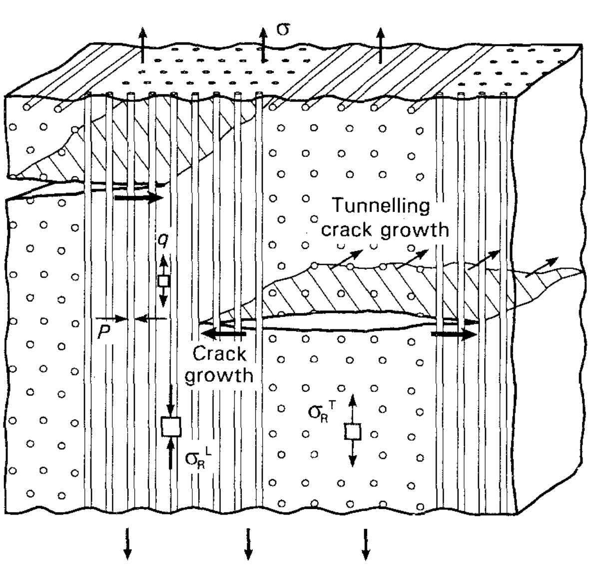

Figure 34 The matrix crack growth mechanisms that operate in two-dimensional CMCs.

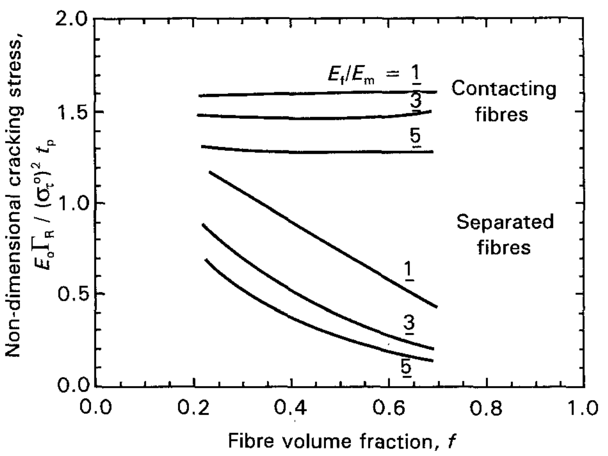

Figure 35 The effect of elastic modulus ratio and fibre volume fraction on the lower bound stress for tunnel cracking ($\sigma^R = 0$) for contacting and separating interfaces.

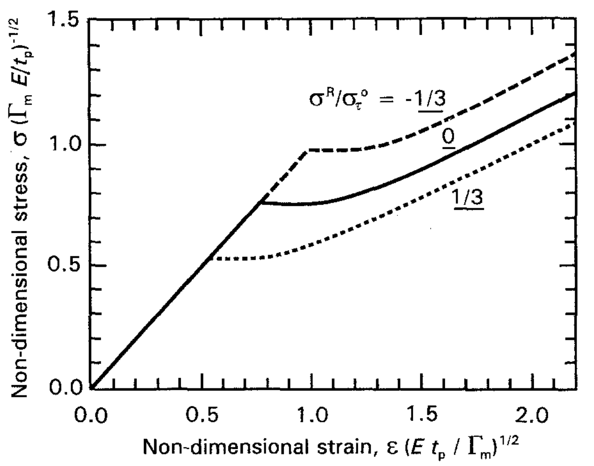

Figure 37 Simulated stress/strain response for a two-dimensional CMC subject to tunnel cracking.

$t_p/\bar{L}$, in the 90° plies [95, 96]. The effect when the fibres are contacting is illustrated on Fig. 36. The ratio $\bar{E}/E_0$ is larger when the fibres separate. Note that, at large crack densities, a limiting value of $\bar{E}$ designated E_ℓ, is reached, given by

$$\bar{E}_\ell/E_0 \;=\; E_L/(E_L + E_T) \qquad (67)$$

The corresponding permanent strain is

$$\varepsilon_0 \;=\; (1/\bar{E} - 1/E_0)\sigma^R(E_L + E_T)/2E_L \qquad (68)$$

Examples of the overall stress–strain response are summarized in Fig. 37 [95]. These curves were obtained by first establishing the change in crack spacing, $\bar{L}$, with stress and then adding the elastic strain (based on $\bar{E}$, Fig. 36) to the permanent strain (Equation 68) to obtain the total strain. In practice, the stresses at which these cracks evolve may be larger, because the formation of cracks, at stresses above σ_τ, depends on the availability of flaws in the 90° plies.

Lateral extension of these tunnel cracks into the matrix of the 0° plies (Fig. 34) results in behaviour similar to that found in one-dimensional material. Moreover, if the stress σ^0 acting on the 0° plies is known, the one-dimensional solutions may be used directly to predict the plastic strain. Otherwise, this stress must be estimated [95]. For a typical 0/90 system, σ^0 must range between $\bar{\sigma}$ and $2\bar{\sigma}$, depending upon the extent of matrix cracking in the 90° plies and upon E_T/E_L. Preliminary analysis has been conducted using, $\sigma^0 = 2\bar{\sigma}$, as implied by the comparison between one- and two-dimensional stress–strain curves (Fig. 33). Additional modelling on this topic is in progress.

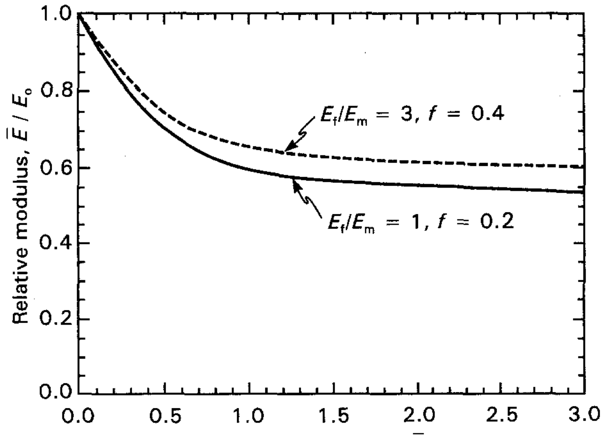

Figure 36 The change in unloading compliance caused by cracks in the 90° plies.

Using this simplified approach, simulations of stress–strain curves have been conducted [97, 98]. These curves have been compared with experimental measurements for several two-dimensional CMCs. The simulations lead to somewhat larger flow strengths than the experiments, especially at small inelastic strains. To address this discrepancy, further modelling is in progress, which attempts to couple the behaviour of the tunnel cracks with the matrix cracks in the 0° plies.

6.2. Shear properties

The matrix cracking that occurs in two-dimensional CMCs, subject to shear loading depends on the loading orientation and the properties of the matrix. Two dominant loading orientations are of interest: in-plane shear along one fibre orientation and out-of-plane (or interlaminar) shear. The key difference between these loading orientations concerns the potential for interaction between the matrix cracks and the fibres (Fig. 38). For inplane loading, the matrix crack must interact with the fibres (Fig. 38a). Conversely, for the out-of-plane case, matrix cracks evolve without significant fibre interaction (Fig. 38b). Such interactions impede matrix crack development. Consequently, the in-plane shear strength always exceeds the interlaminar shear strength.

6.2.1. *In-plane shear*

Experiments that probe the in-plane shear properties have been performed by using Iosipescu test specimens [25]. A summary of experimental results (Fig. 6)

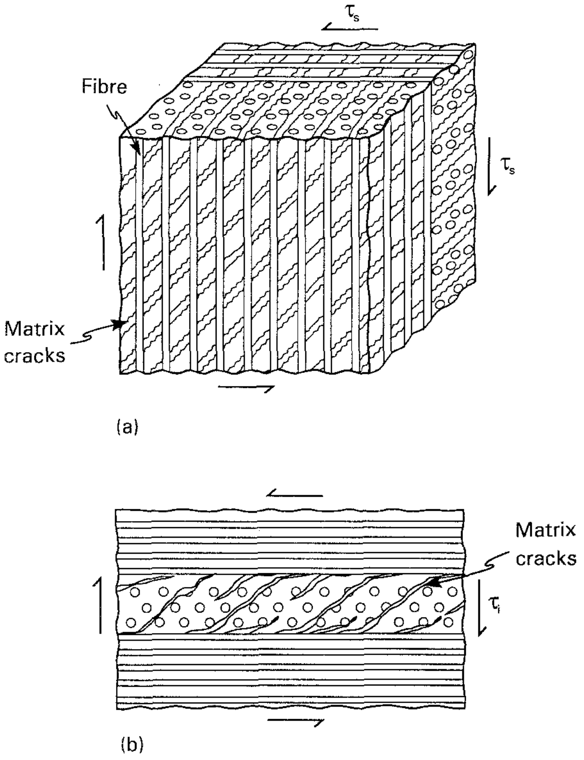

Figure 38 Schematic illustration of the two modes of shear damage: (a) in-plane (b) interlaminar.

indicates that the matrix has a major influence on the shear flow strength, τ_s, and the shear ductility, γ_c. Moreover, it has been found that the shear flow strengths can be ranked using a parameter, $\mathscr{W}$, derived from the matrix cracking stress in the absence of interface sliding [57], given by

$$\mathscr{W} = (\Gamma_m/RG)^{1/2} \tag{69}$$

The results from Fig. 6, ranked in this manner, are plotted on Fig. 39. The property of principal importance within $\mathscr{W}$ is the shear modulus, G, which reflects the increase in compliance caused by the matrix cracks. However, it remains to develop a model that gives a complete relationship between the composite strength and the constituent properties.

The shear ductility also appears to be influenced by the shear modulus, but in the opposite sense: high modulus matrices result in low ductility. This behaviour has been rationalized in terms of the effect of matrix modulus on the bending deformation experienced by fibres between matrix cracks [25]. As yet, there have been no calculations that address this phenomenon.

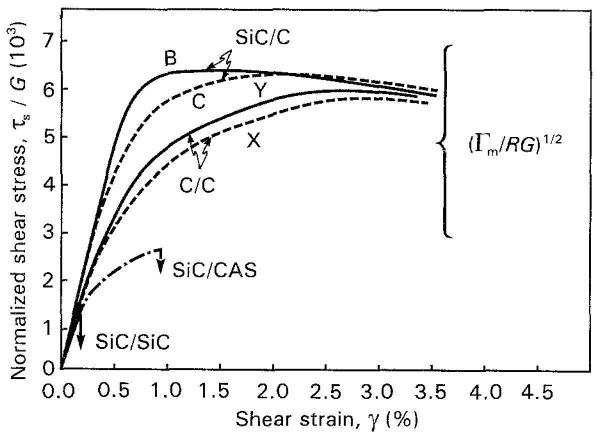

Figure 39 Normalized in-plane shear stress–strain curves with the non-dimensional parameter $\mathscr{W}$ indicated.

6.2.2. Interlaminar shear

The matrix cracks that form upon interlaminar shear loading and provide the plastic strains are material dependent. The simplest case (Fig. 38b) involves multiple tunnel cracks that extend across the layer and orient normal to the maximum tensile stress within the layer [93]. In other cases, the matrix cracks are confined primarily to the matrix-only layers between plies [60]. A general understanding of these different types of behaviour does not yet exist.

When the interlaminar cracks form by tunnelling, the solutions have a direct analogy within the transverse cracking results described above [39]. In shear loading, the tunnel cracks evolve and orient such that a mode II crack develops, as sketched in Fig. 40. The evolution of the echelon array of cracks has been analysed and shown to occur in accordance with the stress–displacement curve plotted on Fig. 41 [39].

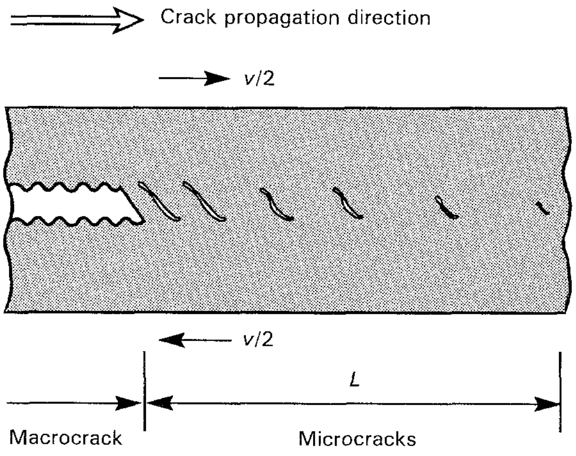

Figure 40 A schematic illustration of echelon cracks that evolve into a mode II failure.

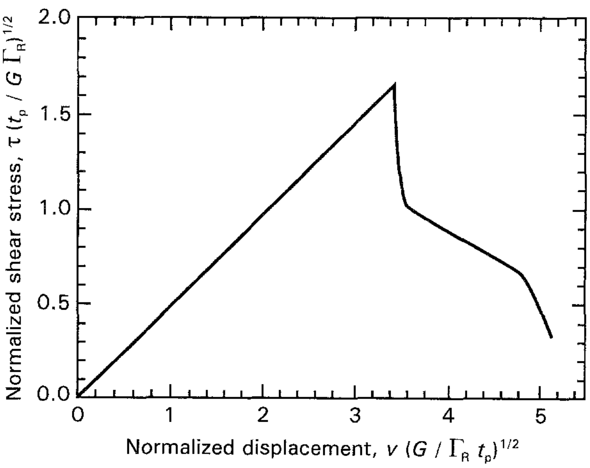

Figure 41 The stress–displacement relation for interlaminar shear.

There is a critical shear stress, τ_c, at which interlaminar shear failure occurs, given by

$$\tau_c \approx 1.5(G\Gamma_R/t_P)^{1/2} \qquad (70)$$

where t_P is now the thickness of the material layer that governs cracking. There must also be effects of residual stress, but these have yet to be included in the model. The form of the critical shear stress relation (Equation 70) is the same as that for transverse tunnel cracking (Equation 64), verifying that these two phenomena are interrelated. The elastic properties dictate whether τ_c or σ_τ is the larger: usually $\tau_c < \sigma_\tau$ because $G \ll E$.

6.3. Transverse tensile properties

CMCs with two-dimensional fibre architecture are susceptible to interlaminar cracking in various component configurations (Fig. 42). In such cases, as the crack extends through the component, conditions range from mode I to mode II. Tests and analyses are needed that relate to these issues. Most experience has been gained from PMCs [99]. The major issue is the manner whereby the interlaminar (transverse) cracks interact with the fibres. In principle, it is possible to conduct tests in which the cracks do not interact. In practice, such interactions always occur in CMCs, as the crack front meanders and crosses over inclined fibres [100, 101]. These interactions dominate the measured fracture loads in conventional cantilever (DCB) specimens, as well as in flexure specimens [102, 103]. Some typical results for the transverse fracture energy (Fig. 43), indicate the large values (compared with $\Gamma_m \approx 20\,\mathrm{J\,m^{-2}}$) induced by these interactions.

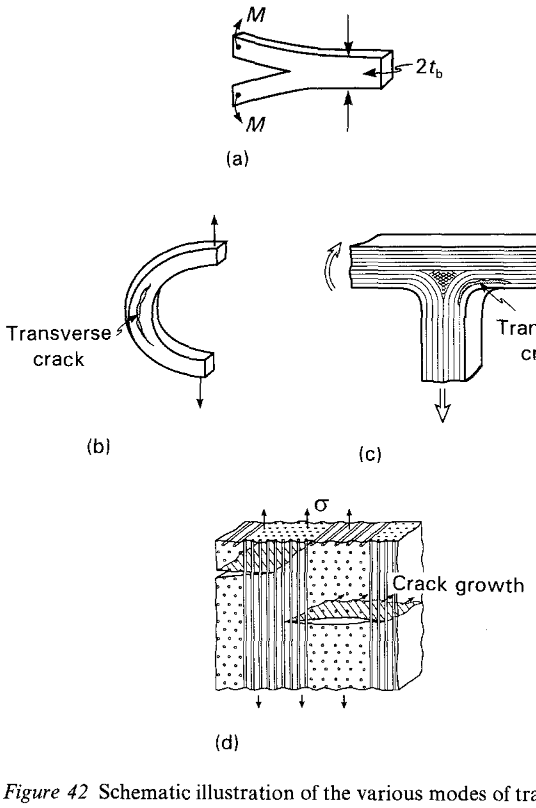

Figure 42 Schematic illustration of the various modes of transverse cracking in CMCs. (a) Cantilever beam, (b) C-specimen, (c) T-junction, (d) tunnel cracks.

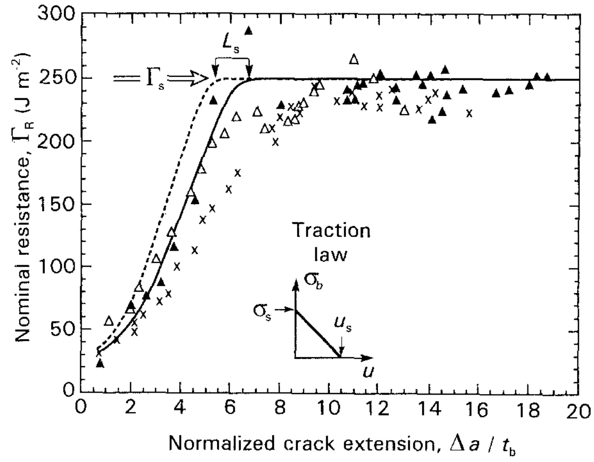

Figure 43 The transverse fracture resistance of a SiC/CAS material. h^*/h_0: (▲) 1.0, (△) 1.6, (×) 2.0. Also shown are the traction law assumed for inclined bridging fibres upon transverse cracking, and the predicted resistance curves for h^*/h_0 = (– – –) 1, (– – –) 2.

Analysis indicates that large-scale bridging (LSB) is involved and the bridging behaviour can be explicitly ascertained from the measured curves [102]. For the particular case of a DCB specimen (Fig. 42a), the J integral is explicitly defined in terms of the bending moment, M, and the traction law [12]. For example, the steady-state resistance, Γ_s, for a linear softening traction law, is

$$\begin{aligned}\Gamma_s &= 12M_s^2/E_L t_b^3 \\ &= \sigma_s u_s/2 + \Gamma_m \qquad (71)\end{aligned}$$

and the zone length at steady-state is

$$L_s = (Eu_s/3\sigma_s)^{1/4} t_b^{3/4} \qquad (72)$$

where $2t_b$ is the DCB beam thickness, M_s is the bending moment, with the quantities σ_s and L_s defined on Fig. 43. Experimental measurements made with DCB specimens can be used to evaluate the parameters, σ_s and u_s, by simply fitting the data to Equations 71 and 72. This information can then be used to predict Γ_s and Γ_R for other configurations.

An example is given for SiC/CAS composites (Fig. 43). Experimental results for this material [100] give $u_s \approx 100\,\mu\mathrm{m}$ and $\sigma_s \approx 10\,\mathrm{MPa}$. One application of these results is the prediction of the tunnel cracking found in 0/90 laminates (Equation 64). The analysis of tunnel cracking [95] has established that for typical laminate thicknesses, the crack opening displacements are small ($< 1\,\mu\mathrm{m}$). For such small displacements, there is a negligible influence of the fibres. Consequently, $\Gamma_R \approx \Gamma_m (1 - f)$. Other applications to C-specimens and T-junction are in progress.

An obvious limitations of the procedure is the uncertainty about the manner whereby the matrix crack interacts with the fibres in other geometries and hence, the universality of σ_s and u_s. This is a topic for further research.

7. Stress redistribution

7.1. Background

CMCs usually have substantially lower notch sensitivity than monolithic brittle materials and, in several cases, exhibit notch insensitive behaviour [2, 3]. This desirable characteristic of CMCs arises because the material may redistribute stresses around strain concentration sites. Notch effects appear to depend on the class of behaviour. Moreover, a different mechanics is required for each class, because the stress redistribution mechanisms operate over different physical scales. Class I behaviour involves stress redistribution by fibre bridging/pull-out, which occurs along the crack plane [12, 104, 105]. Large-scale bridging mechanics (LSBM) is preferred for such materials. Class II behaviour allows stress redistribution by large-scale matrix cracking [2] and continuum damage mechanics (CDM) is regarded as most appropriate. Class III behaviour involves material responses similar to those found in metals, and a comparable mechanics might be used [26, 27]: either LEFM for small-scale yielding or non-linear fracture mechanics for large-scale yielding. Because a unified mechanics has not yet been identified, it is necessary to use mechanism maps that distinguish the various classes (Figs 3 and 4).

7.2. Mechanism transitions

The transition between class I and class II behaviour involves considerations of both matrix crack growth and fibre failure. One hypothesis for the transition may be analysed using LSBM. Such analysis allows the condition for fibre failure at the end of an unbridged crack segment to be solved simultaneously with the energy release rate of the matrix front. The latter is equated to the matrix fracture energy [77]. By using this solution to specify that fibre failure occurs before the matrix crack extends into steady-state, class I behaviour is presumed to ensue. Conversely, class II behaviour is envisaged when steady-state matrix cracking occurs prior to fibre failure. The resulting mechanism map involves two indices (Table III)

$$\begin{aligned}\mathscr{S} &= (RS/a_0\tau)(E_m^2/E_L E_f)[(1-f)/f]^2 \\ &\equiv 3/\mathscr{A}_b \qquad (73)\end{aligned}$$

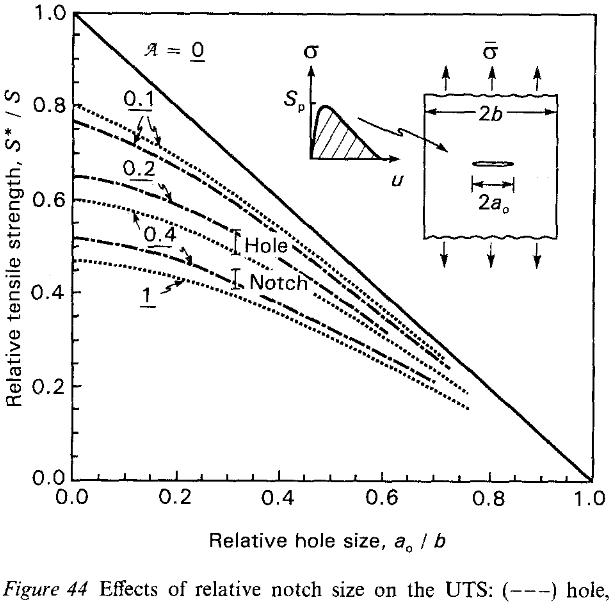

Figure 44 Effects of relative notch size on the UTS: (– – –) hole, (— - —) notch. Also shown are experimental data for a SiC/C material (vertical bars).

and

$$\mathscr{U} = \sigma_{mc}/S \qquad (74)$$

With $\mathscr{S}$ and $\mathscr{U}$ as coordinates, a mechanism map may be constructed that distinguishes class I and class II behaviour (Fig. 3). While this map has qualitative features consistent with experience, the experiments required for validation have not been completed. In practice, the mechanism transition in CMCs probably involves additional considerations.

The incidence of class III behaviour is found at relatively small magnitudes of the ratio of shear strength, τ_s, to tensile strength S. When τ_s/S is small, a shear band develops at the notch front and extends normal to the notch plane. Furthermore, because τ_s is related to G, the parameter G/S is selected as the ordinate of a mechanism map. Experimental results suggest that class III behaviour arises when $G/S \gtrsim 50$ (Fig. 4).

7.3. Mechanics methodology

7.3.1. *Class I materials*

The class I mechanism, when dominant, has features compatible with LSBM [104–106]. These mechanics may be used to characterize effects of notches, holes and manufacturing flaws on tensile properties, whenever a single matrix crack is prevalent. For cases wherein the flaw or notch is small compared with specimen dimensions, the tensile strength may be plotted as functions of both flaw indices: $\mathscr{A}_b$ and $\mathscr{A}_p$ (Fig. 18). For the former, the results are sensitive to the ratio of the pull-out strength, S_p, to the UTS [78]. These results should be used whenever the unnotched tensile properties are compatible with global load sharing. Conversely, $\mathscr{A}_p$ should be used as the notch index when the unnotched properties appear to be pull-out dominated.

When the notch and hole have dimensions that are a significant fraction of the plate width ($a_0/b > 0$), net section effects must be included [7, 8]. Some results (Fig. 44) illustrate the behaviour for different values of the notch sensitivity index, $\mathscr{A}$. Experimental validation has not been undertaken, although partial results for one material (SiC/C$_B$) are compatible with LSBM [27], as shown for data obtained with centre notches and holes (Fig. 44). The promising feature is that LSBM explains the difference between notches and holes (upon requiring that $\mathscr{A} \approx 0.4$).

7.3.2. *Class II materials*

The non-linear stress–strain behaviour governed by matrix cracking (expressed through $\bar{E}$, Equation 56 and ε_0, Equation 55) provides a basis for a damage mechanics (CDM) approach that may be used to predict the effects of notches and holes. Such developments are in progress. (An important factor that dictates whether continuum or discrete methods are used concerns the ratio of the matrix crack spacing to the radius of curvature of the notch.) In practice, several class II CMCs have been shown to exhibit notch insensitive behaviour, at notch sizes up to 5 mm

[2, 3]. The notch insensitivity is manifest in the effect of the relative notch size, a_0/b, on the ratio of the UTS measured in the presence of notches (designated S^*), to the strength in the absence of notches (designated S). Results for SiC/CAS are illustrated on Fig. 45. In this material, the non-linearity provided by the matrix cracks allows sufficient stress redistribution that the stress concentration is eliminated. This occurs despite the low ductility ($< 1\%$). A CDM procedure capable of predicting this behaviour will be available in the near future, using the stress–strain simulation capability based on constituent properties, (Figs 25, 35 and 36).

7.3.3. Class III materials

Class III behaviour has been found in several carbon matrix composites [26, 27]. In these materials, the shear bands can be imaged using an X-ray dye penetrant method. Based on such images, the extent of the shear deformation zone, ℓ_s, is found to be predictable from measured shear strengths, τ_s (Fig. 6), in approximate accordance with (Fig. 46)

$$\ell_s/a_0 \approx \sigma/\tau_s - 1 \tag{75}$$

This formula applies when $\ell_s/a_0 \gtrsim 2$. At smaller lengths, the relationship is parabolic. Calculations have indicated that this shear zone diminishes the stress ahead of the notch (Fig. 47), analogous to the effect of a plastic zone in metals. For C/C materials, it has been found that the shear band lengths are small enough that LEFM is able to characterize the experimental data over a range of notch lengths, such that, $K_{IC} \approx 16\,\mathrm{MPa\,m^{1/2}}$ (Fig. 48). However, conditions must exist where LEFM is violated. For example, when $\ell_s/a_0 \gtrsim 3$, the stress concentration is essentially eliminated (Fig. 47) and the material must then become notch insensitive. Further work is needed to identify parameters that bound the applicability of

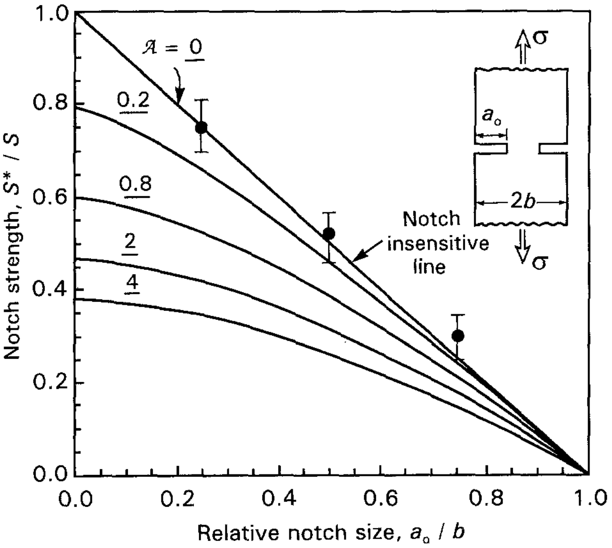

Figure 45 Experimental results (●) for SiC/CAS indicating notch insensitivity.

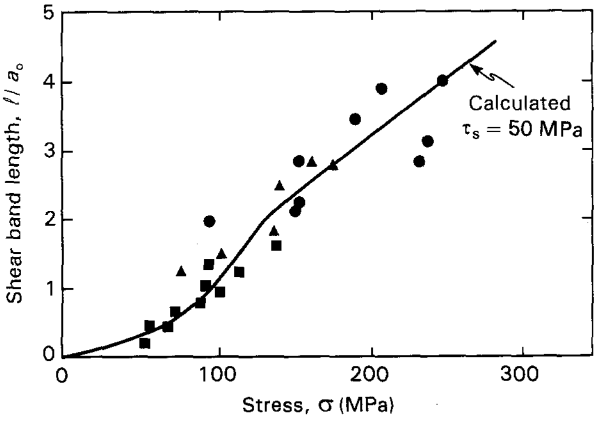

Figure 46 Relationship between shear band length and stress for a C/C composite. The calculated curve is also shown. Notch size (mm): (●) 1, (▲) 2, (■) 6.

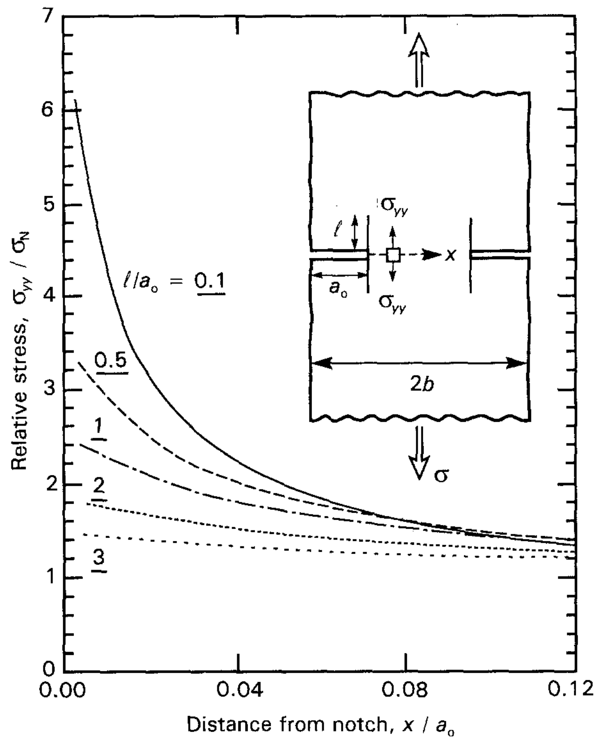

Figure 47 Effect of shear bands on the stress ahead of a notch.

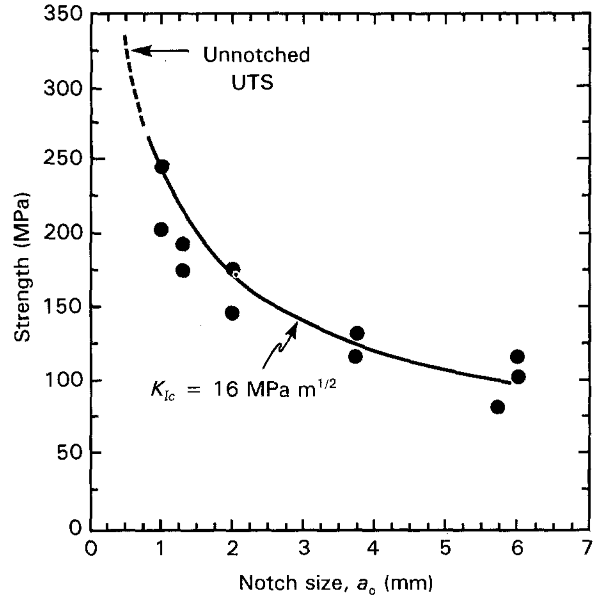

Figure 48 LEFM representation of notch data for C/C.

LEFM, as well as establish the requirements for notch insensitivity.

7.4. Measurements

Notch sensitivity data (Figs 44, 45 and 48) provide an explicit measure of stress redistribution. However, further understanding requires techniques that probe the stress and strain around notches, as CMCs are loaded to failure. Many of the methods have been developed and used for the same purpose on PMCs [107, 108]. These techniques can measure both strain and stress distributions.

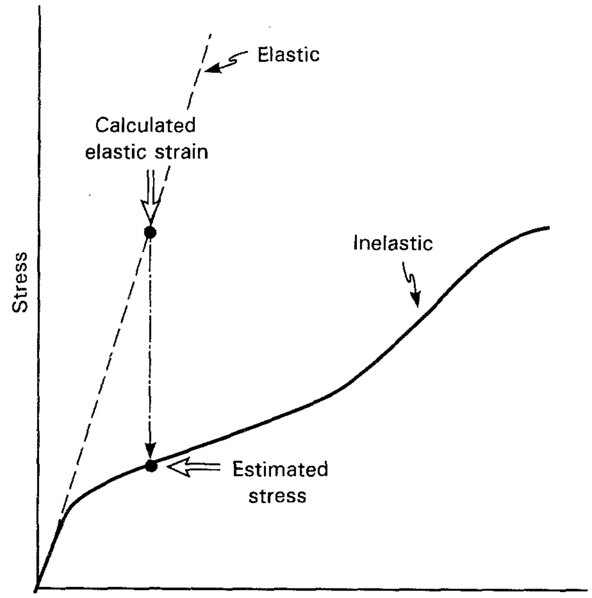

Figure 49 A schematic illustration of an approximate method for obtaining the stress by using the strain obtained from elastic calculations.

Strain distributions are measured with high spatial resolution by using Moiré interferometry. In this method, the fringe spacings relate to the in-plane displacements which, in turn, govern the strains. There has been only limited use of this technique for CMCs [109]. Preliminary measurements suggest that the inelastic deformations result in strains somewhat larger than elastic strains. That the reduced stress concentrations are thus approximated by the lower stresses that arise upon inelastic deformation at fixed strain (Fig. 49).

Because strain measurements appear to have minimal sensitivity to the stress redistribution mechanisms operative in CMCs, a technique that measures the stress distribution is preferred. One such method involves measurement of thermoelastic emission. This method relies on the rate of temperature rise, $\Delta\dot{T}$, that occurs when an element of the composite is subject to a hydrostatic stress rate, $\Delta\dot{\sigma}_{kk}$, under adiabatic conditions. The fundamental adiabatic relationship for a homogeneous solid is [110]

$$\Delta\dot{\sigma}_{kk} = (C_v\rho_0/\alpha T_0)\Delta\dot{T} \qquad (76)$$

where C_V is the specific heat at constant strain and ρ_0 is the density. One experimental implementation of this concept is a technique referred to a stress pattern analysis by thermoelastic emission (SPATE) [110]. It

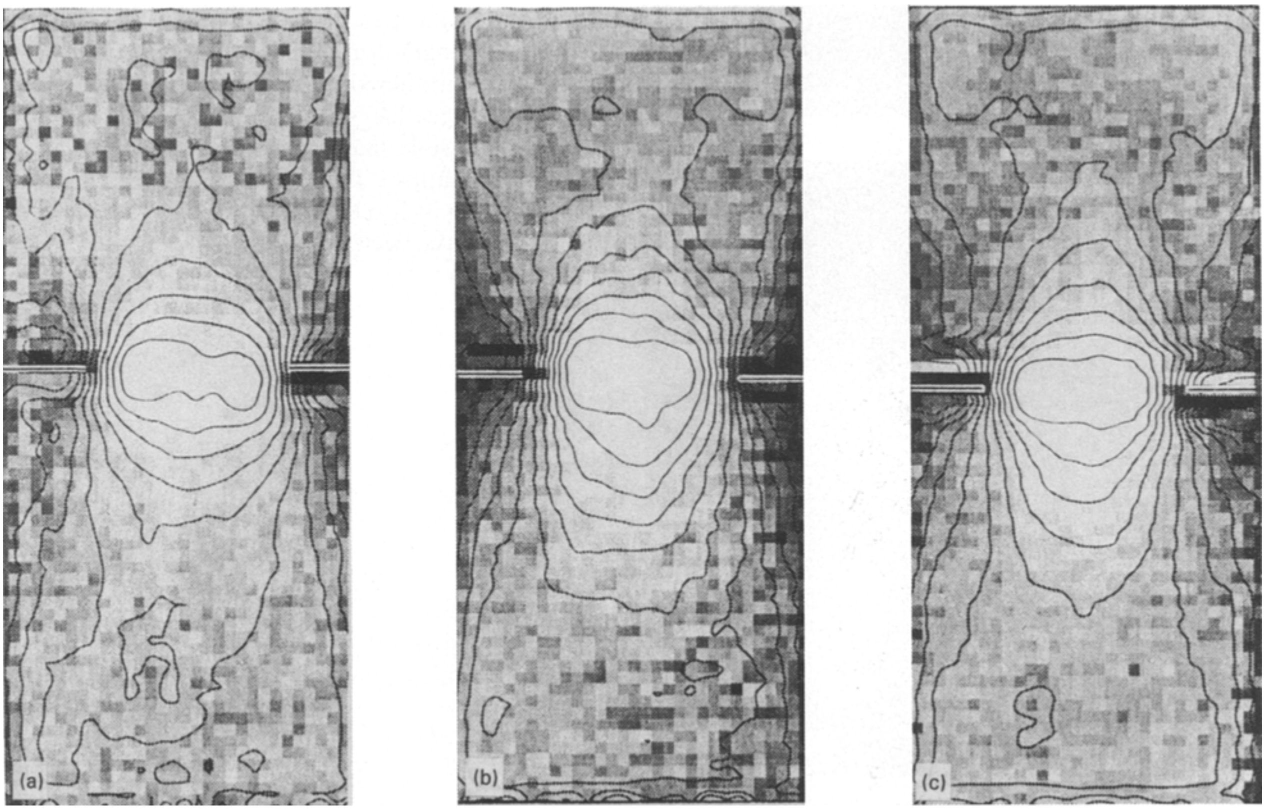

Figure 50 SPATE images obtained from a SiC/CAS composite after imposing three applied loads (a–c). The light regions along the notch plane are the zone at the highest stress. Note that this zone is not at the notch tip, but has displaced towards the centre. The load at (c) is 90% of the UTS.

involves the use of high sensitivity infrared detectors, which measure the temperature in a lock-in mode, as a cyclic stress is applied to the material. This feature essentially eliminates background problems and has good signal-to-noise characteristics. SPATE measurements are conventionally performed at small stress amplitudes, which elicit "elastic" behaviour in the material. Experimental results [111] for a class II material (SiC/CAS) have confirmed that the stress concentration can be eliminated by matrix cracks (Fig. 50). In addition, results for a class III material (C/C) have provided a direct measure of the stress redistribution caused by shear bands (Fig. 51).

Another method for strain measurement uses fluorescence spectroscopy [112]. This method has particular applicability to oxides, especially Al_2O_3 (either as fibre or matrix). The technique has the special advantage that strains can be measured in individual fibres, such that stress changes caused by matrix cracks can be measured. Such measurements permit the material to be probed at the spatial resolution needed to understand mechanisms in detail [63].

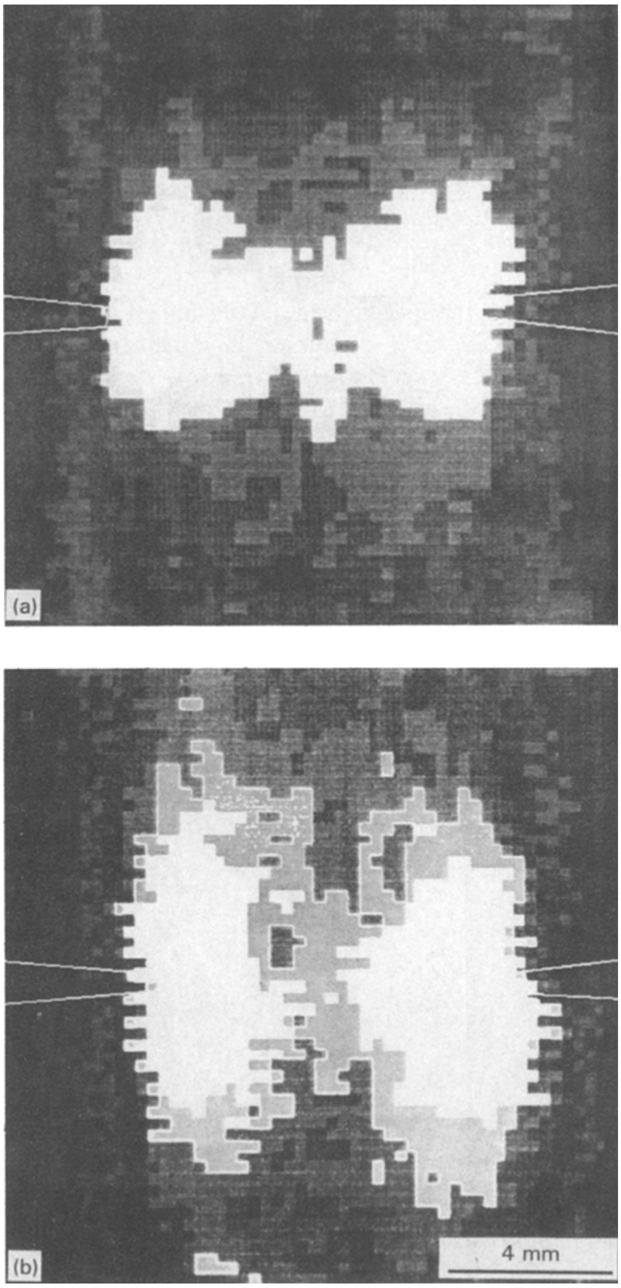

Figure 51 SPATE images obtained from a C/C composite at two load levels. In this case, the regions of highest stress are white. Note that the high stress zone spreads laterally as the load increases from (a) to (b).

8. Fatigue

8.1. Basic phenomena

Upon cycling loading, matrix cracking and fibre failure occur in brittle matrix composites [10, 54, 79, 113, 114], in accordance with the same three classes found for monotonic loading (Fig. 2). The preceding matrix cracking and fibre failure models still apply, except that some additional factors need to be introduced [114]. The experimental results needed to establish the specific fatigue mechanisms that operate in CMCs are sparse. However, similar mechanisms operate in metal (MMC) and polymer (PMC) matrix composites. Observations, modelling and measurements performed on these materials provide insights that facilitate and hasten an understanding of the cyclic behaviour of brittle matrix composites.

Among the new features that enter when cyclic loading is used are degradation mechanisms and, in some cases, revised crack growth criteria. The macroscopic characteristics associated with the degradation mechanisms are fatigue life (σ–N) curves (Fig. 52) and changes in compliance (Fig. 53). In addition, the hysteresis loops change as fatigue proceeds (Fig. 54). Analyses of compliance and hysteresis changes, as well as differences in fibre pull-out, indicate that the interface sliding stress changes upon fatigue. A cyclic sliding function, $\tau_f(N)$, thus becomes a new constituent property [114]. In some cases at high temperature and upon thermomechanical fatigue, a particularly low fatigue threshold stress (compared with the UTS) implies fibre strength degradation. Consequently, a cyclic fibre strength function, $S_f(N)$, may also be needed to predict fatigue life.

Several possible matrix crack growth criteria are applicable to fatigue. These relate to the conditions at the crack front. When the matrix itself is susceptible to cyclic fatigue, the Paris law relates crack growth in the

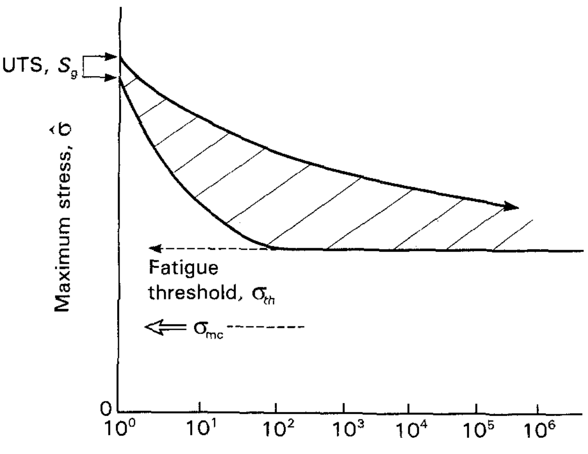

Figure 52 A schematic illustration of typical isothermal fatigue data for CMCs.

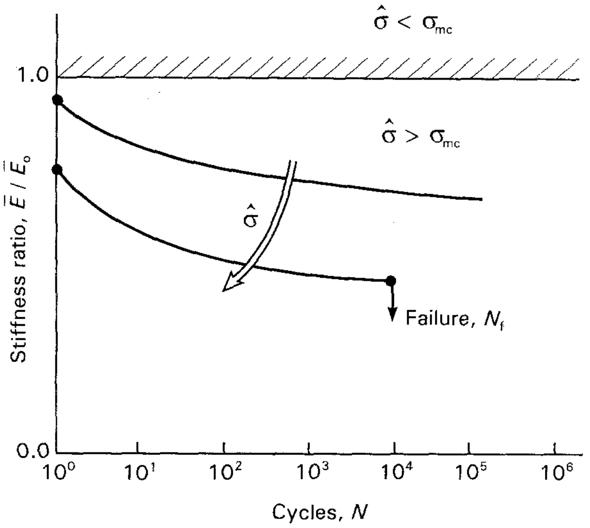

Figure 53 A schematic illustration of changes in modulus that occur in CMCs upon cycling.

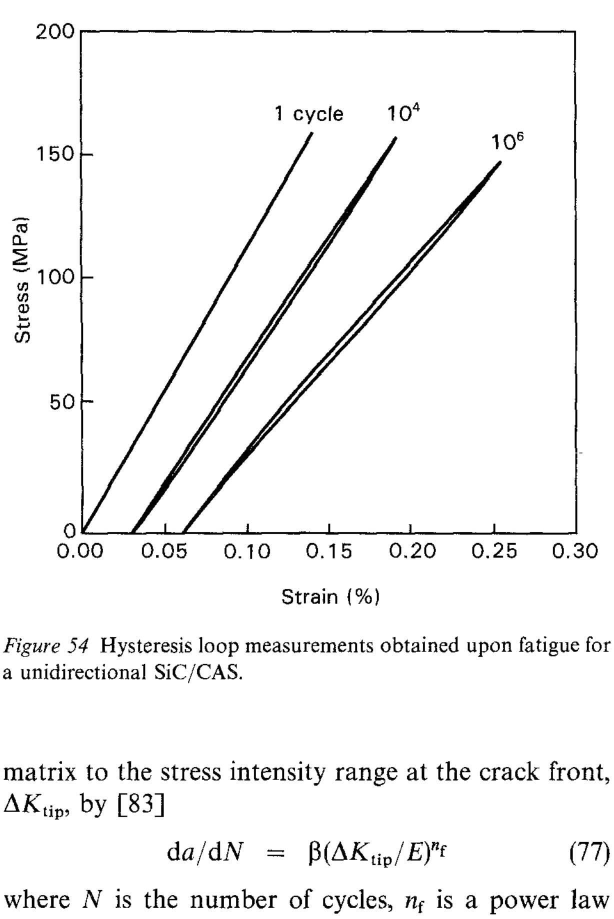

Figure 54 Hysteresis loop measurements obtained upon fatigue for a unidirectional SiC/CAS.

matrix to the stress intensity range at the crack front, ΔK_{tip}, by [83]

$$da/dN = \beta(\Delta K_{tip}/E)^{n_f} \tag{77}$$

where N is the number of cycles, n_f is a power law exponent and β is a material dependent coefficient. In some cases, n_f is sufficiently large that matrix crack growth is dominated by the peak value of either K_{tip} or $\mathscr{G}_{tip}$. Then, the same criterion used for monotonic loading (Equation 24) may be preferred. Finally, when the dominant mechanism involves stress corrosion, crack growth can be described in terms $\mathscr{G}_{tip}$ through the commonly-used power law [115]

$$\frac{da}{dt} = \mathring{a}_0\left(\frac{\mathscr{G}_{tip}}{\mathscr{G}_m}\right)^{\eta} \tag{78}$$

where $\mathring{a}_0$ is a reference velocity, η is the power law exponent and $\mathscr{G}_m$ is the matrix toughness, taken to be $\Gamma_m(1-f)$.

8.2. Matrix crack growth

When the interfaces are "weak", fibres can remain intact in the crack wake and cyclic frictional dissipation resists fatigue crack growth [83]. The latter has been extensively demonstrated on titanium matrix composites reinforced with SiC fibres [116–119]. The essential features of the "weak" interface behaviour are as follows: intact, sliding fibres acting in the crack wake shield the crack tip, such that the stress intensity range at the crack tip, ΔK_{tip}, is less than that expected for the applied loads, ΔK. Using this approach, a simple transformation converts the monotonic crack growth parameters into cyclic parameters that can be used to interpret and simulate fatigue growth of each matrix crack. The key transformation is based on the relationship between interface sliding during loading and unloading, which relates the monotonic result to the cyclic equivalent through [83]

$$(\tfrac{1}{2})\Delta\sigma_b(x/a, \Delta\sigma) = \sigma_b(x/a, \Delta\sigma/2) \tag{79}$$

where $\Delta\sigma$ is the range in the applied stress. Notably, the amplitude of the change in fibre traction, $\Delta\sigma_b$, caused by a change in applied stress, $\Delta\sigma$, is twice the fibre traction, σ_b, which would arise in the monotonic loading of a previously unopened crack, caused by an applied stress equal to half the stress change. This result is fundamental to all subsequent developments [83].

The stress intensity factor for bridging fibres subject to cyclic conditions is

$$\Delta K_b(\Delta\sigma) = -2\left(\frac{a}{\pi}\right)^{1/2}\int_0^a \frac{\Delta\sigma_b(x, \Delta\sigma)}{(a^2 - x^2)^{1/2}}\,dx \tag{80}$$

which, with the use of Equation 79 becomes

$$\Delta K_b(\Delta\sigma) = 2K_b^{max}(\Delta\sigma/2) \tag{81}$$

where the superscript "max" refers to the maximum values of the parameters achieved in the loading cycle and thus, K_b^{max} is the bridging contribution that would arise when the crack is loaded by an applied stress equal to $\Delta\sigma/2$. Furthermore, because ΔK is linear, Equation 79 is also valid for the tip stress intensity factor

$$\Delta K_{tip} = 2K_{tip}(\Delta\sigma/2) \tag{82}$$

When the fibres remain intact, a cyclic steady-state (ΔK independent of crack length) is obtained when the cracks are long, given by the condition $\Delta\mathscr{E} \leqslant 4$ [83], where $\Delta\mathscr{E}$ is defined in Table III. The result is (for cyclic loading, the residual stress, q, does not affect ΔK_{tip}.)

$$\Delta K_{tip} = \Delta\sigma R^{1/2}(12^{1/2}\Delta\mathscr{T})^{-1} \tag{83}$$

where $\Delta\mathscr{T}$ is defined in Table III.

The corresponding crack growth rate is determined by using a crack growth criterion. When a Paris law applies, Equations 77 and 83 give [83]

$$\frac{da}{dN} = \beta\left[\left(\frac{\Delta\sigma R^{1/2}}{6^{1/2}\Delta\mathscr{T}E_m}\right)\right]^{n_f} \tag{84}$$

When the matrix does not fatigue, such that Equation 24 represents the crack growth criterion, fatigue crack growth after the first cycle is only possible whenever τ reduces upon cycling, as elaborated below.

When short cracks are of relevance ($\Delta\mathscr{E} > 4$)

$$\Delta K_{\text{tip}} = \Delta\sigma(\pi a)^{1/2} \times\left[1 - \frac{4.31}{\Delta\mathscr{E}}(\Delta\mathscr{E} + 6.6)^{1/2} + \frac{11}{\Delta\mathscr{E}}\right] \qquad (85)$$

Consequently, at fixed $\Delta\sigma$, ΔK_{tip} increases as the crack extends, and the Paris law matrix crack growth accelerates. However, the bridged matrix fatigue crack always grows at as lower rate than an unbridged crack of the same length. Consequently, the composite always has superior crack growth resistance relative to the monolith.

To incorporate the effects of fibre breaking into the fatigue crack growth model, a fibre failure criterion based on S_g has been used [120]. To conduct the calculation, once the fibres begin to fail, the unbridged crack length is continuously adjusted to maintain a stress at the unbridged crack tip equal to the fibre strength. These conditions lead to the determination of the crack length, a_f, when the first fibres fail, as a function of the fibre strength and the maximum applied load (Fig. 55). Note that when either the fibre strength is high or the applied stress is low, no corresponding value of a_f can be identified and the fibres do not fail.

After the first fibre failure, fibres continue to break as the crack grows. Continuing fibre failure creates an unbridged segment larger than the original notch size. However, only the current unbridged length, $2a_u$, and the current total crack length, $2a$, are relevant [120] (Fig. 56).

If the fibres are relatively weak and break close to the crack tip ($a_0/a \to 1$), the bridging zone is always a small fraction of the crack length. In this case, there is minimal shielding. If the fibres are moderately strong, the fibres remain intact at first. But when the first fibres fail, subsequent failure occurs quite rapidly as the crack grows. The unbridged crack length then increases more rapidly than the total crack length and ΔK_{tip} also increases as the crack grows. When the fibres are even stronger, first fibre failure is delayed. But once such failure occurs, many fibres fail simultaneously and the unbridged length increases rapidly. This causes a sudden increase in the crack growth rate. Finally, when the fibre strength exceeds a critical value, they never break and the fatigue crack growth rate always diminishes as the crack grows. The sensitivity of these types of behaviour to fibre strength is quite marked (Fig. 56), with the different types of behaviour occurring over a narrow range of fibre strength. Some typical crack growth curves predicted using this approach are plotted in Fig. 57. This figure indicates the manner in which the crack extension, Δa, changes with the number of cycles, N, non-dimensionalized in accordance with Equation 81. Note that Δa accelerates at the onset of fibre failure.

The results of Fig. 55 can be used to develop a criterion for a "threshold" stress range, $\Delta\sigma_t$, below which fibre failure does not occur for any crack length. Within such a regime, the crack growth rate approaches the steady-state value given by Equation 84, with all fibres in the crack wake remaining intact. The variation in the "threshold" stress range with fibre strength is plotted on Fig. 58. The ordinate is essentially the peak stress normalized by the fibre strength, fS_c, whereas the abscissa is the notch length, a_0, normalized by terms contained in $\Delta\mathscr{E}$ (Table III). Note that, below

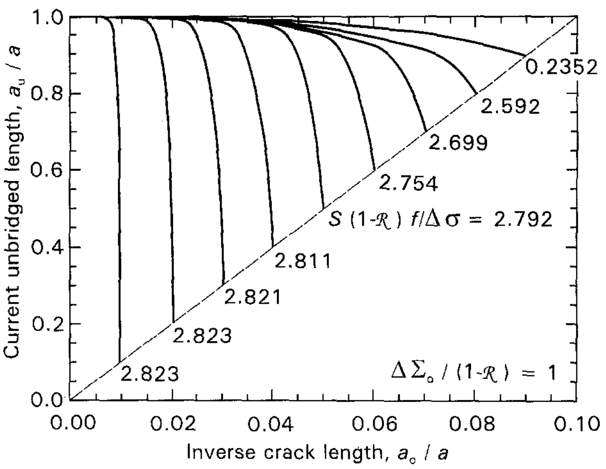

Figure 56 Fibre breaking rate as manifest in the current unbridged matrix crack length, $2a_u$, as a function of total crack length, $2a$. $n = 2$, $\Delta\mathscr{E}_0 = 4$.

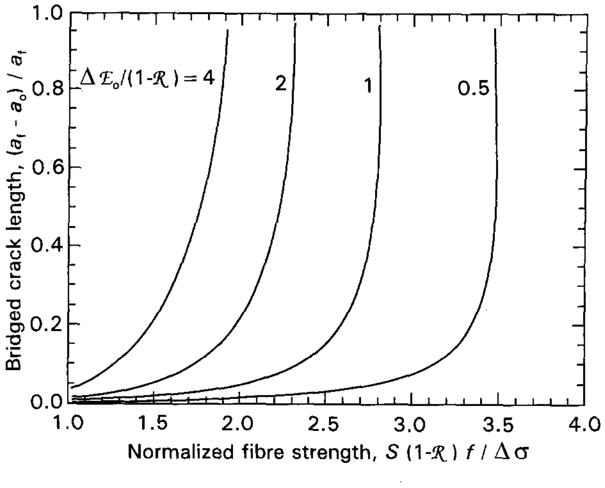

Figure 55 The length of matrix crack a_f at first fibre failure as a function of fibre strength for a range of stress amplitudes, $\Delta\mathscr{E}$.

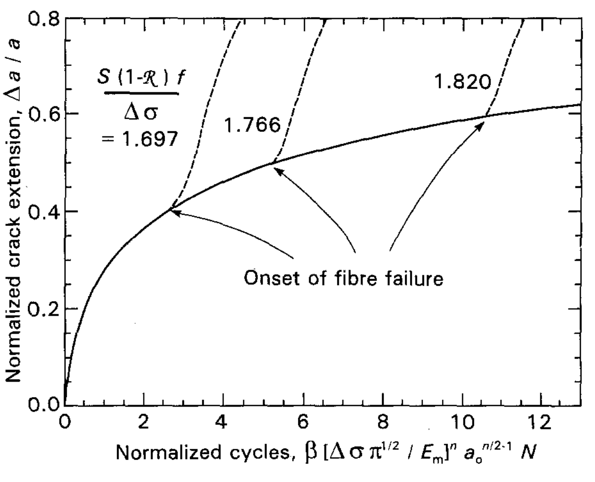

Figure 57 Predicted matrix crack growth curves.

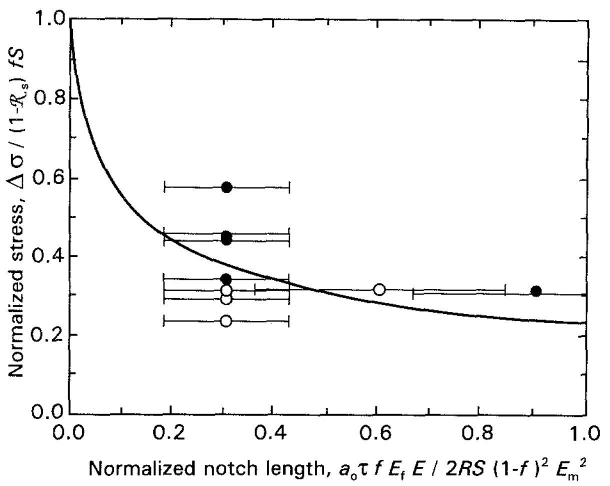

Figure 58 The threshold stress diagram. Also shown are experimental results for titanium matrix composites: (●) fibre failure, (○) no fibre failure; ($S = 4.0$ GPa, $\tau = 15$–35 MPa).

the line, composite failure does not occur, regardless of the number of fatigue cycles. Above the line, composite failure is inevitable.

A notable feature of the predictions pertains to the role of the stress ratio, $\mathcal{R}_s$, in composite behaviour. Prior to fibre failure, the crack growth rate is independent of $\mathcal{R}_s$ (except for its effect on the fatigue properties of the matrix itself). However, $\mathcal{R}_s$ has a strong influence on the transition to fibre failure, as manifest in its effect on the maximum stress. It thus plays a dominant role in the fatigue lifetime.

In most cases, CMCs are subject to multiple matrix cracking, which leads to reductions in the unloading modulus $\bar{E}$, as well as changes in the hysteresis. This aspect of fatigue is described below for matrices with large n_f.

8.3. Multiple cracking and failure

As cycling proceeds, the hysteresis measurements show that the interface sliding stress, τ_f, decreases. As this occurs, there is a corresponding decrease in both the matrix cracking stress, σ_{mc} (Equation 34) and the UTS (Equation 17a). The former effect leads to a permanent strain and a diminished modulus. The latter effect dictates the fatigue threshold stress, S_{th}, provided that fibre strength degradation does not occur. Both types of behaviour can be readily predicted from the corresponding monotonic loading models, whenever $\tau_f(N)$ is known.

Upon using the sliding function proposed for SiC/SiC composites [114] indicated on Fig. 59a

$$\tau_f = \tau_0 N^{-\xi} \qquad 1 < N < N_s \tag{86a}$$

$$\tau_f = \tau_{ss} \qquad N > N_s \tag{86b}$$

the following predictions can be generated. The threshold stress, S_{th}, when GLS applies, is given by inserting Equation 10 into Equation 17a with τ_0 replaced by τ_{ss}

$$S_{th}/S_g = (\tau_{ss}/\tau_0)^{1/(m+1)} \tag{87}$$

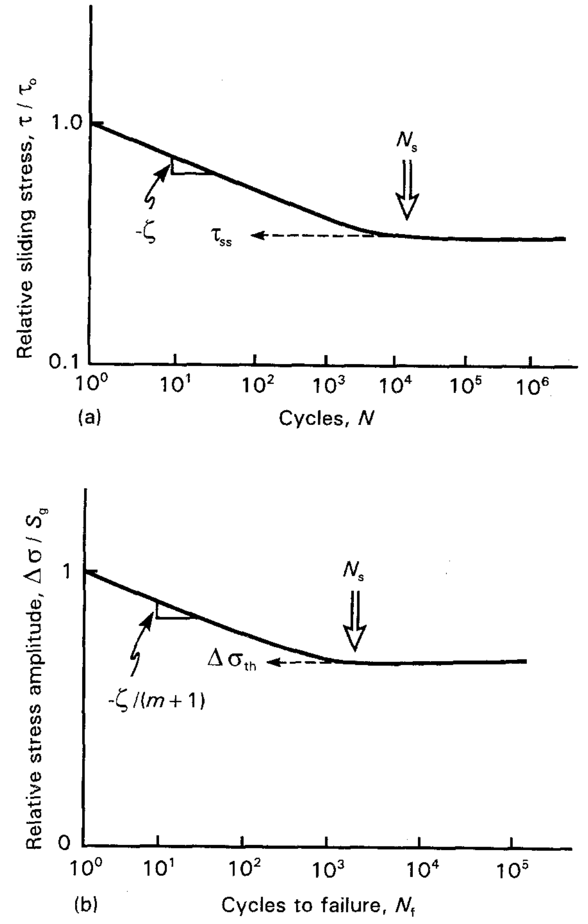

Figure 59 (a) Effect of fatigue on the interface sliding stress (schematic representation). (b) Corresponding fatigue (σ–N) curve.

This threshold occurs after N_s cycles. At intermediate cycles, $N < N_s$, the retained strength, S_R, is derived as

$$S_R/S_g = N^{-\xi/(m+1)} \tag{88}$$

These results can be combined to yield a fatigue (σ–N) curve (Fig. 59b). Upon comparing with measured fatigue curves, these predictions provide a straightforward means of determining whether fibre degradation occurs.

The change in the unloading modulus during fatigue occurs at fixed crack density, as evident from Equation 54. For example, when the sliding resistance has been reduced to steady-state, τ_{ss}, the reduction in the unloading modulus, $\Delta\bar{E}$, is given by

$$\frac{\Delta\bar{E}}{\bar{E}_i} = \frac{(1 - \bar{E}_i/E_*)(\tau_0/\tau_{ss} - 1)}{1 + (1 - \bar{E}_i/E_*)(\tau_0/\tau_{ss} - 1)} \tag{89}$$

where $\bar{E}_i$ is the initial unloading modulus.

8.4. Thermomechanical fatigue

The basic matrix crack growth model can be extended to include thermomechanical fatigue (TMF). This can be achieved by means of another transformation wherein all of the stress range terms in Equations 79–85, $\Delta\sigma$ and $\Delta\sigma_b$ are replaced, by the tractions, Δt

and Δt_b, respectively. The specific transformations are [120].

$$\Delta t = \Delta\sigma + fE_f(\alpha_f - \alpha_m)\Delta T \qquad (90a)$$

$$\Delta t_b = \Delta\sigma_b + fE_f(\alpha_f - \alpha_m)\Delta T \qquad (90b)$$

where ΔT represents the temperature cycle and $\Delta\sigma$ the stress cycle. With these transformations, it is possible to represent the crack growth using two non-dimensional parameters, $\Delta\mathcal{E}_0$ and $\Delta\mathcal{E}_T$ (Table III) that specify the stress cycling and the temperature cycling, respectively. It is immediately apparent that matrix crack growth and fibre failure are expected to be quite different for out-of-phase and in-phase TMF.

For materials in which $\alpha_m > \alpha_f$, in-phase TMF causes Δt to be less than that expected for stress cycling alone and vice versa. These effects are apparent from trends in the stress intensity range, ΔK_{tip} (Fig. 60), calculated for cases wherein fibre failure does not occur. A key result is that, whereas ΔK_{tip} always reduces upon initial crack extension either for stress cycling alone or for in-phase TMF, it can increase for out-of-phase TMF. Furthermore, for extreme ratios of $\Delta\mathcal{E}_T$ to $\Delta\mathcal{E}_0$, ΔK_{tip} can exceed that for the monolithic matrix without fibres. This result implies that the crack growth rate also exceeds that for the monolith.

When fibre failure effects are introduced, in-phase and out-of-phase cycling result in behaviour that opposes that associated with matrix crack growth. Namely, the crack size a_f, at which fibre failure commences is smaller for in-phase loading than for out-of-phase loading (Fig. 61). Consequently, in order to ensure a threshold, the material is required to operate under conditions of fibre integrity. Then, in-phase TMF represents the more severe problem.

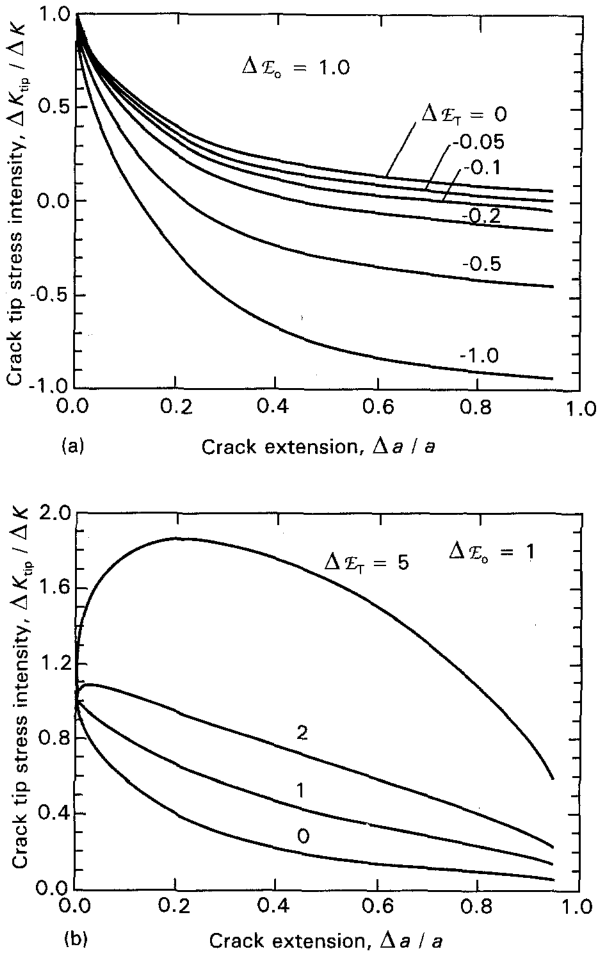

Figure 60 Effects of TMF on the tip stress intensity factor, (a) in phase, (b) out-of-phase.

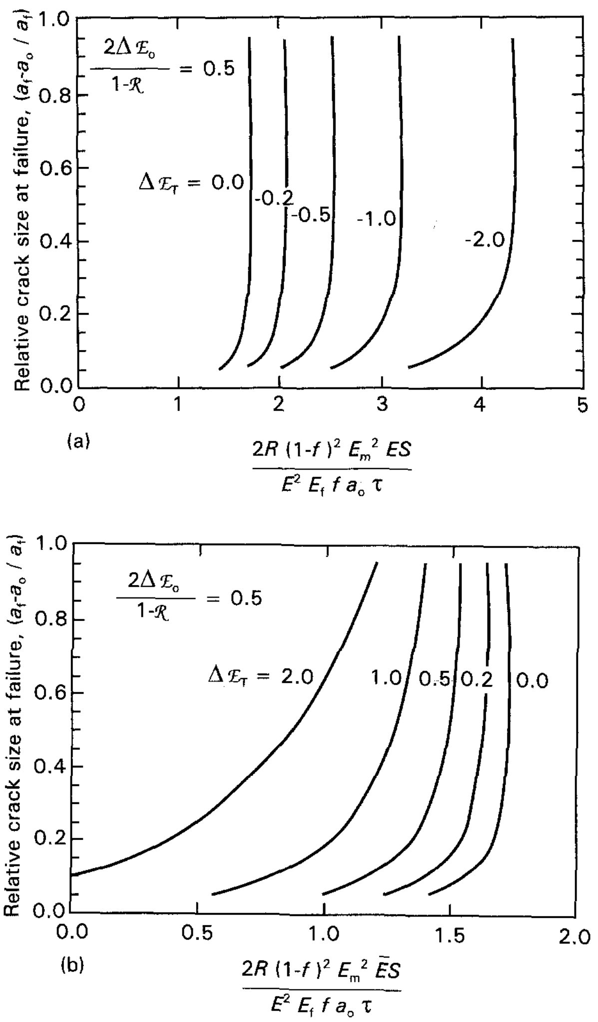

Figure 61 Effects of TMF on the crack size at which fibre failure occurs, (a) in phase, (b) out-of-phase.

8.5. Experimental results

Experimental measurements performed on CMCs and titanium MMCs reflect features associated with the cyclic degradation of the sliding stresses and fibre strength and also provide a critique of crack growth criteria. These features are manifest in phenomena ranging from the growth characteristics of individual cracks, to changes in modulus to fatigue life curves. The salient cyclic and static fatigue characteristics are illustrated using various experimental results .

The growth of individual cracks has been investigated on titanium MMCs, but not on CMCs. The crack growth trends found in titanium MMCs are in broad agreement with the predictions of the matrix crack growth models (Fig. 62), upon using a Paris law applicable to the matrix (Equation 77). The results indicate that sliding stress, τ, decreases upon cycling, because of "wear" mechanisms operating within the fibre coating [117–119, 121]. The reduction in τ occurs

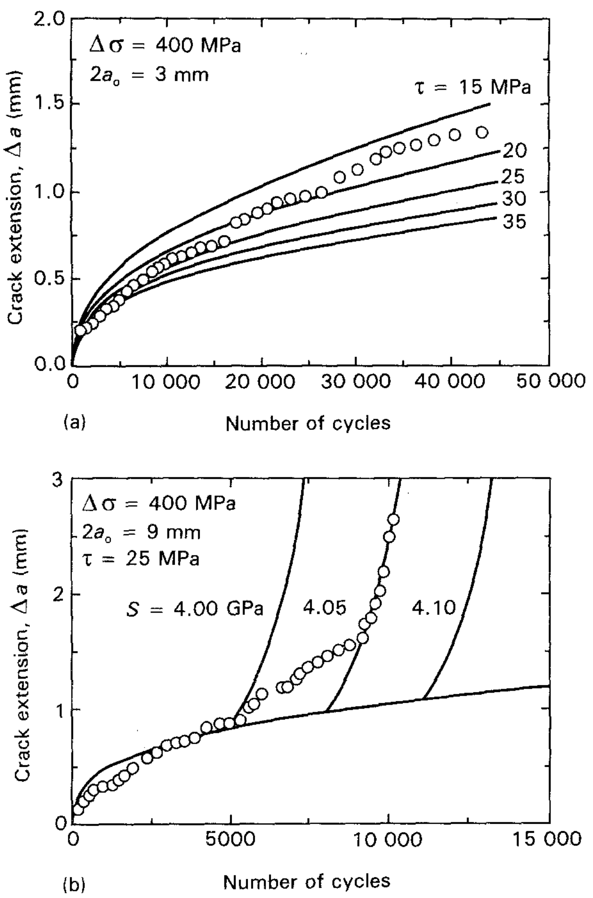

Figure 62 Comparison between experimental crack growth results and predictions for unidirectional SiC/Ti composites: (a) experiments for small notches with predictions made for several τ, (b) experiments for larger notches and predictions for $\tau = 25$ MPa at several values of fibre strength S (Fig. 57).

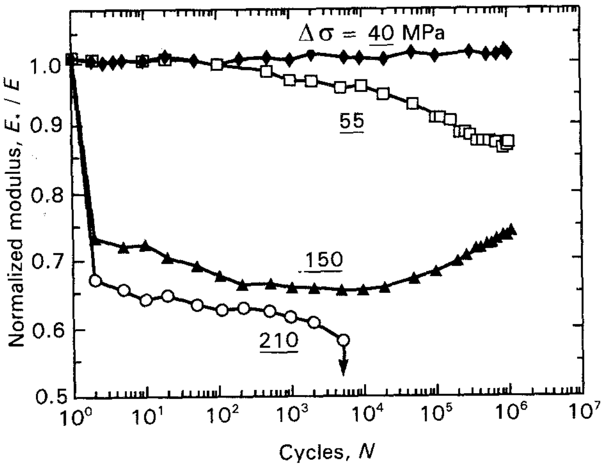

Figure 63 Modulus reduction found upon fatigue in a glass matrix composite [10].

after a relatively small number of cycles (< 1000) and thereafter, remains at an essentially constant value, τ_{ss}, consistent with Equation 86. It is also evident for these materials that the fibre strength if not degraded by cyclic sliding of the interface, even after $> 10^5$ cycles.

Tensile fatigue testing of CMCs has been conducted under conditions which produce multiple cracking. There are consequent changes in modulus and hysteresis loop width, which relate to the fatigue life. Such results do not provide a critical test of the matrix crack growth criterion, but clearly illustrate the influence of cycling on the interface sliding stress and the fibre strength. Reductions in unloading modulus, $\bar{E}$, are found at fixed stress amplitude (Fig. 63) [10, 122]. In some cases, there is also a small subsequent increase. The modulus changes have been analysed, such that constituent properties during fatigue may be obtained. For example, measurements made for SiC/CAS (at frequencies < 10 Hz) have been correlated with the crack density (Fig. 64), such that comparisons may be made with predictions, based on Equation 89. This analysis indicates a substantial reduction in sliding stress, from $\tau_0 \approx 15$ MPa for the pristine composite [121] to $\tau_{ss} \approx 5$ MPa. Fatigue life data for SiC/SiC (CVI) composites provide similar information [114]. Analysis of S_{th}, may be made using Equation 87, subject to the assumption that there is no fibre degradation. The analysis indicates that $\tau_{ss}/\tau \approx 0.38$. This degradation in τ is similar to that found for SiC/CAS and titanium MMCs, described above. A commonality regarding the changes in interface sliding that occur upon fatigue thus appears to be emerging. Note that the fatigue threshold stress, S_{th}, is a relatively large fraction of the UTS ($S_{th}/S_g \approx 0.7$) when fatigue causes interface degradation, but does not degrade the fibres. The ratio S_{th}/S_g is larger than that usually found for metals.

At higher frequencies ($\gtrsim 50$ Hz), frictional heating also occurs, accompanied by a larger reduction in τ [123]. The hypothesis is that the frictional heating causes the carbon fibre coating to be eliminated. Such behaviour would be consistent with that found upon isothermal heat treatment [56].

The occurrence of cyclic fatigue failure at peak stresses substantially lower than the UTS (Fig. 65) has been found at high temperatures and, especially, for TMF. Such results suggest that the fibre strength systematically diminishes for certain cyclic thermomechanical loadings. There are three primary mechanisms of fibre weakening: abrasion, oxidation and stress corrosion. These mechanisms might be distinguished in the following manner. The strength

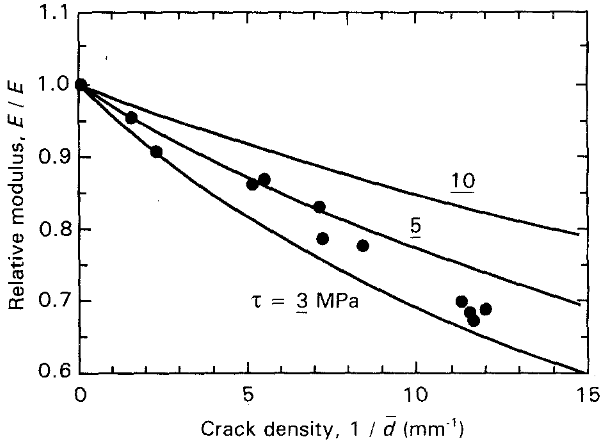

Figure 64 (●) Influence of cyclic loading on modulus reduction as a function of crack density for a unidirectional CAS/SiC composite indicating that τ has been decreased by fatigue. (——) Theory.

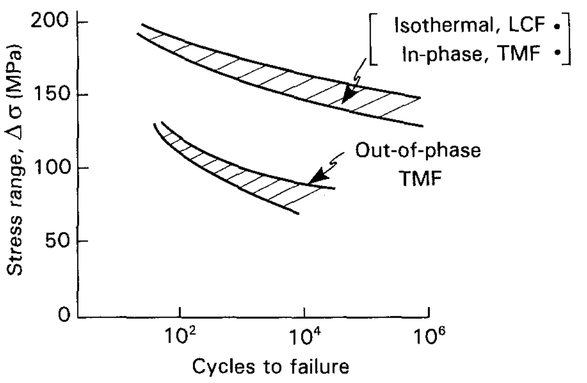

Figure 65 Isothermal fatigue and TMF data for a glass matrix composite [2].

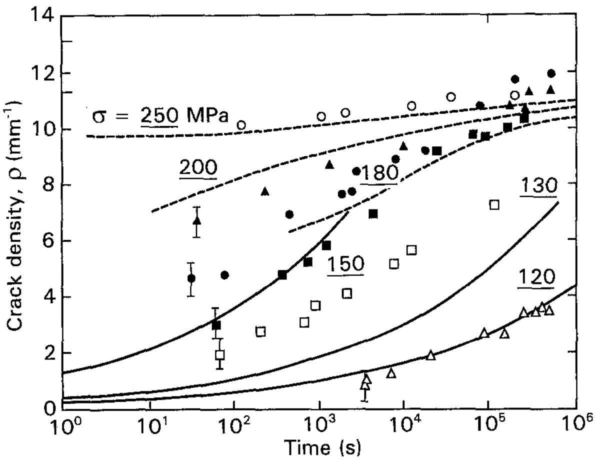

Figure 67 Experimental measurements and simulations at (——) low and (- - -) high stress of matrix crack evolution in a SiC/CAS composite caused by stress corrosion at constant stress. Flexure: (△) 120 MPa, (□) 130 MPa, (■) 150 MPa, (●) 180 MPa, (▲) 200 MPa, (○) 250 MPa.

degradation caused by stress corrosion occurs abruptly, following time accumulated at peak load [115]. Abrasion occurs systematically with cyclic sliding at the interfaces (Fig. 66) and should be enhanced by out-of-phase TMF, which accentuates the sliding displacement. Oxidation is strictly time and temperature dependent. The strong effect of out-of-phase TMF on the fatigue life at high temperature [2] suggests that fibre degradation by abrasion is an important mechanism, perhaps accentuated by oxide formation at higher temperatures. Much additional study is required on this topic.

In some CMCs, modulus changes and rupture occur at constant stress [122]. Substantial matrix crack growth has been found at stresses below that required to produce cracks in short duration, monotonic tensile tests. Furthermore, the crack densities following extended periods under load (~ 10^6 s) are higher than those obtained in the short duration tests. The development of cracks with time and stress (Fig. 67) has been considered to involve stress corrosion of the matrix. The behaviour is consistent with a revised matrix crack growth criterion (Equation 78) without any changes in the sliding stress. Fibre weakening may also be occurring by stress corrosion.

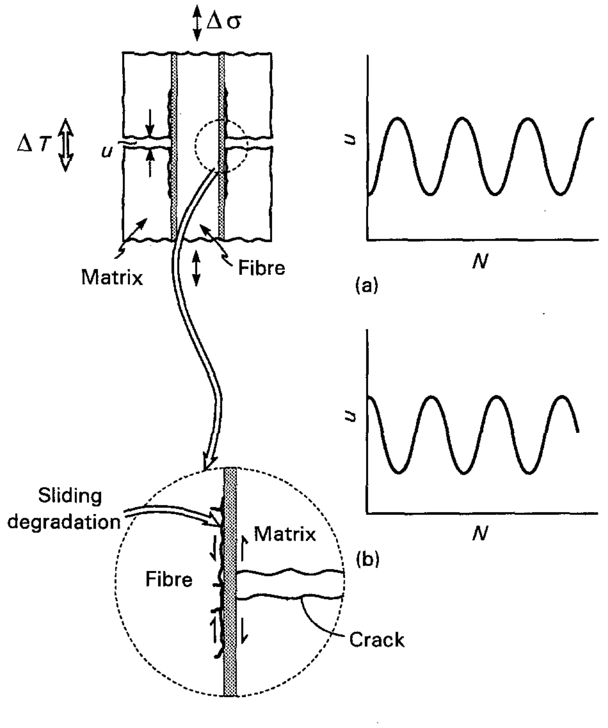

Figure 66 Mechanism of fibre degradation by fatigue, coupled with oxidation. (a) load cycling, (b) thermal cycling.

9. Creep

9.1. Basic behaviour

The creep behaviour and relationships with constituent properties are critically influenced by fibre failure, matrix cracks and interface debonding. Some of the basic stress–time characteristics are sketched in Figs 68 and 69. When the fibres and matrix are intact and the interfaces are bonded, the creep deformations of the composite and the constituent properties are related in a straightforward manner [124, 125]. When

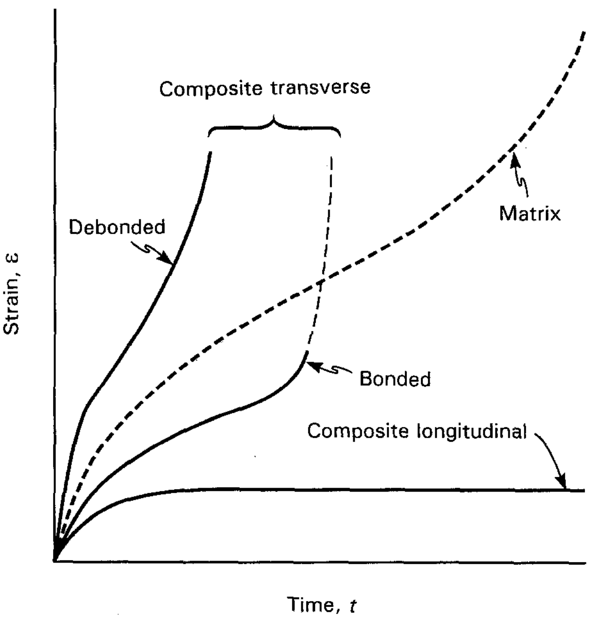

Figure 68 Schematic illustration of creep anisotropy in unidirectional CMCs.

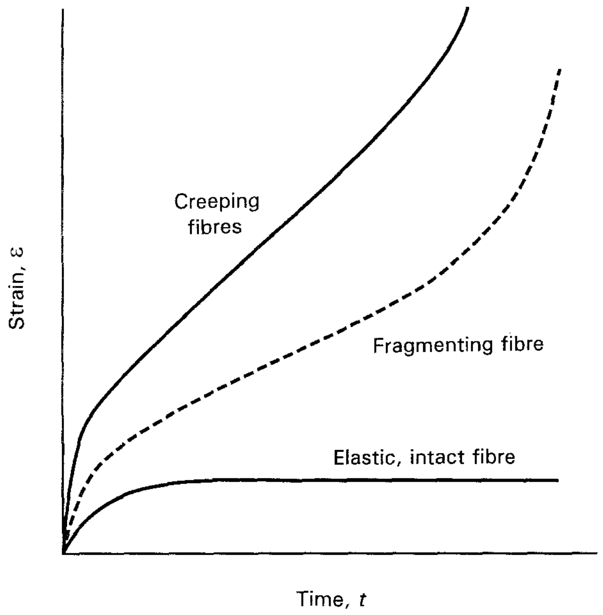

Figure 69 Schematic illustration of effects of intact and creeping fibres, as well as fibre failure on the longitudinal creep.

one constituent is elastic (fibre or matrix) and the other creeps, the longitudinal creep strain is transient and stops when all of the strain is transferred on to the elastic material (Figs 68 and 69) [124]. The creep law needed to describe this behaviour is

$$\dot{\varepsilon}_{ij} = \frac{1}{2G}\dot{s}_{ij} + \frac{1}{9K}\delta_{ij}\dot{\sigma}_{kk} + \frac{3}{2}B\sigma_e^{n-1}s_{ij} + \alpha\delta_{ij}\dot{T} \quad (91)$$

where $\dot{\varepsilon}$ is the strain rate, $\dot{\sigma}$ is the stress rate, δ_{ij} is the Kronecker delta, n is the creep index, s_{ij} is the deviatoric stress and the effective stress, σ_e, is defined by

$$\sigma_e = (\tfrac{3}{2}s_{ij}s_{ij})^{1/2} \quad (92)$$

and B is the rheology parameter for steady-state creep

$$B = \dot{\varepsilon}_0/\sigma_0^n \quad (93)$$

with σ_0 being the reference stress and $\dot{\varepsilon}_0$ is the reference strain rate. If the fibres are elastic and the matrix creeps, the stress in the matrix, σ_m, evolves at constant applied stress as ($n \neq 1$) [124, 125]

$$\sigma_m(t) = \left\{\frac{(n-1)fE_fE_mBt}{E_L} + \frac{1}{[\sigma_m(0)^{n-1}]}\right\}^{1-n} \quad (94)$$

where $\sigma_m(0)$ is the matrix stress at time, $t = 0$. When the matrix stress, $\sigma_m \rightarrow 0$, the stress on the fibres increases to, $\sigma_f = \sigma/(1-f)$, such that the transient strain, ε_t, is

$$\varepsilon_t = \sigma/E_f(1-f) \quad (95)$$

Similar results apply when the fibres creep, but the matrix is elastic.

When both the fibre and the matrix creep, steady-state develops in the composite following an initial transient (Fig. 69). The evolution of the matrix stress occurs according to [124]

$$\left[\frac{E}{fE_mE_f}\right]\dot{\sigma}_m = B_m\sigma_m^{n_m} - B_f\left[\frac{\sigma-(1-f)\sigma_m}{f}\right]^{n_f} \quad (96)$$

where n_m and n_f are the creep indices for the matrix and fibres, respectively. When a steady-state is reached ($\dot{\sigma}_m = 0$), σ_m and σ_f are related by

$$[\sigma_m^{n_m}(B_m/B_f)]^{1/n_f} + \frac{(1-f)}{f}\sigma_m = \frac{\sigma}{f} \quad (97)$$

and

$$\dot{\sigma}_m(1-f) + \sigma_f f = \sigma \quad (98)$$

These formulae can be solved for specific n_m and n_f to obtain σ_m and σ_f. With the stresses known the composite creep rate can be readily obtained.

Transverse creep with well-bonded fibres is usually matrix dominated. Solutions which have been generated for bonded rigid fibres thus have utility. All such solutions indicate that the creep attains steady-state, with a creep-rate lower than that for the matrix alone (Fig. 68). Moreover, strengthening solutions derived for transverse deformation with a power law hardening matrix (Fig. 70) also apply to a power law creeping matrix, in steady-state (with the strains becoming the strain rates). The reduction in creep rate depends on the power law exponent for the matrix and the spatial arrangement of the fibres. For a composite with a square arrangement of fibres, and a matrix subject to diffusional creep ($n_m = 1$), because there is no creep in the fibre direction, z [124]

$$\dot{\varepsilon}_{yy} = -\dot{\varepsilon}_{xx} = (\sigma_{yy} - \sigma_{xx})k_1(f) \quad (99)$$

with

$$k_1(f) = (3/4)[(1-f)/(1+2f)] \quad (100)$$

In essence, k_1 gives the reduction in creep-rate upon incorporating the bonded fibres. For non-linear matrices, the equivalent results have the form

$$\dot{\varepsilon}_{xx} = -\dot{\varepsilon}_{yy} = B_m(\sigma_{xx} - \sigma_{yy})^{n_m-1}(\sigma_{xx} - \sigma_{yy})k_n(f) \quad (101)$$

where k_n is a function of the fibre volume fraction and spatial arrangement. For example, when $n_m = 5$ and a square fibre array is used

$$k_n = 0.42[(1-f)/(1-f^2)]^5 \quad (102)$$

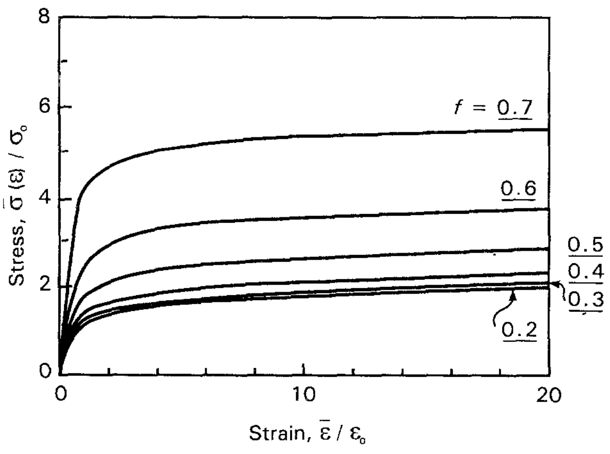

Figure 70 Transverse strength of a unidirectional composite with a power law hardening matrix.

9.2. Effect of fibre failures

When stresses are applied along the fibre axis in a system with a creeping matrix, the time-dependent stress elevation on the fibres may cause some fibre failures. Following fibre failure, sliding would initiate at the interface, accompanied by further creep in the matrix. The time constant for this process is much longer than that for the initial transient, described above, and can be analysed as a separate creep problem [124]. While the process in complicated, several factors are important. If the stress on the fibres reaches their strength, S, the composite will fail. Moreover, the relevant S is probably that with a small τ, associated with creep sliding of the interface. In this limit, composite failure is possible at all stresses above the "dry bundle" strength, S_b (Equation 17c). Conversely, the composite cannot rupture at stress below S_b, unless the fibres are degraded by creep. The dry bundle strength thus represents a "threshold". At stresses below S_b, creep must be transient.

At higher stresses, the fibres fracture and may fragment. Then, steady-state creep is possible (Fig. 68), proceeding in accordance with a creep law devised for a material with aligned rigid reinforcements of finite aspect ratio. This behaviour is represented by the Mileiko model [126]. The solution for a non-sliding interface is [124, 127]

$$\dot{\varepsilon} = B_m\sigma^{n_m}(R/L_f)^{n_m+1}\mathscr{L}(n_m, f) \qquad (103)$$

where L_f is the fragment length and

$$\mathscr{L}(n_m, f) = 2^{n_m+1}3^{1/2}\left[\frac{3^{1/2}(2n_m+1)}{2n_m f}\right]^{n_m}\frac{(1-f)^{(n_m-1)/2}}{(n_m-1)} \qquad (104)$$

However, the fragment length decreases as the stress increases. This occurs in accordance with the scaling [28]

$$L_f/R \sim (S_c/\sigma)^m \qquad (105)$$

Upon inserting Equation 105 into Equation 103, it is evident that steady-state creep-rate should occur with a large power law exponent, $n_m + m + mn_m$ [124]. Such behaviour has been reported in composites with discontinuous fibres [128]. The overall behaviour is sketched in Fig. 71. In practice, because of the large stress exponent at stress above S_b, adequate creep performance can only be ensured at stresses below S_b.

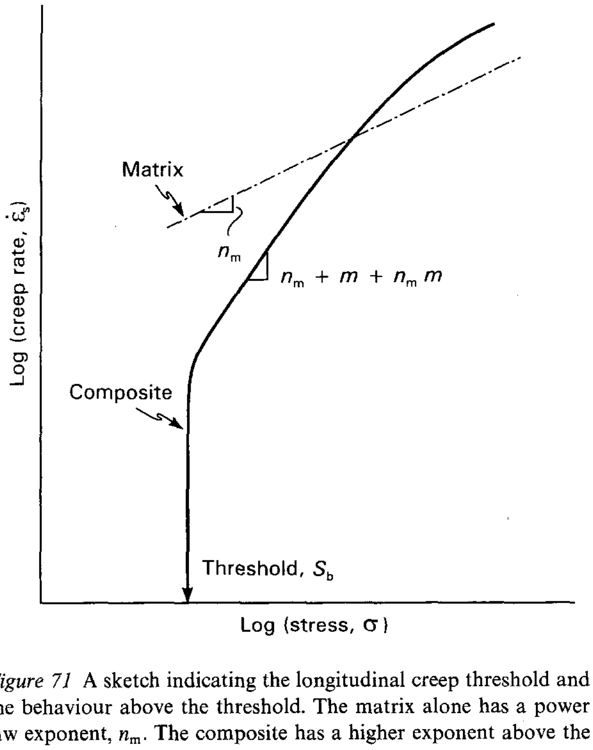

Figure 71 A sketch indicating the longitudinal creep threshold and the behaviour above the threshold. The matrix alone has a power law exponent, n_m. The composite has a higher exponent above the threshold associated with stress-induced fibre fragmentation.

9.3. Interface debonding

While there are no solutions known to the authors for transverse creep with debonding interfaces, the analogy (noted above) between power law deformation and steady-state creep provides insight. Calculations of transverse deformation with and without interface bonding (Fig. 72) indicate a major strength degradation when debonding occurs [129, 130]. Furthermore, the composite behaviour approaches that for a body containing cylindrical holes. Creep results for porous bodies may thus provide rough estimates of the transverse creep strength when the interfaces debond.

9.4. Matrix cracking

In some CMCs, the fibres creep more readily than the matrix. Such materials include SiC/SiC and SiC/Si_3N_4. In this case, fibre creep and matrix cracking appear to proceed in a synergetic manner that accelerates the creep and causes premature creep rupture. The basic phenomenon is as follows. Creep in the fibre increases the stress on the matrix, as described above. Above a threshold, the stress on the matrix then exceeds σ_τ (Equation 64), causing multiple matrix cracks to form in the 90° plies. These cracks gradually extend into the 0° plies, because creep of the fibres relaxes the bridging tractions. As a result, the stress at these locations is borne entirely by the fibres, which creep, without impediment, leading to rupture of the composite (Fig. 73). The creep analogy of the tunnelling stress, σ_τ (equation 67) represents a threshold stress. At stresses above σ_τ, matrix cracks eventually extend across the composite and the composite fails by fibre rupture. The rupture ductility of polycrystalline

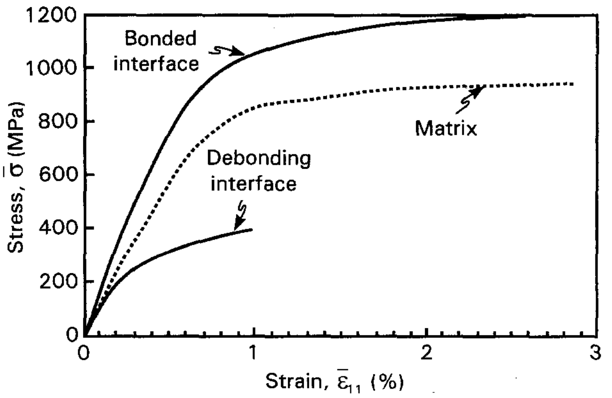

Figure 72 Comparison of transverse behaviour with and without interface debonding.

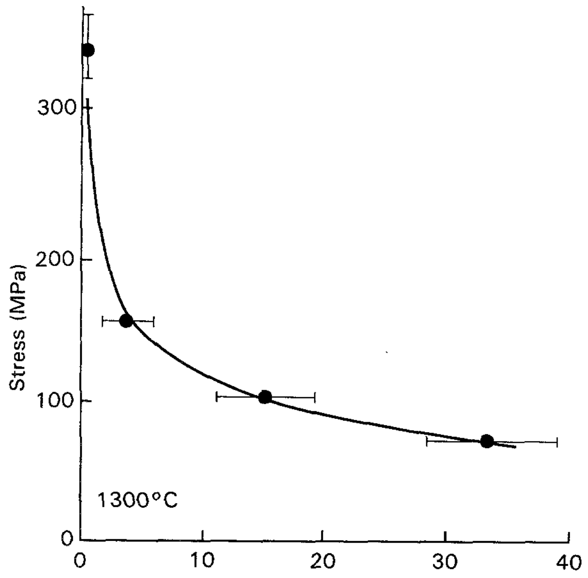

Figure 73 Creep rupture data for a SiC/C composite which is susceptible to fibre creep and matrix cracking.

ceramic fibres is typically quite low, because of void formation along the grain boundaries. Consequently, matrix cracking often leads to creep rupture with brittle characteristics.

9.5. Strain recovery

Because creep in composites redistributes stresses between matrix and fibre, strain recovery must occur when the loads are removed [131]. This behaviour is well established for a system with one elastic constituent and one viscoplastic constituent, in accordance with standard Kelvin concepts. Notably, the elastic stretch in one constituent is gradually relaxed when the load is removed. The specifics depend, of course, on the nature of the viscoplasticity. A simple example illustrates the salient phenomena. A composite with elastic fibres and a creeping matrix, loaded along the fibre direction, has been crept until the stress in the matrix is essentially zero (Fig. 74). The load is then removed. The instantaneous elastic shrinkage, $\Delta\varepsilon$, must satisfy

$$\Delta\varepsilon = \frac{\sigma_m}{E_m} = \frac{\Delta\sigma_f}{E_f} \qquad (106)$$

The stresses after elastic unloading are thus

$$\sigma_m = -\frac{f\sigma E_m}{(1-f)E_L} \qquad (107a)$$

$$\sigma_f = \sigma E_m / E_L \qquad (107b)$$

Thereafter, holding at temperature causes σ_m to relax according to Equation 94, with $\sigma_m(0)$ given by Equations 107a and b.

9.6. Experimental results

Experimental data for a range of different composites are used to illustrate some of the features described above and to anticipate trends. The longitudinal behaviour found when the fibres are elastic is addressed first. Results obtained on TiAl reinforced with sapphire fibres (Fig. 75) establish the existence of transient creep in the longitudinal orientation when the fibres are elastic and intact, but the matrix is subject to creep [132]. At higher loads, when some fibres fail, creep can continue and rupture may occur, as demonstrated by data obtained on a titanium matrix composite reinforced with SiC fibres (Fig. 76). Removal of the load after creep results in reverse deformation, as demonstrated for a SiC/Si_3N_4 composite (Fig. 74). Upon using a creep index applicable to monolithic Si_3N_4 ($n = 2$), the stress in the matrix relaxes in the manner

$$\sigma_m = \left[\frac{fE_f E_m B t}{E_L} - \frac{(1-f)E_L}{f\sigma E_m}\right]^{-1} \qquad (108)$$

Note that B has units $(\text{stress})^{-2}$.

The inverse situation may also be important in some CMCs, wherein the fibres creep but the matrix is elastic [132, 133]. Typical examples include SiC/SiC and SiC/Si_3N_4 composites, which have SiC fibres with fine grain size (such as Nicalon). In these materials,

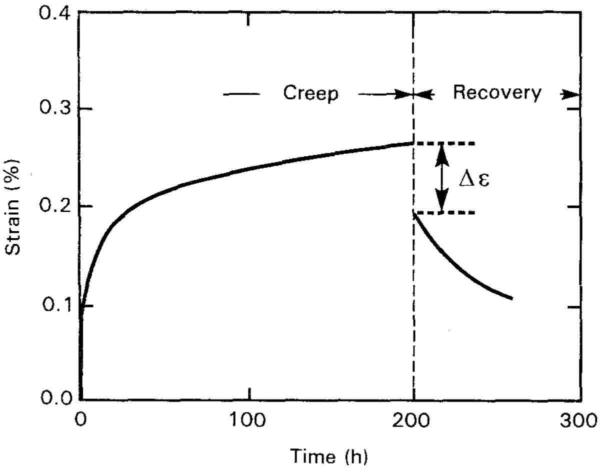

Figure 74 Creep recovery effects in a SiC/Si_3N_4 with "elastic" fibres and a creeping matrix [131].

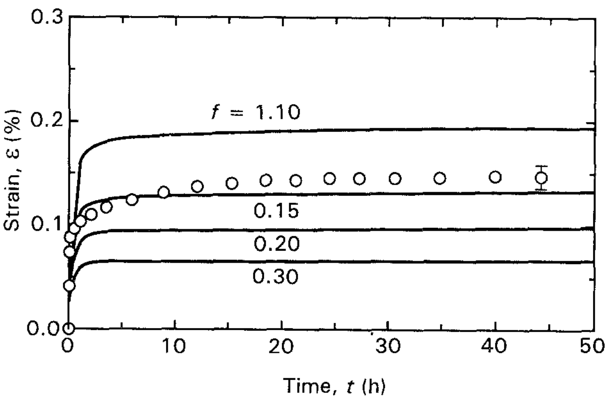

Figure 75 Transient longitudinal creep in a TiAl matrix composite reinforced with sapphire fibres [132]. (○) experiments, (——) model.

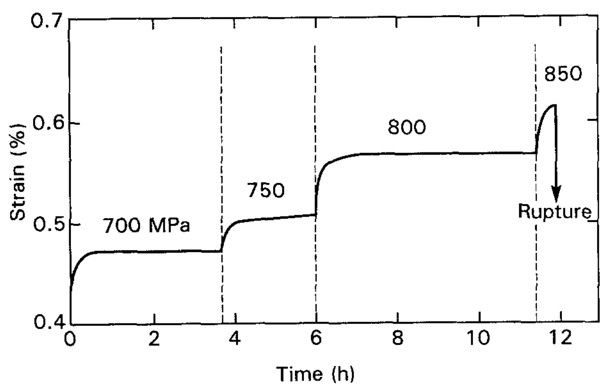

Figure 76 Transient creep and rupture data obtained for a SiC/Ti composite subject to incremental loading [134].

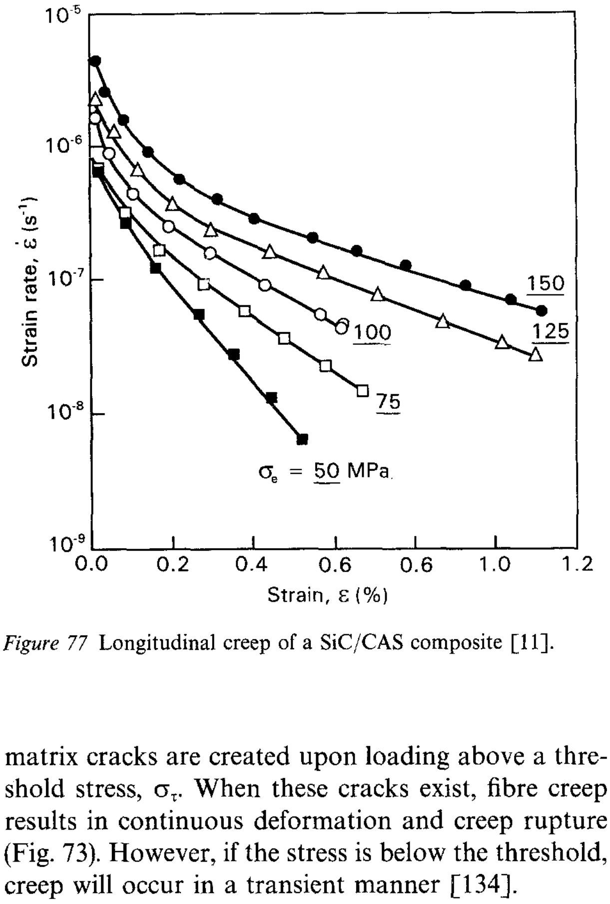

Figure 77 Longitudinal creep of a SiC/CAS composite [11].

matrix cracks are created upon loading above a threshold stress, σ_T. When these cracks exist, fibre creep results in continuous deformation and creep rupture (Fig. 73). However, if the stress is below the threshold, creep will occur in a transient manner [134].

When both the matrix and fibres creep, and there are no matrix cracks, continued deformation of the composite proceeds in the longitudinal orientation [11]. Results obtained on CAS/SiC (Fig. 77) verify that creep continues. However, interpretation is complicated by microstructural changes occurring in the fibres, which lead to creep hardening. The deformation is thus entirely primary in nature. These results identify microstructural stability as an important fibre selection criterion.

10. Challenges and opportunities

Reasonable progress has been made in understanding inelastic strain mechanisms, although the continued development of models and experimental validation is necessary. It is now possible to appreciate how stress redistribution occurs and to characterize the notch sensitivity. The analysis of the degradation mechanism is much less mature.

There are several challenges and opportunities that arise. With regard to the short duration performance, it is necessary to develop simple constitutive laws that can be used with finite element codes in order to calculate stresses around attachments, holes, etc. Mechanism-based models of the inelastic strain are preferred for this purpose. However, there is insufficient basic understanding about the inelastic strains that occur upon shear loading and their dependence on constituent properties. Basic inelastic strain models with matrix cracks inclined to the fibres are needed to address this deficiency.

Degradation mechanisms that operate upon cyclic loading in the presence of matrix cracks require concerted study. Interface changes and fibre degradation are both possible. Moreover, there may be detrimental synergistic interaction with the environment. The models developed for MMCs indicate that the retention of fibre strength upon cyclic loading is particularly important, because this strength governs the fatigue threshold. Mechanisms and models that predict fibre strength degradation are critically important.

References

1. K. M. PREWO, *J. Mater. Sci.* **17** (1982) 3549.
2. S. MALL, D. E. BULLOCK and J. J. PERNOT, to be published.
3. C. CADY, T. J. MACKIN and A. G. EVANS, *J. Am. Ceram. Soc.* (1993) in press.
4. A. G. EVANS, J. M. DOMERGUE and E. VAGAGGINI, *ibid.* in press.
5. V. C. NARDONNE and K. M. PREWO, *J. Mater. Sci.* **23**, (1988) 168.
6. R. Y. KIM and N. PAGANO, *J. Am. Ceram. Soc.* **74** (1991) 1082.
7. H. C. CAO, E. BISCHOFF, O. SBAIZERO, M. RÜHLE and A. G. EVANS, *ibid.* **73** (1990) 1691.
8. A. W. PRYCE and P. SMITH, *J. Mater. Sci.* **27** (1992) 2695.
9. K. M. PREWO, *ibid.* **22** (1987) 2595.
10. L. P. ZAWADA, L. M. BUTKUS and G. A. HARTMAN, *J. Am. Ceram. Soc.* **74** (1991) 2851.
11. C. WEBER and A. G. EVANS, *ibid.* (1993) in press.
12. G. BAO and Z. SUO, *Appl. Mech. Rev.* **45** (1992) 355.
13. J. AVESTON, G. A. COOPER and A. KELLY, in "The Properties of Fiber Composites", NPL Conference Proceedings (IPC Publishing, Guildford, 1971) pp. 15–26.
14. W. A. CURTIN, *J. Am. Ceram. Soc.* **74** (1991) 2837.
15. A. G. EVANS and D. B. MARSHALL, *Acta Metall.* **37** (1989) 2567.
16. A. G. EVANS and F. W. ZOK, in "Topics In Fracture and Fatigue", edited by A. S. Argon (Springer-Verlag, NY, 1992) pp. 271–308.
17. E. VAGAGGINI, J. M. DOMERGUE and A. G. EVANS, *J. Am. Ceram. Soc.* (1993) in press.
18. J. B. DAVIS, J. P. A. LÖFVANDER, A. G. EVANS, E. BISCHOFF and M. L. EMILIANI, *ibid.* **76** (1993) 1249.
19. A. G. EVANS, F. W. ZOK and J. DAVIS, *Compos. Sci. Technol.* **42** (1991) 3.
20. M. Y. HE, B. X. WU, A. G. EVANS and J. W. HUTCHINSON, *Mech. Mater.* (1993) in press.
21. A. G. EVANS, *Mater. Sci. Eng.* **A143** (1991) 63.
22. B. N. COX, *Acta Metall. Mater.* **39** (1991) 1189.
23. B. N. COX and C. S. LO, *ibid.* **40** (1992) 69.
24. B. N. COX and D. B. MARSHALL, *Fatigue Fract. Eng. Mater.* **14** (1991) 847.
25. P. A. BRØNDSTED, F. E. HEREDIA and A. G. EVANS, *J. Am. Ceram. Soc.* (1993) in press.

26. F. E. HEREDIA, S. M. SPEARING, P. MOSHER, A. G. EVANS and W. A. CURTIN, *ibid.* **75** (1992) 3017.
27. F. E. HEREDIA, S. M. SPEARING, M. Y. HE, T. J. MACKIN, P. A. BRØNDSTED, A. G. EVANS and P. MOSHER, *J. Am. Ceram. Soc.* (1993) in press.
28. W. A. CURTIN, *J. Mater. Sci.* **26** (1991) 91.
29. J. F. JAMET, D. LEWIS and E. Y. LUH, *Ceram. Eng. Sci. Proc.* **5** (1984) 625.
30. F. W. ZOK and S. M. SPEARING, *Acta Metall. Mater.* **40** (1992) 2033.
31. D. B. MARSHALL, B. N. COX and A. G. EVANS, *Acta Metall.* **33** (1985) 2013.
32. D. B. MARSHALL and B. N. COX, *Mech. Mater.* **7** (1986) 127.
33. J. W. HUTCHINSON and H. JENSEN, *ibid.* **9** (1990) 139.
34. R. J. KERANS and T. A. PARTHASARATHY, *J. Am. Ceram. Soc.* **74** (1991) 1585.
35. P. D. JERO, R. J. KERANS and T. A. PARTHASARATHY, *ibid.* **74** (1991) 2793.
36. T. MACKIN, P. WARREN and A. G. EVANS, *Acta Metall. Mater.* **40** (1992) 1251.
37. M. Y. HE and J. W. HUTCHINSON, *Int. J. Solids Struct.* **25** (1989),1–53.
38. N. A. FLECK, *Proc. R. Soc.* **A432** (1991) 55.
39. C. XIA and J. W. HUTCHINSON, *Acta Metall. Mater.*, in press.
40. D. B. MARSHALL and W. C. OLIVER, *J. Am. Ceram. Soc.* **70** (1987) 542.
41. R. W. RICE, US Pat. 4642,271, 10 February 1987; assigned to the USA as represented by the Secretary of the Navy.
42. R. W. RICE, J. R. SPANN, D. LEWIS and W. COBLENZ, *Ceram. Eng. Sci. Proc.* **5** (1984) 614.
43. B. BENDER, O. SHADWELL, C. BULIK, L. INCORVATI and D. LEWIS III, *Am. Ceram. Soc. Bull.* **65** (1986) 363.
44. J. J. BRENNAN, in "Tailoring of Multiphase Ceramics", edited by R. E. Tressler, *et al.* Vol. **20** (Plenum, NY, 1986) p. 549.
45. D. B. MARSHALL and A. G. EVANS, *J. Am. Ceram. Soc.* **68** (1985) 225.
46. C. LIANG and J. W. HUTCHINSON, *Mech. Mater.* **14** (1993) 207.
47. T. J. KOTIL, J. W. HOLMES and M. COMNINOU, *J. Am. Ceram. Soc.* **73** (1990) 1879.
48. J. LAMON, P. RABALLIAT and A. G. EVANS, *ibid.* in press.
49. T. MACKIN, J. YANG, C. LEVI and A. G. EVANS, *Acta Metall. Mater.* (1993) in press.
50. J. J. BRENNAN and K. M. PREWO, *J. Mater. Sci.* **17** (1982) 2371.
51. R. NASLAIN, *Compos. Interfaces* **1** (1993) 253.
52. X. BURATT, unpublished research at LCTs, Bordeaux (1993).
53. J. W. HOLMES and S. F. SHULER, *J. Mater. Sci. Lett.* **9** (1990) 1290.
54. J. W. HOLMES and C. CHO, *J. Am. Ceram. Soc.* **75** (1992) 929.
55. R. Y. KIM and A. P. KATZ, *Ceram. Eng. Sci. Proc.* **9** (1988) 853.
56. E. BISCHOFF, M. RÜHLE, O. SBAIZERO and A. G. EVANS, *J. Am. Ceram. Soc.* **72** (1989) 741.
57. B. BUDIANSKY, J. W. HUTCHINSON and A. G. EVANS, *J. Mech. Phys. Solids* **34** (1986) 167.
58. K. K. CHAWLA, "Composite Materials Science and Engineering" (Springer, New York, 1987).
59. F. W. ZOK and A. G. EVANS (1993) to be published.
60. D. BEYERLE, S. M. SPEARING and A. G. EVANS, *J. Am. Ceram. Soc.* **75** (1992) 3321.
61. D. BEYERLE, S. M. SPEARING, F. ZOK and A. G. EVANS, *ibid.* **75** (1992) 2719.
62. Q. MA and D. R. CLARKE, *ibid.* **76** (1993) 1435.
63. Q. MA, H. C. CAO, D. R. CLARKE and A. G. EVANS (1993) to be published.
64. X. YANG and R. J. YOUNG, *J. Mater. Sci.* **28** (1993) 2536.
65. L. PHOENIX and R. RAJ, *Acta Metall. Mater.* **40** (1992) 2813.
66. F. HILD, J. M. DOMERGUE, F. A. LECKIE and A. G. EVANS, *Int. J. Solids Struct.* to be published.
67. R. B. HENSTENBURG and S. L. PHOENIX, *Polym. Compos.* **10** (1989) 389.
68. A. FREUDENTHAL, in "Fracture", edited by H. Liebowitz (Academic Press, NY, 1967) pp. 341–45.
69. J. R. MATTHEWS, W. J. SHACK and F. A. McCLINTOCK, *J. Am. Ceram. Soc.* **59** (1976) 304.
70. H. E. DANIELS, *Proc. R. Soc.* **A183** (1945) 405.
71. H. L. OH and I. FINNIE, *Int. J. Fract.* **6** (1970) 287.
72. M. D. THOULESS and A. G. EVANS, *Acta Metall.* **36** (1988) 517.
73. M. D. THOULESS, O. SBAIZERO, L. S. SIGL and A. G. EVANS, *J. Am. Ceram. Soc.* **72** (1989) 525.
74. M. SUTCU, *Acta Metall.* **37** (1989) 651.
75. H. T. CORTEN, in "Modern Composite Materials", edited by L. J. Broutman and R. H. Krock (Addison, Boston, 1967) p. 27.
76. D. C. PHILLIPS, *J. Mater. Sci.* **9** (1974) 1874.
77. L. CUI and B. BUDIANSKY, *J. Mech. Phys. Solids*, in press.
78. Z. SUO, S. HO and X. GONG, *J. Mater. Eng. Technol.* **15** (1993) 319.
79. K. M. PREWO, *J. Mater. Sci.* **21** (1986) 3590.
80. A. J. ECKEL and R. C. BRADT, *J. Am. Ceram. Soc.* **72** (1989) 435.
81. S. BASTE, R. El GUERJOUMA and B. ANDOIN, *Mech. Mater.* **14** (1992) 15.
82. L. N. McCARTNEY, *Proc. R. Soc.* **A409** (1987) 329.
83. R. M. McMEEKING and A. G. EVANS, *Mech. Mater.* **9** (1990) 217.
84. H. TADA, P. C. PARIS and G. R. IRWIN, "The Stress Analysis of Cracks Handbook" (Del Research Corp., St. Louis, Mo, 1985).
85. C. CHO, J. W. HOLMES and J. R. BARBER, *J. Am. Ceram. Soc.* **75** (1992) 316.
86. S. M. SPEARING and F. W. ZOK, *J. Eng. Mater. Technol.* **115** (1993) 314.
87. R. F. COOPER and K. CHYUNG, *J. Mater. Sci.* **22** (1987) 126.
88. B. HARRIS, R. A. HABIB and R. G. COOKE, *Proc. R. Soc. Ser. A.* **437** (1992) 109.
89. K. PREWO and J. J. BRENNAN, *J. Mater. Sci.* **17** (1982) 1201.
90. *Idem, ibid.* **17** (1980) 463.
91. *Idem, ibid.* **17** (1982) 1201.
92. T. W. COYLE, M. H. GUYOT and J. F. JAMET, *Ceram. Eng. Sci. Proc.* **7** (1986) 947.
93. O. SBAIZERO and A. G. EVANS, *J. Am. Ceram. Soc.* **69** (1986) 481.
94. J. W. HUTCHINSON and Z. SUO, *Appl. Mech. Rev.* **28** (1991) 63.
95. C. XIA, R. R. CARR and J. W. HUTCHINSON, *Acta Metall. Mater.* **41** (1993) 2365.
96. N. LAWS and G. DVORAK, *J. Compos. Mater.* **22** (1980) 900.
97. X. AUBARD Thèse de Doctorat de L'Université de Paris, November 1992.
98. J. M. DOMERGUE, E. VAGAGGINI and A. G. EVANS (1993) *J. Amer. Ceram. Soc.*, in press.
99. H. CHAI, *Composites* **15** (1984) 277.
100. S. M. SPEARING and A. G. EVANS, *Acta Metall.* **40** (1992) 2191.
101. D. A. W. KAUTE, H. R. SHERCLIFF and M. F. ASHBY, *Acta Metall. Mater.* (1993) to be published.
102. G. BAO, B. FAN and A. G. EVANS, *Mech. Mater.* **13** (1992) 59.
103. R. BORDIA, B. J. DALGLEISH, P. G. CHARALAMBIDES and A. G. EVANS, *J. Am. Ceram. Soc.* **74** (1991) 2776.
104. F. W. ZOK, O. SBAIZERO, C. HOM and A. G. EVANS, *J Am. Ceram. Soc.* **74** (1991) 187.
105. F. W. ZOK and C. L. HOM, *Acta Metall. Mater.* **38** (1990) 1895.
106. J. BOWLING and G. W. GROVES, *J. Mater. Sci.* **14** (1979) 43.
107. H. R. BAKIS, H. R. YIH, W. W. STINCHCOMB and K. L. REIFSNIDER, ASTM STP 1012 (American Society for Testing and Materials, Philadelphia, PA, 1989) pp. 66–83.

108. W. W. STINCHCOMB and C. E. BAKIS, in "Fatigue of Composite Materials", edited by K. L. Reifsnider (Elsevier Science, NY, 1990) pp. 105–80.
109. M. C. SHAW, D. B. MARSHALL, M. DHADKAH and A. G. EVANS, *Acta Metall. Mater.* **41** (1993) 3311.
110. N. HARWOOD and W. M. CUMMINGS, "Thermoelastic Stress Analysis" (Adam Hilger IOP, NY, 1991).
111. T. J. MACKIN, A. G. EVANS, M. Y. HE and T. E. PURCELL (1993) *J. Amer. Ceram Soc.*, in press.
112. S. E. MOLIS and D. R. CLARKE, *J. Am. Ceram. Soc.* **73** (1990) 3189.
113. C. Q. ROUSSEAU, ASTM STP 1080, edited by J. M. Kennedy, H. H. Moeller and W. S. Johnson (American Society for Testing and Materials, Philadelphia, PA, 1990) pp. 240–52.
114. D. ROUBY and P. REYNAUD, in "Ceramic Matrix Composites", AGARD Conference Proceedings 795, Antalya, Turkey (Specialist Printers, Loughton, 1993).
115. S. M. WEIDERHORN, *J. Am. Ceram. Soc.* **50** (1967) 45.
116. M. SENSMEIER and K. WRIGHT, in "Proceedings TMS Fall Meeting", edited by P. K. Law and M. N. Gungor (ASM, Pittsburgh, 1989) p. 441.
117. D. WALLS, G. BAO and F. ZOK, *Scripta Metall. Mater.* **25** (1991) 911.
118. *Idem, Acta Metall. Mater.* **41** (1993) 2061.
119. D. WALLS and F. W. ZOK, in "Advanced Metal Matrix Composites for Elevated Temperatures", edited by M. N. Gungor, E. J. Lavernia and S. G. Fishman (ASM, Metals Park, OH, 1991) p. 101.
120. G. BAO and R. McMEEKING, *Acta Metall. Mater.* (1993) in press.
121. T. MACKIN and F. W. ZOK, *J. Am. Ceram. Soc.* **75** (1993) 3169.
122. S. M. SPEARING, F. W. ZOK and A. G. EVANS, *ibid.* **77** (1994) 562.
123. J. W. HOLMES, *ibid.* **74** (1991) 39.
124. R. M. McMEEKING, *Int. J. Solids Struct.* (1993) in press.
125. M. McLEAN, *Compos. Sci. Technol.* **23** (1985) 37.
126. S. T. MILEIKO, *J. Mater. Sci.* **5** (1970) 254.
127. A. KELLY and K. N. STREET, *Proc. R. Soc. Lond.* **A328** (1972) 283.
128. T. G. NIEH, *Metall. Trans.* **15A** (1984) 139.
129. S. GUNAWADENA, S. JANSSON and F. E. LECKIE, *Acta Metall. Mater.* (1993) in press.
130. S. JANNSON and F. A. LECKIE, *J. Mech. Phy. Solids* **40** (1992) 593.
131. J. W. HOLMES, *J Mater. Sci.* **26** (1991) 1808.
132. C. WEBER, J. Y. YANG, J. P. A. LÖFVANDER, C. G. LEVI and A. G. EVANS, *Mat. Sci. Eng.* **A161** (1993) 285.
133. F. ABBE, J. VICENS and J. L. CHERMANT, *J. Mater. Sci. Lett.* **8** (1989) 1026.
134. C. WEBER, S. J. CONNELL and F. W. ZOK, ICCM-9 (Woodhead Pub. Madrid, 1993) to be published 417–23.

Received 15 October 1993
and accepted 12 January 1994.